UNIVERSITY OF EXETER

DOCTORAL THESIS

Reconfigurable phase-change optical metasurfaces: novel design concepts to practicable devices

---

Author:
Carlota RUIZ DE GALARRETA

Supervisors:
Prof. C. David WRIGHT
Dr. Jacopo BERTOLOTTI

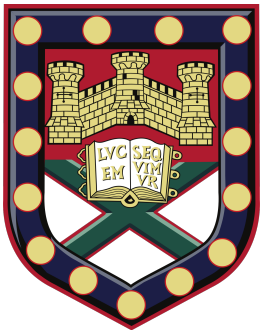

A thesis submitted in fulfillment of the requirements
for the degree of Doctor of Philosophy

Signed:

September 19, 2019

Declaration of Authorship

Reconfigurable phase-change optical metasurfaces: novel design concepts to practicable devices

Submitted by **Carlota RUIZ DE GALARRETA** to the University of Exeter as a thesis for the degree of Doctor of Philosophy in Physics in September 2019.

I certify that all material in this thesis which is not my own work has been identified and that no material has previously been submitted and approved for the award of a degree by this or any other University.

"Be of good cheer. Do not think of today's failures, but of the success that may come tomorrow. You have set yourself a difficult task, but you will succeed if you persevere; and you will find a joy in overcoming obstacles."

Helen Keller

2

UNIVERSITY OF EXETER

Abstract

Reconfigurable phase-change optical metasurfaces: novel design concepts to practicable devices

by Carlota RUIZ DE GALARRETA

Optical metasurfaces have been proven to be capable of controlling amplitude, phase and polarization of optical beams without the need of bulky geometries, making them really attractive for the development of compact photonic devices. Recently, their combination with chalcogenide phase-change materials (traditionally employed in non-volatile optical and electrical memories), whose refractive index can be reversibly and repeatedly controlled, has been proposed to yield low power consumption tunable metasurfaces having several functionalities in a single device. However, despite phase-change memories are commercially available since various decades now, the unification of phase-change materials with metasurfaces towards real life applications is becoming a formidable task, mainly due to the several engineering branches involved in this technology, which sometimes compromise each other in a non-trivial way. This includes thermo/optical, thermo/electric, and chemical incompatibilities which are typically not taken into account by researchers working in the field, resulting in devices having exciting reconfigurable properties, but at the same time, lack of practicability. This thesis is therefore dedicated to the development of novel phase-change metasurface architectures which could partially or totally address such engineering problems. Particular emphasis has been put in the realization of reconfigurable metasurfaces for active wavefront control, as such a functionality remains relatively unexplored.

The first part of this thesis focuses in the first experimental demonstration of active, reconfigurable non-mechanical beam steering devices working the near-infrared.

This was achieved via integration of ultra-thin films of chalcogenide phase-change materials (in this case, the widely employed alloy $Ge_2Sb_2Te_5$) within the body of a dielectric spacer in a plasmonic metal/insulator/metal metasurface architecture. Active, and optically reversible beam steering between two different angles with efficiencies up to 40% were demonstrated.

The second part of this work shows the work carried out in metal-free metasurfaces as a way to manipulate optical beams with high efficiency in both transmission and/or reflection. This was achieved via combination of all-dielectric silicon nanocylinders with deeply-subwavelenght sized $Ge_2Sb_2Te_5$ inclusions. By strategic placement of the phase-change inclusions in the regions of high electric field density, independent and active control of the metasuface resonances is demonstrated, with modulations depths as high as 70% and 65% in reflection and transmission respectively. Multilevel, and fully reversible optically-induced switching of the phase-change layer is also reported, with up to 11 levels of tunability over 8 switching cycles.

Finally, the last section of this thesis introduces the concept of hybrid dielectric-plasmonic phase-change metasurfaces having key functional benefits when compared to both purely dielectric and plasmonic approaches. The proposed architectures showed great versatility in terms of both active amplitude and phase control, offering the possibility of designing devices for different purposes (i.e. such as active absorbers/modulators or beam steerers with enhanced efficiency) employing the same unit-cell configuration with minor geometry re-optimizations. Initial device experimental demonstrations of such an approach are discussed, as well as their potential in terms of delivering in-situ electrical switching capabilities using a metallic ground plane as a resistive heater.

Acknowledgements

First, I would like to express my deepest gratitude to my supervisors, Prof. C. David Wright and Dr. Jacopo Bertolotti, for giving me the opportunity to do this PhD, as well as for their excellent guidance through the course of this project. More specifically, to David for always believing in me, as well as for his excellent advice; and to Jacopo, for teaching me how to look at problems from a different perspective. It has been a privilege working with both of you.

I'd like to thank as well my old professors from the University Complutense de Madrid, especially to Dr. J. M. Lopez Alonso, Dr. J. A. Gomez Pedrero and J. C. Martinez Anton, for transmitting me their clear passion for optics during my undergraduate studies, which in part made me be where I am now.

I could not be happier about my colleagues from our research group: the ones that have just arrived (Joe and Lu) for being so nice and having such an excellent predisposition to work, and obviously the older members; Yat-Yin, Em, Liam and Santi, for all the nice moments we have spent together during the last four years (and for the ones that will eventually come!). Special thanks also to the members who left, Dr. Kathik Nagareddy, Dr. Arseny Alexeev and Dr. Tobias Bachmann, as well as to our external collaborators Dr. Martin Lopez-Garcia (University of Bristol) and Dr. Ivan Sinev (ITMO University) for their valuable help and support during the development of this work.

Last but not least, I would like to thank my loved ones in Spain. My friends Anelis, Steffi, Ongui, Cati and Nabil for being the **best** friends that one could ever have (I love you so much). My parents, Dr. Fanjul Rodriguez and Dr. Ruiz de Galarreta Hernandez: I cannot express how grateful I am for the sacrifice they have made for me, as well as for their unconditional love. My older sister, Claudia, for always being my model to follow, and my brother-in-law Mehdi for treating her so well. And finally, my niece Alba – you have a long way to go and I wish you all the best in your life. This is for you *petite bichito*!

List of Publications and Conferences

I. Journal publications

1. Ruiz de Galarreta C, Alexeev A, Sinev I, Trofimov P, Ladutenko K, Garcia-Cuevas Carrillo S, Gemo E, Baldycheva A, Nagareddy K, Bertolotti J and Wright C D. Selective reconfigurable multilevel control of resonant modes in hybrid all-dielectric/phase-change metasurfaces. Optica, DOI 10.1364/OPTICA.384138, 2019

2. Ruiz de Galarreta C, Alexeev A, Sinev I, Trofimov P, Ladutenko K, Garcia-Cuevas Carrillo S, Gemo E, Baldycheva A, Nagareddy K, Bertolotti J and Wright C D. Next-generation tunable photonic devices enabled by hybrid phase change dielectric metasurfaces. Nature Communications, 2019 (Under review).

3. Gemo E, Garcia-Cuevas Carrillo S, Ruiz de Galarreta C, Baldycheva A, Hayat H, Youngblood N, Bhaskaran H, Wolfram H P P and Wright C D. Plasmonically-enhanced all-optical integrated phase-change memory. Optics Express, 27(17), 24724-24737, 2019.

4. Ruiz de Galarreta C, Alexeev A, Bertolotti J, Wright C D. Phase-Change Metasurfaces for Dyamic Beam Steering and Beam Shaping in the Infrared. IEEE International Symposium of Circuits and Systems, 2018.

5. Ruiz de Galarreta C, Alexeev A. M, Bertolotti J, Lopez-Garcia M, Klemm M, Cryan M. J, Au Y-Y, Wright C D. Nonvolatile Reconfigurable Phase-Change Metadevices for Beam Steering in the Near Infrared. Advanced Functional Materials, 28, 10, 1704993, 2018.

II. Attended conferences

1. Cai L, Ruiz de Galarreta C, Hearpath R, Hendry E, Qiu M, Qiang L, Wright D. Terahertz Amplitude Modulators Using Phase-Change Metamaterials. International Conference on Materials for Advanced Technologies (ICMAT), Marina Bay Sands, Singapore, 23-28 June, 2019. (Oral)

2. Sinev I, Ruiz de Galarreta C, Trofimov P, Alexeev A, Betolotti J and Wright C D. Dynamically Tunable All-dielectric Hybrid Silicon/Phase Change Optical Metasurfaces. International Conference on Materials for Advanced Technologies (ICMAT), Marina Bay Sands, Singapore, 23-28 June, 2019. (Oral)

3. Ruiz de Galarreta C, Alexeev A M, Au Y-Y, Shields J, Garcia-Cuevas Carrillo S, Bertolotti J, and Wright C D. Non-Volatile, Reconfigurable, Multilevel Photonic Devices Based on Phase-Change Metasurfaces and Thin Films. MRS spring meeting, Phoenix, Arizona, USA, 22th-26th April, 2019. (Oral)

4. Wright C D, Carrillo SGC, Galarreta C R, Gemo E, Trimby L, Alexeev AM, Au YY, Nagareddy VK, Baldycheva A, Bertolotti J. Phase-change metadevices for the dynamic and reconfigurable control of light. Novel Optical Materials and Applications (NOMA), Zurich, Switzerland, 2–5 July 2018. (Oral)

5. Ruiz de Galarreta C, Alexeev A, Bertolotti J, Wright CD. Phase Change metaoptics with enhanced efficiency. European Phase Change and Ovonic Symposium, EPCOS 2018, Sicily, Italy, 23-25 Sep 2018. (Poster)

6. Ruiz de Galarreta C, Alexeev A, Bertolotti J, Lopez-Garcia M, Klemm M, Cryan MJ, Au Y-Y, Wright C D. Phase-change metasurfaces for dynamic beam stteering in the near infrared. Photonic and Optoelectronic Materials, Royal Microscopy Society (RMS), Exeter, UK, 9th April 2018. (Oral)

7. Ruiz de Galarreta C, Alexeev A M, Au Y-Y, Bertolotti J, Cryan M J, Klemm M, Wright C D. (2017) Phase-Change Plasmonic Metasurfaces for Dynamic and Reconfigurable Beam Steering and Beam Shaping in the Near Infrared. Materials Research Society, MRS fall meeting 2017, Boston, Massachussets, USA, Nov 2018. (Oral)

8. Ruiz de Galarreta C, Alexeev A M, Bertolotti J, Cryan M J, Klemm M, Wright C D. (2017) The design of practicable beam steering and beam shaping phase-change metasurfaces working at telecom frequencies, European Phase Change and Ovonic Symposium, EPCOS 2017, Aachen, Germany, 3rd - 5th Sep 2017. (Poster)

9. Au Y-Y, García-Cuevas Carrillo S, Ruiz de Galarreta C and C D. Wright (2017). Infrared Phase-Change Meta-Devices with In-Situ Switching. European Phase Change and Ovonic Symposium, EPCOS 2017, Aachen, Germany, 3rd - 5th Sep 2017. (Poster)

10. Alexeev A M, Ruiz de Galarreta C, Garcia-Cuevas Carrillo S, Sinev I S, Samusev A K, Gemo E, Nagareddy V K, Au Y-Y, Wright C D. Tunable Dielectric Metadevices Enabled by Phase-Change Materials, European Phase Change and Ovonic Symposium, EPCOS 2017, Aachen, Germany, 3rd - 5th Sep 2017. (Poster)

11. Wright C D, Garcia-Cuevas S, Ruiz de Galarreta C, Trimby L, Cryan M. Phase-change meta-photonics. European Phase Change and Ovonic Symposium, EPCOS 2016, Camrbdige, UK, Sept 2016. (Oral)

Contents

List of Abbreviations

AFM	**A**tomic **F**orce **M**icroscopy
BFP	**B**ack **F**ocal **P**lane
BP	**B**erry **P**ancharatnam
DC	**D**irect **C**urrent
DRA	**D**ielectric **R**esonant **A**ntennas
EBL	**E**lectron **B**eam **L**ithography
ED	**E**lectrcic **D**ipole
EDS	**E**nergy **D**ispersive **S**pectroscopy
EM	**E**lectro**m**agnetic
GSP	**G**ap **S**urface **P**lasmon
GSPR	**G**ap **S**urface **P**lasmon **R**esonance
GST	$Ge_2Sb_2Te_5$
GSST	$Ge_2Sb_2S_4Te_1$
ITO	**I**ndium **T**in **O**xide
LC	**L**iquid **C**rystal
LIDAR	**L**ight **I**maging **D**etection **A**nd **R**anging
MD	**M**agnetic **D**ipole
MIM	**M**etal **I**nsulator **M**etal
MW	**M**icro**w**ave
MWIR	**M**id **W**ave **I**nfra**r**ed
NIR	**N**ear **I**nfra**r**ed
PCM	**P**hase **C**hange **M**aterial
PDMS	**P**oly**D**i**M**ethyl**S**iloxane
PIN	**P**-type **I**intrinsic **N**-type
RF	**R**adio **F**requency
RFP	**R**ear **F**ocal **P**lane
SEM	**S**canning **E**lectron
TE	**T**ranseverse **E**lectric
TM	**T**ranseverse **M**agnetic
XRD	**X**-**R**ay **D**iffraction

A mi sobrina Alba

Chapter 1

Introduction and Motivation

1.1 Optical beam control: From passive bulky optics to active metasurfaces

Since the beginning of mankind, the human race has always shown strong interest in the origin of optical phenomena, and how to control them for its own benefit. Evidences of early objects for light control currently date from the beginning of bronze age [1], with the discovery of ancient mirrors and lenses based on polished metals and rock crystal (quartz) respectively (**Figure 1.1**). Despite there being uncertainty about whether the physics behind such items were known by then, it is believed that their function was to serve as imaging and magnification tools [2]. Today, conventional bulky optics are still being used for focusing, imaging and guiding light, and serve as the key elements in most of our current optical devices. Their working principle is now well known: their ability to mould and control light in a particular way relies on propagation effects such as phase accumulation and interference effects of electromagnetic (EM) waves in refractive and reflective materials. This has paved the way for the development of more sophisticated optical components such as interference filters/coatings or lenses with freeform and aspheric geometries, whose functionalities can be deliberately controlled by design via proper material and geometry combination [3].

In 1801, Thomas Young demonstrated that a beam diffracted by two slits can generate a fringe pattern as result of constructive and destructive interferences based on Huygens' principle. The double slit experiment provided for the first time an experimental evidence for the acceptance of wave theory of light [3], and triggered

the development of non-bulky devices for light control based on both interference **and** diffraction effects. This includes diffraction gratings made of periodic structures with periods d in the order of the wavelength, which are typically used to split a beam into different directions (diffraction orders). Because the direction of such beams depend on the period and the wavelength of the incident beam, diffraction gratings are commonly used as dispersive elements, i.e. to split white light into different monochromatic components [3, 4].

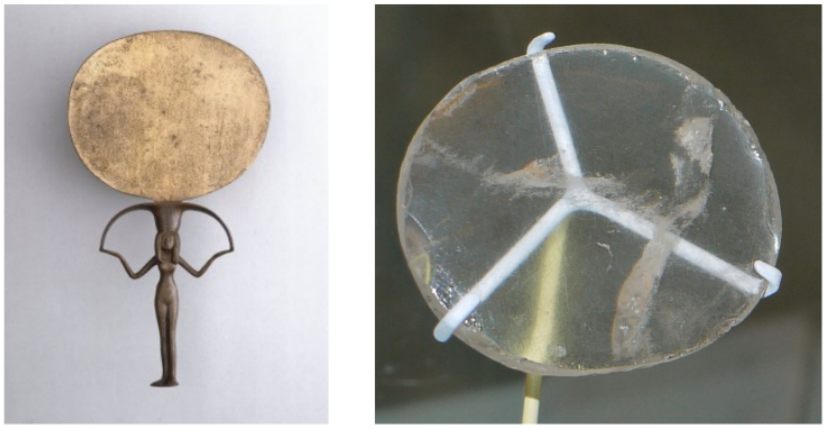

FIGURE 1.1: Examples of ancient objects for light control. Mirror made of silver and copper alloys, dating from $\sim$ 1478-1390 B.C. (ancient Egypt, left). The Nimrud lens, made of rock crystal and dating from $\sim$ 750–710 B.C. (ancient Assyria, right). Images taken from the Brooklyn and British museum websites (https://www.brooklynmuseum.org/ and https://www.britishmuseum.org respectively).

Despite bulky optics and diffractive elements still being heavily employed nowadays, their effect on optical beams are locked at the design stage, thus limiting their functionalities to a single configuration. For example, a lens will have a fixed numerical aperture based on its geometry and constituent materials, which will determine its spatial resolution and thus the minimum distance at which two points can be resolved. The potential of conventional optical components can be eventually increased by combining various elements to form more sophisticated optical systems such as spectrometers, where both lenses and mirrors are combined with diffraction gratings to analyse the spectral content of light after interacting with a specimen. Even so, such systems suffer from other unavoidable design and fundamental limitations, such as size and weight, or spatial/spectral resolution.

A new and more flexible approach to light manipulation emerged around two

decades ago with the introduction of metamaterials and metasurfaces. Such devices are engineered structures made of sub-wavelength (typically resonant) building blocks which can be either periodically or randomly arranged. By properly engineering the spacing, dimensions and electromagnetic properties of such building blocks (sometimes named meta-atoms), metamaterials and metasurfaces can achieve effective EM properties (i.e. permittivities and permeabilities) beyond those found in nature [5], and/or mimic the functionalities of conventional optics without the need of bulky geometries respectively [6]. Since the concept of metasurfaces emerged, considerable research efforts have been put into the development of novel "meta-device" prototypes with unusual properties, and spanning the ultraviolet to the microwave spectrum. Examples of this research trend in the optical regime include devices for amplitude control (such as super absorbers [7, 8]), and phase control, e.g., holograms [9], flat lenses [10] or beam steerers [11]. However, despite optical metasurfaces having emerged as a versatile design platform which can offer clear advantages over classical optical components (such as lightweight photonic devices or exotic EM phenomena), they share the same issue in terms of static-functionalities. That is, their utility is fixed by design so that a particular metasurface design will have a repeatable and stationary effect on optical beams. Hence, many potential applications of metasurfaces have been frustrated, among others, by the lack of tuning capabilities. Motivated by this, over the last years several approaches to reconfigurable/dynamically tunable metasurfaces have been proposed by the scientific community [12, 13]. As summarised in **Figure1.2**, five principal methods to provide dynamic light control using metasurfaces can be identified, from which four of them are based on tuning the optical properties of the constituent or surrounding materials [12]:

a. Optically tunable metasurfaces

Optical tuning consists of locally varying the permittivity of the metasurface constituent materials via generation of non-linear optical effects, which are driven by ultrafast, high-power laser irradiation [12, 14]. Depending on the laser intensity, pulse duration, as well as on the physical characteristics of the irradiated material,

different nonlinear mechanisms can be generated to achieve optically tunable metasurfaces [14, 15, 16, 17]. For example:

- Changes in the permittivity driven by laser pumping can be induced via optical Kerr and two photon effects in all-dielectric metasurfaces made of materials such as germanium (Ge) [18] or silicon (Si) [19], whose Kerr and two photon absorption coefficients are high [14]. These phenomena are proportional to the irradiance of the external laser pump, thus multilevel tuning becomes possible via control of the applied power [14, 20].

- In the case of metals where light attenuation is dominated by linear absorption, changes in the permittivity due to non-linear effects become accessible through the use of metamaterials whose building blocks are of the order of the metal penetration depth [21, 22]. However, the most common approach is to use metallic nanoparticles to enhance the Kerr and two-photon effects of surrounding dielectrics via excitation of localised plasmon resonances [17].

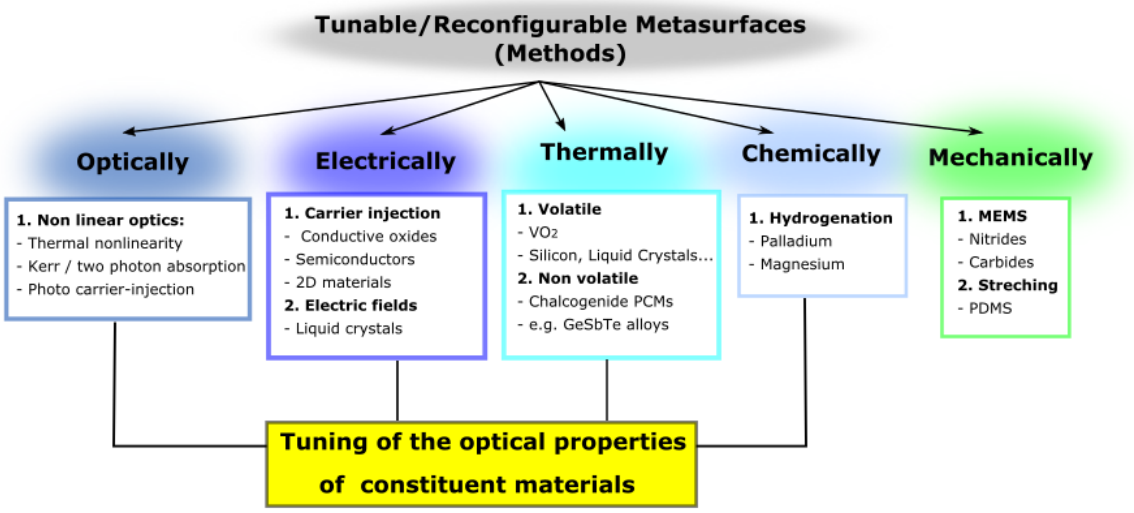

FIGURE 1.2: Schematics of different methods employed to yield tunable/reconfigurable metasurfaces

b. Electrically tunable metasurfaces

This approach can be considered as the electrical counterpart to optical tuning, as it is based on changing the optical properties of the metasurface constituent materials via electrical stimuli. Reconfigurable metasurfaces of this form typically consist of

meta-atoms made of electrically sensitive materials with incorporated varactors or PIN diodes [12], and can be classified in two main groups:

- One is based on electrically driven carrier density modifications in materials such as indium tin oxide (ITO), semiconductors (Si, GaAs...) or 2D materials (graphene, MoS_2...) [23, 24, 25]. In analogy to optical photo carrier-injection, a change in the free carrier density produces changes in the plasma frequency of the material (hence in its permittivity), which results in alteration of the metasurface electromagnetic response.

- The second approach is based on the use of liquid crystals (LC), whose molecular orientation and thus birrefringence can be modified on demand via applying a voltage between two electrodes. The permittivity of such materials can be therefore gradually controlled with variations of the voltage [26, 27].

c. Thermally tunable metasurfaces

The combination of metasurfaces with materials whose dielectric properties are thermally sensitive is another option towards achieving reconfigurability [12]. Thermally driven metasurface tuning can be divided in two main categories depending on the underlying mechanism:

- One is based on volatile thermal switching, which takes advantage of materials with sizeable temperature-dependant dielectric permittivities. Materials such as VO_2 are currently the most exploited options [28, 29, 30, 31]. This compound undergo an insulator to metal phase transition at relatively low temperatures (66 °C) [32] which is accompanied by abrupt changes in its optoelectronic properties. Hence, VO_2 has been substantianly employed to create reconfigurable metasurfaces from the visible to the THz spectral regimes [28, 29, 30, 31, 32]. Alternative materials have been also successfully combined with metasurfaces to yield thermally-tunable photonic devices, including thermotropic liquid crystals, semiconductors, or superconductors [12].

- The above approach requires for a constant heat simulus to hold changes of the dielectric function of the active material over time, which depending on

the application might result in high power consumption. Non-volatile thermal switching does not suffer from this issue, and is essentially occupied by chalcogenide phase change materials (PCMs) typically made of germanium (Ge), antimony (Sb) and tellurium (Te) alloys [33, 34]. As in the case of Vanadium Oxides, a structural phase transition (in PCMs from amorphous to crystalline states) with subsequent sharp changes in the optical properties can be thermally driven in such PCM compounds [33]. The main difference here relies on the fact that despite the crystalline phase of chalcogenide PCMs is more energetically favourable [33, 35], chalcogenide PCMs can remain amorphous at room temperature for decades [33], making them eminently suitable for low power consumption memories or reconfigurable photonic devices. Indeed, various dynamically reconfigurable metasurfaces have been demonstrated over the last couple of years [34]. In addition to chalcogenide PCMs, non-volatile reconfigurable metasurfaces based on amorphous to crystalline switching of silicon nano-particles have been also recently demonstrated [36]

Both volatile and non-volatile thermal switching can be successfully carried out in reconfigurable metasurfaces employing different types of heating mechanisms, such as resistive Joule heating via electrical contacts [37], optical heating employing laser scans [38], or simply via hot plate annealing [39].

d. Chemically tunable Metasurfaces

Another method to achieve tunability of metasurfaces is based on the use of chemically sensitive materials as building blocks, where the optical properties can be altered via chemical reactions. For example, in ref. [40], Tittl et al. experimentally demonstrated the concept of tunable absorbing metasurfaces via hydrogen adsorption by palladium, where the amplitude (reflectance) of visible light can be switched as a function of hydrogen concentration. Other approaches such active structural colour generation via hydrogenation and de-hydrogenation of magnesium based metasurfaces have been reported [41].

f. Mechanically tunable Metasurfaces

The tunability methods described previously are essentially based on modifying the optical properties of constituent materials. Mechanical tuning proposes an

alternative pathway which consists of actively changing the geometrical design parameters (such as thicknesses and/or spacing between elements), which results in changes of the metasurface electromagnetic response. Two main approaches have been reported so far:

- One is based on the so-called micro-electro-mechanical-systems (MEMS), consisting of electrically activated switches made of piezoelectric and/or pyroelectric materials, such as nitrides (e.g. Si_3N_4, GaN), carbides (e.g. SiC) and other ceramics [42, 43].
- The second approach takes advantage of substrates made of elastic materials such as polydimethylsiloxane (PDMS). Mechanical tuning is here achieved via stretching the substrate to change the inter-distance between resonant nanoparticles [44, 45].

The integration of methods such as those described in **a)** to **f)** into real-life optical devices is far from easy, as local tuning of optical metasurfaces and/or individual meta-atoms becomes a formidable task at the nanoscale. Nevertheless, the ability to dynamically control the detailed spatio-temporal nature of optical beams using lightweight reconfigurable metasurfaces would open up a new route to a wide range of exciting applications going from imaging to telecommunications. This includes e.g., active flat optical components such as reconfigurable holograms, lenses, optical switches, active colour displays or non-mechanical beam steering [6, 34]. The present work is therefore dedicated to the study and experimental realisation of novel reconfigurable metasurface device architectures, particularly focused on the practicable combination of phase-change materials with metasurfaces towards the realisation of real-life devices. In the following subsections, the motivation and challenges of such a pursuit will be briefly discussed, and the specific objectives of the work carried out will be explained.

1.2 Motivation and objectives

Research interest in the area of dynamically reconfigurable metasurfaces is growing fast. As described in the previous section, the majority of the approaches to

active metasurfaces reported up to now rely on tuning of the refractive index of the constituent elements. Perhaps one of the best candidates to make this happen are chalcogenide phase-change materials, due to their excellent tunability properties. That is, high refractive index contrast between amorphous and crystalline states, non-volatility, fast switching times and large number of switching cycles [33], which would potentially result in photonic devices with high optical contrast, low power consumption, high operational speed, and large endurance respectively. Particularly over the few last years, the combination of chalcogenide phase-change materials (traditionally employed in memory technologies) with metasurfaces has been arguably one of the most explored option, as reflected by the number of publications per year (in **Figure 1.3**).

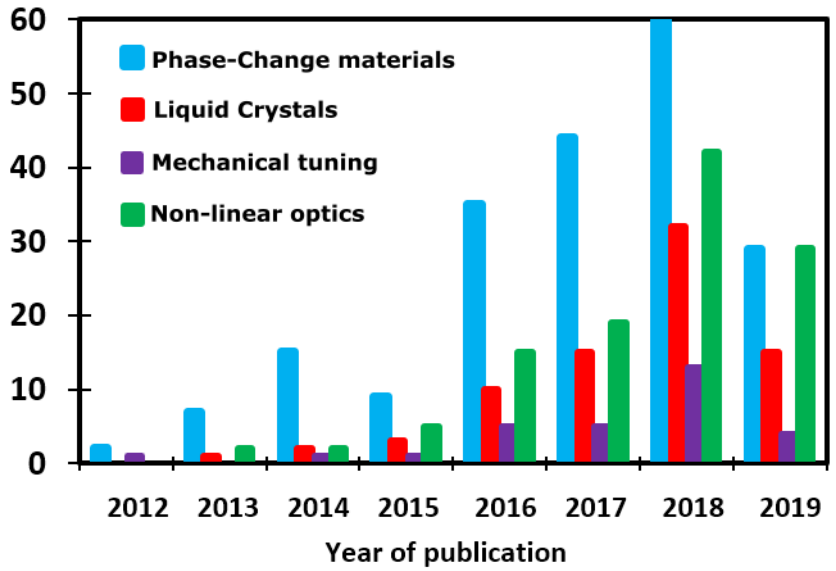

FIGURE 1.3: Number of published papers per year about reconfigurable/tunable optical metasurfaces, sorted by various methods. Tuning based on phase-change materials and non-linear optics are so far the most employed methods. Data extracted from Web of Science in June 2019.

In spite of the amount of research effort put in the development of phase-change metasurfaces, such research is still at a relatively low stage of maturity, and a long way away from becoming a commercial technology. To date most of the published work relies on numerical simulations showing new potential applications of active phase-change meta-devices [46, 47, 48, 49, 50, 51, 52, 53, 54, 55, 56, 57, 58, 59, 60, 61, 62]; with only a sub-set of concepts having successfully fabricated and tested,

from which a huge majority is based on active amplitude control and modulation of light across different parts of the IR specturm [7, 63, 64, 65, 66, 67, 68, 69, 39, 70, 71]. Furthermore, only a few experimental demonstrations of reversible optical switching (i.e. crystallisation and re-amorphisation) over multiple cycles can be currently found in the literature [7, 38, 70, 72], and no phase-change active metasurfaces with reversible electrical switching capabilities have been reported so far, to the best of our knowledge. Instead, the most common practice relies on optical characterisation of the amorphous, as-fabricated, PCM metasurface with subsequent characterisation in the crystalline state after hot plate crystallisation (annealing) as a proof of concept [34, 63, 66, 69, 71]. The lack of agile progress in this field is mainly due to three main key issues:

1. The first issue consists of the presence of **various non-trivial, engineering crossroads arising from the marriage of chalcogenide phase-change materials and metasurfaces**. In this context, perhaps one of the most challenging point comes from the balance of optical and thermal responses when designing phase-change metasurfaces. Because PCMs require for a melt-quench process to re-amorphised [33], re-amorphisation might become challenging (or even impossible) over large volumes due to thermal insulation [73]. In turn, employing small PCM volumes in metasurfaces can result in low optical contrast, which limits the device tunability and thus compromises the optical performance. On the other hand, **chemical reactions and incompatibilities of chalcogenide phase-change materials** are often not taken into account by researchers working in the field. This includes oxidation of PCMs when exposed to air (e.g. see [46, 68, 39]), or thermally induced metal diffusion into chalcogenide PCMs [74]. That said, it becomes clear that the design of phase-change meta-devices having optimum optical responses and ex-situ (i.e. laser-induced) switching capabilities simultaneously turns into a challenging task. Electrically-driven, pixel-by-pixel, in-situ switching is indeed even more challenging; as it would involve the use of resistive heaters and electrical contacts made of metals not suffering from thermally-induced diffusion into PCMs. At

the same time, such metallic parts must be made of materials suitable for plasmonics in the optical regime to avoid degradation of the optical response (such as gold, silver or aluminium)[75], and must have melting points higher than PCMs to prevent long-time deformation of the heating elements.

2. In terms of optical performance, the majority of phase-change active metasurfaces reported up to now suffer from **low efficiency**: first because they are mainly based on metallic building blocks introducing plasmonic losses [46, 70, 64, 66, 76]; and second, because commonly employed PCM compositions do suffer from unavoidable dielectric losses in the infrared, which are in general very low in the amorphous phase, but become higher after crystallisation [34, 77]. Both sources of losses combined together typically result in phase-change metasurfaces having operation efficiencies and/or modulation depths below or in the order of 20% [64, 66, 70]. Exploring new metasurface architectures outside from the purely plasmonic approach is therefore needed in order to increase these numbers.

3. Following the previous point, there is also a clear l**ack of suitable chalcogenide phase-change compositions specifically synthesised for their integration in metasurfaces**. Since phase-change materials have been traditionally employed in non-volatile electronic and optical memories, research efforts have been so far put on the synthesis of new alloys whose physical properties are suitable for this purpose. Nevertheless, the material requirements for the progress of non-volatile memories do not necessarily match what is expected from tunable metasurfaces. For example currently employed PCM compositions have the capability to switch between phases in timescales of units of nanoseconds or even less [33, 78], which is quite useful for their integration in memory and/or computing devices but would find no utility in some other applications related to phase change metasurfaces. For instance, eye-related technologies like active colour displays or smart glasses would not find real benefits from such high operational speeds, as the eye-brain temporal resolution is far below the switching speeds of current PCM alloys. On the other hand, despite the need of high electro-optical contrast between the

structural phases of PCMs is common to both metasurfaces and memory technologies, chalcogenide phase change alloys do suffer from strong optical losses in the visible spectrum [77], which is not relevant to memory devices but might limit the potential of developing active metasurfaces operating in such spectral regime. The majority of available alloys have their corresponding (amorphous and crystalline) bandgaps located in the infrared spectrum [77], which is highly desirable for low power consumption electronic memories, but in turn; results in severe degradation of the optical performance when designing metasurfaces in the visible spectrum.

Solutions to **3** would involve the development of new PCM compositions with properties specifically focused on the progress of reconfigurable metasurfaces, which falls outside of the topic of this thesis. Nevertheless, this work is motivated by the need of overcoming the key engineering conflicts briefly described in **1** and **2** , which can be potentially sorted out at the design stage. Therefore, the main objective of this thesis is to design, analyse and experimentally validate novel and practicable metasurface architectures which could partially or totally address such engineering crossroads. The design philosophy followed in this work has been inspired when possible by current well-established commercial PCM optical and electrical non-volatile memories (reviewed in-depth in **Chapter 2**) towards future integration of reconfigurable phase-change metasurfaces in real-life applications. Following this philosophy, the design, fabrication, characterisation and analysis of future potential of various device prototypes employing different metasurface configurations have been carried out. Finally, since almost all of the work developed up to now is based on amplitude modulation, particular emphasis has been put in the development of reconfigurable devices for optical phase control in the near infrared, with potential applications in beam steering, active lensing or holography.

1.3 Thesis outline

The first chapter of this thesis has served as a brief introduction to the state of the art of currently available devices for optical beam control, from conventional optics to the various types of reconfigurable/tunable metasurfaces. The main (but not the

only) engineering challenges for a successful development of phase-change material based dynamic metasurface technology have been then identified, followed by a statement of the main objectives of the present work.

The rest of the manuscript will continue according to the following scheme:

Chapter 2 starts with a review of basic electromagnetism, towards a better understanding of the frequency-dependent fundamental limitations of naturally occurring materials in terms of light/matter interaction. The concepts of metamaterials and metasurfaces are then introduced in more detail, and some of the most relevant examples on how metamaterials can yield the fundamental limits of natural substances will be explained to the reader. The evolution of such technology will be then briefly reviewed from the first metamaterial prototypes to their recently emerged two-dimensional analogues (i.e. metasurfaces).
The main physical properties and characteristics of chalcogenide phase-change materials, as well as their traditional applications in non-volatile optical and electrical memories will be then reviewed. Some of the most relevant modern applications of phase-change materials outside the memory technology will be then briefly revisited, with particular emphasis on the current state of the art work of recently-developed reconfigurable metasurfaces employing PCM alloys and their technological challenges.

Chapter 3 provides in-depth details of the tools and methodologies employed for the realisation of this work. As this thesis involves the design, analysis, fabrication and characterisation of nano-photonic devices, a wide range of computational, nanofabrication and characterisation methods have been therefore required for its correct development. This chapter aims to provide both background and procedures of the various methods employed.

Chapters 4 to 6 describe the bulk of the computational and experimental work carried out during the project. The combination of ultra thin PCM layers with different meta-atom structures (i.e. plasmonic metal/insulator/metal, high index all-dielectric, and hybrid dielectric-metal configurations) is proposed and experimentally validated in **Chapters 4** , **5** and **6** respectively. More specifically:

- **Chapter 4** Shows the development of non-volatile, reversible, active beam steering in the near-infrared employing phase-change metal/insulator/metal metasurfaces (reported in [38]).

- **Chapter 5** sets out the work carried out in developing all-dielectric, hybrid silicon/PCM metasurfaces. The observation of new exciting features arising from this combination (such as individual control of Mie-like electric resonances) has been exploited for the design and experimental realisation of exotic reconfigurable optical switches, as well as for the first experimental realisation of laser-induced multilevel and reversible switching in phase-change metasurfaces (reported in [79]).

- **Chapter 6** introduces the concept of hybrid dielectric-plasmonic metasurfaces having key functional benefits when compared to both purely dielectric and plasmonic metasurfaces (see [80]). Initial device experimental demonstrations of such an approach in the near infrared (NIR) are discussed, as well as their potential in terms of delivering in-situ electrical switching capabilities with superior scattering efficiency.

Each of the results chapters starts with a brief introduction and motivation of the work specifically carried out, and ends up with an discussion of the pros and cons of the particular phase-change meta-atom configuration investigated, as well as a list of possible future work.

Finally **Chapter 7** contextualises and reiterates the results of this work, with an overview of the key findings discussed on each chapter.

In terms of original contribution to knowledge, the work carried out in this thesis makes a key improvement towards the development of practicable active phase-change metasurfaces for real-world applications, as it demonstrates both numerically and experimentally that the relevant engineering conflicts arising from the marriage of phase-change materials with metasurfaces can be sorted out at the design stage. This was achieved via establishing a design philosophy specifically focused in minimising the amount of PCMs down to what is typically used in non-volatile

memories, while at the same time not interfering with other relevant engineering aspects, such as optical performance (i.e. efficiency and tunability), or chemical interactions (e.g. oxidation or metal diffusion into PCMs). Such an approach resulted in excellent optical device performances, as well as successful reversible switching of all the developed devices without signs of performance degradation.

Chapter 2

Background

2.1 Light-matter interaction: Fundamental limits of natural materials

For a better understanding of the technological importance of metamaterials and metasurfaces and their potential towards the development of novel photonic technologies, it is first convenient to understand the inherent limitations of natural materials in terms of light-matter interaction. Naturally occurring materials display a wide range of complex arrangements of atoms with both free or bound electrons, which are directly responsible for their macroscopic electromagnetic (EM) response. Light propagation in a medium is dictated by Maxwell's equations, which relate the spatio-temporal variation of the displacement electric fields $\vec{D}$ and magnetic induction $\vec{B}$, with the magnetic $\vec{H}$ and electric $\vec{E}$ fields of an EM wave respectively [5]:

$$\nabla \cdot \vec{D} = \rho \tag{2.1}$$

$$\nabla \cdot \vec{B} = 0 \tag{2.2}$$

$$\nabla \times \vec{E} = -\frac{\partial \vec{B}}{\partial t} \tag{2.3}$$

$$\nabla \times \vec{H} = -\frac{\partial \vec{D}}{\partial t} + \vec{j} \tag{2.4}$$

where ρ and $\vec{j}$ are the free electric charge and electric current respectively. Maxwell's

equations still apply to light matter interaction even at the atomic scale, where bound, free charges and currents are present. For simplicity, and since for the materials considered in this thesis, the magnetic response is weak at high (optical) frequencies [81], we will neglect the magnetic properties for the moment. Thus, the macroscopic material properties of most interest are electrical, and can be expressed by the following linear relations between fields:

$$\vec{D} = \varepsilon_0\vec{E} + \vec{P} = \varepsilon_0\vec{E} + \varepsilon_0\tilde{\chi_e}\vec{E} = \varepsilon_0(1 + \tilde{\tilde{\chi}_e})\vec{E} = \varepsilon_0\tilde{\varepsilon_r}\vec{E} \tag{2.5}$$

where $\vec{P}$ is the polarisation which quantifies the electric dipole moment per unit of volume, $\tilde{\tilde{\chi}_e}$ is the electric susceptibility and $\tilde{\varepsilon_r}$ is the complex relative permittivity of the material.

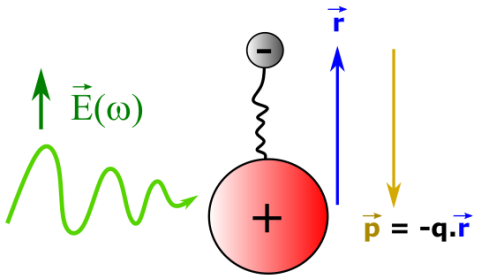

FIGURE 2.1: Nucleus/electron forced and damped harmonic oscillator model.

In the case of dielectric materials where electrons are bound to the atomic nucleus, a Lorentz model within the electromagnetic formalism can be applied to derive the frequency-dependant relative permittivity. That is, as depicted in **Figure 2.1**, considering individual atoms as forced and damped harmonic oscillators, where electrons exhibit periodic motion under the presence of harmonic electric fields from an EM wave. In one dimension, for an isotropic, homogeneous and linear material, the electron equation of motion is defined by

$$m_e\frac{d^2\vec{r}}{dt^2} + m_e\gamma\frac{d\vec{r}}{dt} + m_e\omega_0^2 = -q_e\vec{E} \tag{2.6}$$

where m_e and q_e are the electron mass and charge respectively, γ the damping factor, and ω_0 the natural oscillation frequency. Given that the electric field of an EM

wave is harmonic with an angular frequency ω, by Fourier transforming eq. 2.7 and solving for $\vec{r}$ we get:

$$\vec{r}(\omega) = -\frac{q_e}{m_e}\frac{\vec{E}}{\omega_0^2 - \omega^2 - i\gamma\omega} \tag{2.7}$$

As shown in **Figure 2.1**, the displacement of charges induces a local electric dipole moment $\vec{p}(\omega) = -q_e\vec{r}(\omega)$. However, since materials are made of billions of atoms, the response of a single atom to an harmonic electric field is not enough to determine their macroscopic response. Instead, an average dipole moment per unit of volume (i.e. the polarisation $\vec{P}$) needs to be used:

$$\vec{P}(\omega) = N\langle\vec{p}(\omega)\rangle \tag{2.8}$$

where N is the number of atoms per unit of volume. That said, eq. 2.8 can be re-written as a function of $\vec{P}$:

$$\vec{P}(\omega) = \frac{Nq_e^2}{m_e}\frac{\vec{E}}{\omega_0^2 - \omega^2 - i\gamma\omega} \tag{2.9}$$

Recalling the definition of polarisation from eq. 2.5 where $\vec{P} = \varepsilon_0\tilde{\chi_e}\vec{E}$; we can finally get a frequency dependant expression for the electric susceptibility $\tilde{\chi_e}$:

$$\tilde{\chi_e}(\omega) = \frac{Nq_e^2}{m_e\varepsilon_0}\frac{1}{\omega_0^2 - \omega^2 - i\gamma\omega} \tag{2.10}$$

and thus for the relative permittivity,

$$\tilde{\varepsilon_r}(\omega) = \varepsilon_r'(\omega) + i\varepsilon_r''(\omega) = 1 + \frac{\omega_p^2}{\omega_0^2 - \omega^2 - i\gamma\omega} \tag{2.11}$$

$$\varepsilon_r'(\omega) = 1 + \omega_p^2\frac{\omega_0^2 - \omega^2}{(\omega_0^2 - \omega^2)^2 + \gamma^2\omega^2} \tag{2.12}$$

$$\varepsilon_r''(\omega) = \omega_p^2\frac{\gamma\omega}{(\omega_0^2 - \omega^2)^2 + \gamma^2\omega^2} \tag{2.13}$$

where ω_p is the plasma frequency:

$$\omega_p = \sqrt{\frac{Nq_e^2}{m_e\varepsilon_0}} \tag{2.14}$$

Lorentz models can nicely predict the EM response of substances having electrons bound to the nucleus. However, materials like metals have free, unbonded clouds of electrons; meaning that there is no restoring force, thus no resonant frequency. By imposing $\omega_0 = 0$ in eq. 2.6, one can end up with the Drude model that describes the EM response of metals [5],

$$\tilde{\varepsilon_r}(\omega) = \varepsilon_r'(\omega) + i\varepsilon_r''(\omega) = \left(1 - \frac{\omega_p^2\tau^2}{1+\omega^2\tau^2}\right) + i\left(\frac{\omega_p^2\tau\omega^{-1}}{1+\omega^2\tau^2}\right) \tag{2.15}$$

Note that both the natural frequency and the damping coefficient of eq. 2.6 are not present in the permittivity function of metals, although there is still a damping term τ that accounts for the collisions within the electron cloud.

From eqs. 2.15 and 2.11, it is clear that the electromagnetic properties of naturally occurring materials hold frequency-dependant restrictions, as well as particular values of the plasma frequency ω_p and damping τ. A medium exhibiting such behavior is named dispersive, and the way in which a wave propagates and interacts with it is described by the dispersion relation:

$$k(\omega) = \frac{\omega}{c}\tilde{n}(\omega) = \kappa_0(\omega)\tilde{n}(\omega) = \kappa_0(\omega)\sqrt{\tilde{\mu_r}(\omega)\tilde{\varepsilon_r}(\omega)} \tag{2.16}$$

where k and k_0 are medium and free-space wavenumbers respectively, c is the vacuum speed of light, $\tilde{n}$ is the refractive index of the medium, and $\tilde{\mu_r}$ is the relative permeability. As stated earlier in this section, the magnetic response of natural materials at optical frequencies is weak, thus can be neglected via imposing $\tilde{\mu_r} = 1$. This occurs because contrary to the excitation of electric dipoles, which is formed via electron displacements driven by harmonic electric fields (represented in **Figure 2.2**), magnetic dipole induction relies on Larmor precessions having gyromagnetic ratios which are much slower compared to electric dipole oscillations [82]. Therefore, excitation of magnetic dipoles occur at lower frequencies located below the GHz regime, which limits even further the response of naturally occurring materials in optics.

Figure 2.2 shows an example of the frequency-dependant permittivity for amorphous silicon (left) and platinum (right), calculated with Lorentz and Drude models

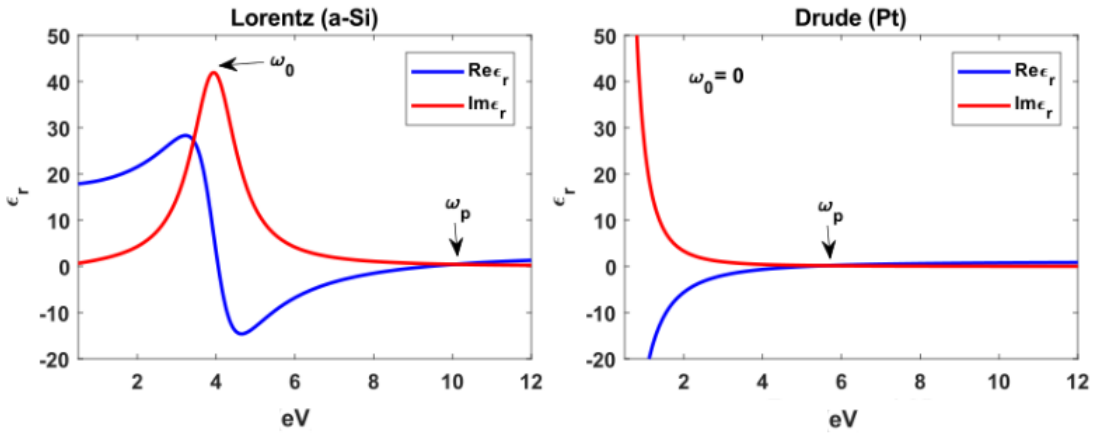

FIGURE 2.2: Permittivity function of amorphous silicon a-Si (left) and platinum Pt (right) obtained employing Lorentz and Drude models respectively. Model parameters for a-Si were obtained from public domain (www.horiba.com), and from Ref. [83] for Pt.

respectively. From **Figure 2.2** (left), it can be seen that the in the case of dielectrics or semiconductors at high frequencies, the real and imaginary parts of the permittivity reach a maximum around the natural frequency of the material ω_0. This peak corresponds to a strong absorption of the wave inside the material, due to energy coupling to the atomic structure. Out of the resonant frequency, three principal regimes can be identified:

- **when** $\omega < \omega_0$, The real part of $\tilde{\varepsilon_r}$ has a positive sign, thus wavenumber k defined in eq. 2.16 is a real number. Such a frequency regime corresponds therefore to a transparency window, where EM waves are allowed to propagate.
- **when** $\omega_0 < \omega < \omega_p$, Re$\{\tilde{\varepsilon}_r\}$ becomes negative, thus the wavenumber is imaginary. As a result, waves become evanescent and cannot propagate inside the material, thus light is reflected instead.
- **when** $\omega > \omega_p$, Re$\{\tilde{\varepsilon}_r\}$ becomes positive again, resulting in a second transmission window.

In the case of metals with no resonant frequency (**Figure 2.2** (right)), the above can be simplified to two main regimes:

- $\omega < \omega_p$ corresponds to a non-propagative regime due to negative values of Re$\{\tilde{\varepsilon}_r\}$, resulting in light being reflected by the medium.

- **when** $\omega \gg \omega_p$, metals exhibit a transmission region just like insulators, thus waves are allowed to propagate since Re{$\tilde{\varepsilon}_r$}>0.

Close to the plasma frequency, radiation can penetrate inside the metal, but at the same time experiences fast exponential decay due to strong losses [5]. Such attenuation along the propagation direction defines the skin depth (δ) of the metal [81]:

$$\delta = \frac{c}{\omega k} \tag{2.17}$$

which is the distance from the metal boundary to the point where the amplitude of the propagating waves are dissipated to 1/e (i.e. when 63% of the wave has been absorbed).

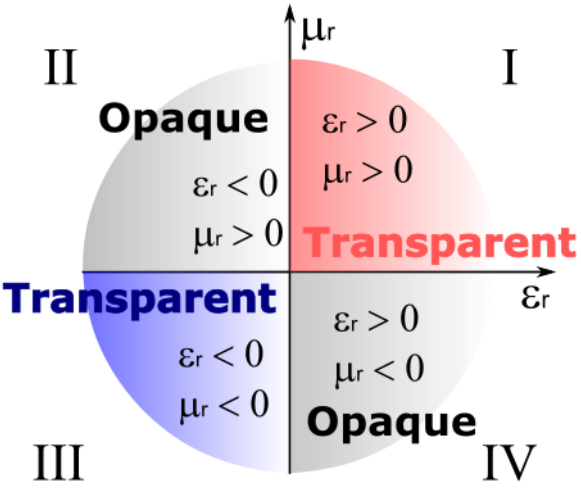

FIGURE 2.3: Materials classification at optical frequencies according to the sign of ϵ_r and μ_r. Materials of quadrants I and II can be found in nature. No naturally occurring materials have been reported in quadrants III and IV in the optical regime

Figure 2.3 shows a quadrant diagram classifying light-matter interaction according to the sign of ϵ_r and μ_r at optical frequencies. Since $\mu_r = 1$ in the optical regime, naturally occurring materials at high frequencies are located in the upper half of the diagram, where μ_r is always positive, and ϵ_r can be either positive or negative. Quadrant I contains the major part of isotropic dielectrics and semiconductors, as well as metals above the plasma frequency, where both permittivity and permeability have positive values. As stated previously, propagation of light is therefore allowed, resulting in materials belonging to this quadrant being transparent to radiation. Quadrant II is dominated by metals below the plasma frequency ($\epsilon_r < 0$ and

$\mu_r > 1$), resulting in light being reflected. At optical frequencies, quadrants III and IV are unoccupied: no natural materials with simultaneous negative ϵ_r and μ_r values (or negative μ_r only) have been reported so far in the optical regime [5]. Quadrant IV is however filled by diamagnetic materials where $\mu_r < 0$, but only at low (below the GHz regime) frequencies [82].

The electrodynamics of hypothetical materials with simultaneous negative ϵ_r and μ_r values were theoretically investigated for the first time in 1967 by Victor G. Veselago [84]. In his work, Veselago predicted various exotic electromagnetic effects emerging from this condition. For example, he pointed out that if ϵ_r and μ_r are both negative, then an EM wave can propagate through media with a negative group velocity. That is, $\vec{E}$, $\vec{B}$ and the wave vector $\vec{k}$ forming a set of orthogonal vectors that follow the left-hand rule, which results in the energy flux (defined by the Poynting vector $\vec{P}_t$) having opposite direction with respect to $\vec{k}$. For this reason, Veselago referred to this hypothetical materials as "left-handed", and his terminology is still being used by the scientific community nowadays [85]. Within the various consequences of this effect, perhaps the most well known phenomenon is negative refraction [5, 86], where light would theoretically bend towards the opposite direction (*cf.* natural materials) when encountering an air/material interface.

At the time of Veselago's work, the concept of left-handed materials was something purely abstract, since no natural materials having this property exists. Veselago's findings therefore passed unnoticed. In the next sub-sections, we will see how his research recovered the attention from the scientific community in 2000, due to the development of artificial materials (nowadays known as metamaterials). We will see as well how metamaterials and metasurfaces can effectively be designed to fill quadrants III and IV from **Figure 2.3**, and overcome the fundamental limits of naturally occurring materials, thus paving the way for a new class of electromagnetic phenomena and devices.

2.2 Metamaterials: A brief historical review

In the last two decades, engineered materials have gained a lot of attention from the scientific community due to their extraordinary properties (some of them not found

in nature) [6, 86, 87, 88, 89]. These artificial structures – now commonly known as metamaterials— have the potential to circumvent the fundamental limitations of natural materials, where the electromagnetic (EM) response is dictated by a particular atomic arrangement. As briefly mentioned in **Chapter 1**, metamaterials are structured materials made of subwavelength inclusions, which can be either periodically or randomly distributed [5]. Such building blocks (often known as meta-atom) can be specifically designed to engineer the macroscopic EM response on demand.

Metamaterial technology began with J. B. Pendry and his research for novel negative permittivity artificial materials at the end of the 90's [90]. In his work, Pendry showed (both numerically and experimentally) that an extended 3D array of deeply subwavelength sized thin wires can be designed to have an effective plasma frequency located in the GHz regime (microwaves). That is, several orders of magnitude lower with respect to naturally occurring metals, which typically have a ω_p located in the UV or visible spectrum [5, 81]. **Figure 2.4a** shows a diagram of the proposed artificial medium. By engineering the dimensions and/or spacing of the air-surrounded wires, Pendry and his group showed on-demand artificial control over the effective electron density, resulting in effective plasma frequencies and negative permittivities ε_{reff} at microwave frequencies [90]. Despite the term "metamaterial" was not employed at that time, the concept of creating artificial electromagnetic structured materials with properties beyond nature was demonstrated for the first time.

After successfully demonstrating the use of engineered materials to generate unusual effective electric responses, and motivated by the poor variety of magnetic response of natural materials at GHz and higher frequencies, Pendry started to investigate analogue magnetic artificial materials. In 1999, he theoretically showed that structured media can also be exploited to engineer effective permeabilities at will [91]. By making the constituent building blocks resonant, the effective magnetic permeability μ_{eff} can be severely enhanced via excitation of magnetic induction, and even take negative values when the excitation frequency is close to the natural frequency [91, 92]. Here, the proposed structural material is made of a pair of subwavelength concentric copper rings with splits at their opposite ends, named split ring resonators (SRR). The SRR are arranged in a cubic 3D lattice as depicted

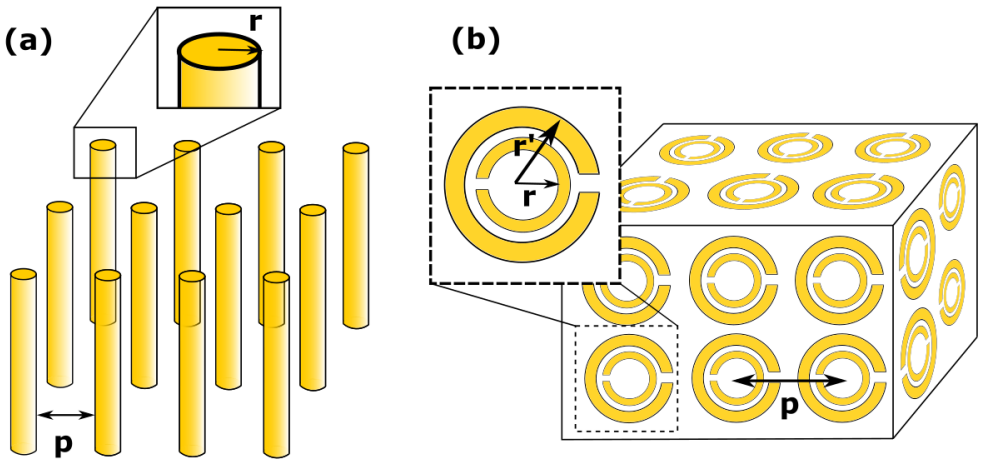

FIGURE 2.4: Diagrams of the first artificial EM materials. **(a)** An array of deeply sub-wavelength sized metal wires utilised for engineering the effective relative permittivity, and thus reduce the plasma frequency to the GHz regime (re-adapted from [90]). **(b)** A 3D cubic lattice of split ring resonators, employed to generate on-demand effective relative permeabilities (re-adapted from [91]).

in **Figure 2.4b**. When excited with an EM wave, harmonic magnetic fields induce resonant current loops in the rings, which generate their own magnetic flux which can enhance or oppose the incident flux. Here again, by appropiately engineering the geometrical parameters of the rings, Pendry et al. theoretically showed that SRRs can exhibit artificial magnetisation, thus effective magnetic permeabilities [91] which can be pre-designed to values not (or rarely) found in natural materials, including negative effective permeability.

The term metamaterial started to become popular after the first experimental demonstration of artificial electromagnetic structures with simultaneous negative ε_{reff} and μ_{reff} values. The credit goes to David Smith and his research group, inspired by Pendry's research on artificial materials described above. In his work, Smith suggested and experimentally validated that the combination of negative-permeability split ring resonator media with negative permittivity thin metallic wires, previously demonstrated by Pendry's group, results in a left-handed material with negative group velocity [90, 91, 92, 93]. Smith's findings are summarised in **Figure 2.5**. As depicted in **Figure 2.5a**, the structure consists of a three-dimensional array of copper split ring resonators with a thin copper wire parallel to the z axis. The left-handed nature of such a structure was demonstrated via investigation of two different metamaterials separately: one consisting of arrays of copper SRRs only,

and a second one with a combination of copper SRRs combined with thin copper wires. **Figure 2.5b** shows the dispersion curves obtained for with both approaches. In the case of SRR-only metamaterial (i.e. without metal wires), a forbidden band (highlighted in yellow) in which EM waves are not allowed to propagate was observed around 10.5 GHz. This was attributed to an imaginary wave number as a consequence of an effective negative permeability. The addition of copper wires (specifically designed to have negative permittivity) to the SRRs structure "opens" the frequency band gap originated by the SRR-only medium, which indicates propagation of EM waves in the previously-forbidden band, and thus suggesting double-negative condition where $\varepsilon_{reff} < 0$ and $\mu_{reff} < 0$.

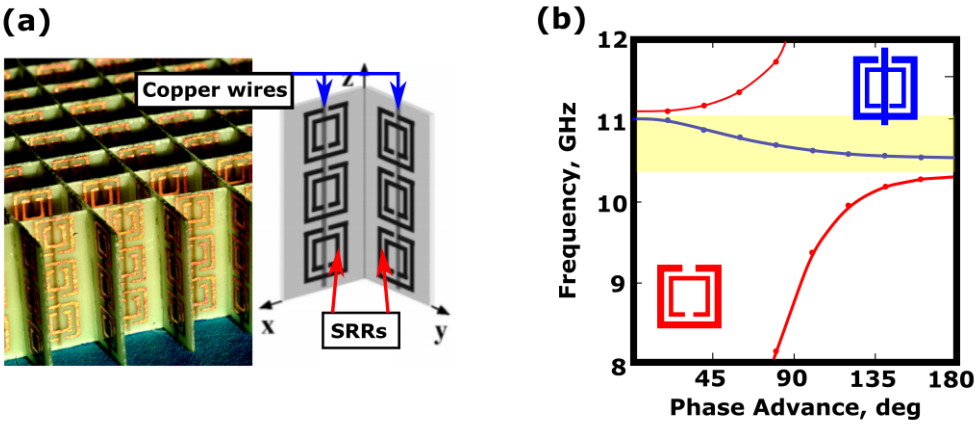

FIGURE 2.5: First left-handed metamaterial cell reported by Smith's group (re-adapted from [93]). **(a)** Schematics of the unit consisting of a combination of copper split ring resonators and a copper wire along the Z axis. **(b)** Dispersion curve for a split ring resonator (red) showing a forbidden band around 10.5 GHz, which "opens" when combined with a metal wire (blue).

Since Smith et al. reported the first left-handed artificial material theoretically investigated by Veselago [84], metamaterials have gained a lot of attention from scientists around the world. It was soon pointed out that metamaterials can be engineered not only to produce negative refraction, but also a wide range of unusual and exciting properties not or rarely found in nature in different parts of the EM spectrum [89, 94, 8]. This metamaterial "scientific avalanche" took place alongside an improvement of micro and nano-fabrication techniques. Such a parallel technological development rapidly paved the way to the first artificial materials working in the infrared spectrum [6], and finally in the optical regime, where the sizes of the building blocks or meta-atoms fall in the nanometer scale [95].

2.3 Optical metasurfaces: State of the art

Shrinking of 3D metamaterials from the microwave to the optical regime has become a reality thanks to the evolution of nano-fabrication fabrication techniques, such as electron-beam lithography, focused-ion beam milling, and nanoimprint lithography [96]. However, such structural re-scaling is still nowadays challenging: first due to complicated 3D fabrication procedures at the nanoscale, and second; due to strong plasmonic losses from metallic nanostructures occurring at optical frequencies which limits the range of applications. Two-dimensional metamaterials or metasurfaces have emerged as an alternative to overcome this issues, since:

- Removing the third dimension allows the reduction of plasmonic losses in the direction of light propagation [75], thus improving efficiency when needed.
- Fabrication complexity is reduced, since a single lithography step combined with thin film deposition techniques is typically sufficient for a successful device realisation [6, 96, 97].

Such flat metasurface arrays consist of subwavelength resonant elements which can be designed to achieve local manipulation of the amplitude, phase and polarisation of light [6], via engineering of their geometry and/or material properties. These capabilities can be therefore exploited to provide full control of the reflected and transmitted waves, paving the way, as summarised in **Figure 2.6**, to the development of a new class of compact photonic devices with novel and exotic functionalities; such as super absorbers, frequency selective surfaces, beam steerers, flat lenses, polarisers, vortex beam generators, or holograms [8]. In fact, most of such functionalities were already reported in the RF and MW regimes even before the demonstration of first metamaterials in 2001. For example frequency selective surfaces and absorbers operating at RF and MW frequencies emerged in the 70's [98, 99], and beam steering and flat lensing (named reflectarrays and transmitarrays in RF and MW terminology) were already employed by the end of the same decade [100]. Metasurfaces can be therefore seen in some way as a shrinking of RF array technology to the optical regime. Since metals do not behave as perfect electric conductors below microwave wavelengths, perhaps the main difference between both

relies on the generation of surface plasmons when using metallic meta-atoms at optical frequencies [75]. This is due to collective coherent oscillations of free electron clouds arising from electric field penetration at the surface of the metal [75]. As a result, linear scaling of the element sizes from the MW to the optical regime fails, since the scaling becomes proportional to the wavelength of the surface plasmon (λ_{sp}) instead of the free-space wavelength (λ_0) [97, 101]. As mentioned before, this effect is also accompanied by an increase of ohmic (plasmonic) losses at optical frequencies, which might be actually of benefit for some devices such as super absorbers for e.g. photovoltaics, but can be detrimental for other applications where light re-radiated to the free-space needs to be kept to a maximum (e.g. like optical switches or beam steering devices).

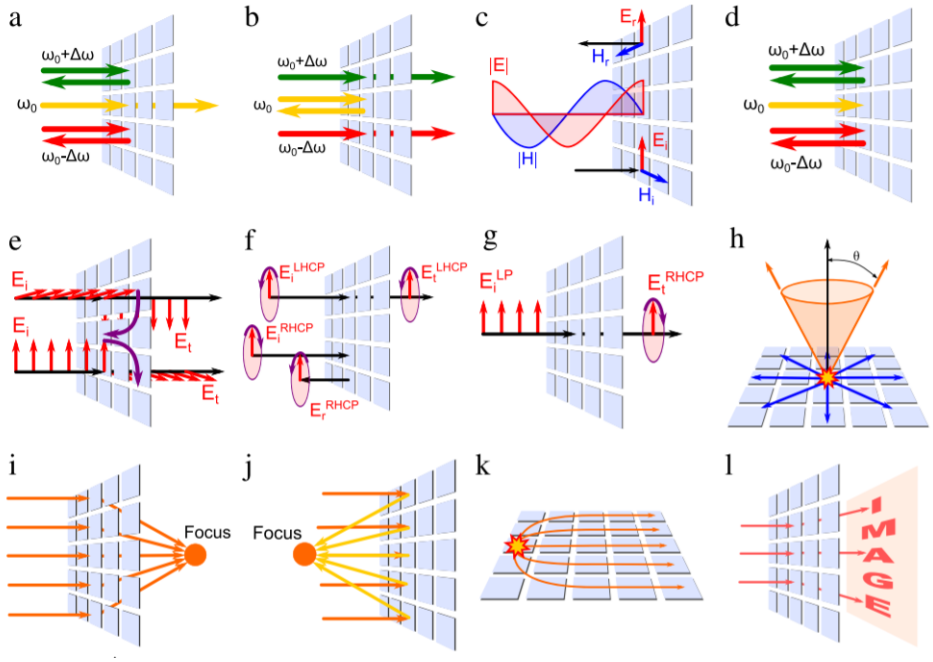

FIGURE 2.6: Examples of functionalities offered by metasurfaces (reproduced from [8]). **(a-b)** bandpass frequency selective surfaces in transmission and reflection. **(c)** Highly reflective surface. **(d)** Perfect absorber. **(e-g)** Polarisers and polarisation sensitive frequency selective surfaces. **(h)** 2D leaky-wave antenna. **(i-j)** Flat lenses in reflection and transmission. **(k)** Flat Luneburg lens. **(l)** hologram.

Despite the wide range of functionalities offered by metasurfaces (**Figure 2.6**), the majority of them can be in general built employing three main types of basic resonant structures (i.e. unit cells or meta atoms) which can be either one or two-dimensional, isotropic or anisotropic; and whose intrinsic physical mechanisms vary from structure to structure. That is, as schematised in **Figure 2.7** and discussed further below:

a) Metallic or plasmonic meta-atoms:

Metallic meta-atoms are subwavelength particles typically made of noble metals, whose optical properties are due to the plasmon resonances supported by their specific geometry and material properties. Some examples of typically employed geometries are shown in **Figure 2.7a**, including V-shaped antennas, split ring resonators, metal/insulator/metal (MIM) gap plasmon resonators and Babinet-inverted metal/insulator antennas. When such structures are excited with time-varying harmonic electric fields (i.e. EM waves), free electrons are displaced causing an in-plane effective dipole moment, with a subsequent depolarising field analogous to a restoring force [5, 102]. Such a collective motion can be described as a Lorentz oscillator, just like in natural atoms whose electrons are bound to the nucleus (as described in the first section of this chapter). In addition to in-plane electric dipole excitation, some specific geometries such as V-shaped, SRR and MIM antennas can also support out-of plane magnetic dipole inductions, even at optical frequencies. This phenomenon is known as artificial optical magnetism [103, 104], and can be generated via anti-parallel conduction currents associated to the time-varying electron motion within the plasmonic particle [102]. These resonant behaviours provide the basic operating principles of many metasurfaces with different functionalities reported up to now [5, 6, 102], some of which will be reviewed in more detail in section 2.3.1.

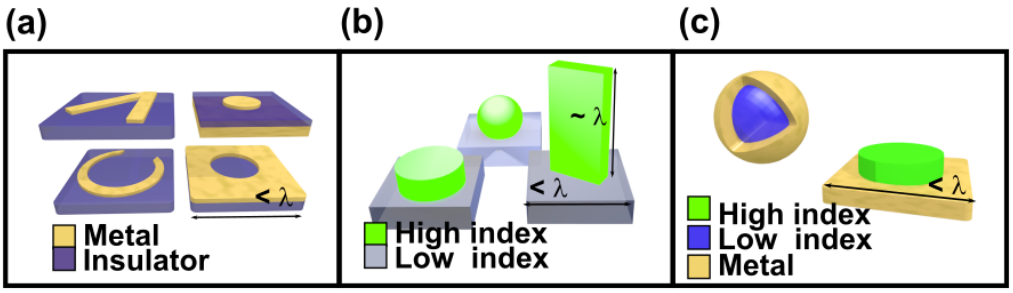

FIGURE 2.7: Examples of different type of unit cells or meta-atom configurations. **(a)** Plasmonic, **(b)** All-dielectric, and **(c)** Hybrid dielectric/plasmonic.

b) All-dielectric meta-atoms:

All dielectric meta-atoms are nanoparticles made of high refractive index dielectrics

such as, typically, silicon, hydrogenated silicon, gallium phosphide or titanium dioxide; surrounded by a low index medium like air or silica [88]. As depicted in **Figure 2.7b**, such structures typically consist of subwavelength building blocks having different geometries, as well as truncated nano waveguides (e.g. nanorods or nanopillars) where only the dimension in the propagation direction is larger than the wavelength [105]. Excluding the latter case, the resonant behaviour supported by all-dielectric metasurfaces is somehow analogous to plasmonic metasurfaces, since they can also support electric and magnetic dipole (as well as higher order) moments [88]. Nevertheless, the main difference between both approaches relies on the origin of such dipoles, which is driven by displacement currents, rather than, as in the case of more conventional metal plasmonic metasurfaces, by conduction currents [88, 104]. As a result, dielectric meta-atoms can exhibit very high scattering efficiencies due to the absence of ohmic (plasmonic) losses inside the particle. Furthermore, by engineering the relative phase and amplitude of the electric and magnetic resonances (which can be done by optimising their geometry), a 2π optical phase control becomes accessible in transmission, with nearly 0% of light being back scattered (reflected) [106, 107]. Such key features makes from this configuration a very attractive platform for applications based on wavefront engineering such as flat lensing or beam steering [108].

c) Hybrid meta-atoms

Hybrid meta-atoms consist of subwavelength elements whose resonant behaviour arises from the combination of plasmonic and dielectric meta-atoms described above, thus electric and magnetic dipole moments are generated via both conduction and displacement currents. The most commonly employed structures are depicted in **Figure 2.7a**, and consist of core-shell nanoparticles in the form of low-index dielectric spheres coated with metals such as gold or silver [109], or high index dielectric resonators on top of a plasmonic metal plane (e.g. TiO_2 cylinders on silver) [45, 110, 111].

As we will see in the upcoming sections, the choice of a specific configuration depends on the desired functionality, application and design specifications. An in-depth analysis of the physical mechanisms of the above-described architectures, as

well as a review of all their functionalities would be very extensive, and outside of the scope of the results discussed in **Chapters 4, 5** and **6**. Hence, the following sub-sections will focus on reviewing the state of the art and physical mechanisms of nano-particles employed only for wavefront engineering, as well as for absorbing metasurfaces (for being more relevant to the content of this thesis).

2.3.1 Absorbing metasurfaces

The generation of losses at particular optical wavelengths or spectral bands is currently a target functionality for a wide range of applications going from photovoltaics to optical telecommunications or displays. Over the last decade, plasmonic metasurfaces, particularly in their metal/insulator/metal form; have been widely employed for this purpose [7, 47, 112]. Such configurations are commonly known as gap-surface-plasmon (GSP) metasurfaces, and as briefly described previously, their optical properties rely on the surface plasmon resonances supported by their specific geometry, as well as their constituent and surrounding materials [102, 75]. **Figure 2.8** shows a diagram of the typical gap plasmon metasurface, whose unit cell consists of a dielectric layer sandwiched between a continuous metal plane and a patterned metal antenna. When excited with harmonic electric fields, the charge motion induced in the top antenna is imaged at the bottom plane, thus generating anti-parallel currents with a subsequent magnetic dipole induction [113, 114].

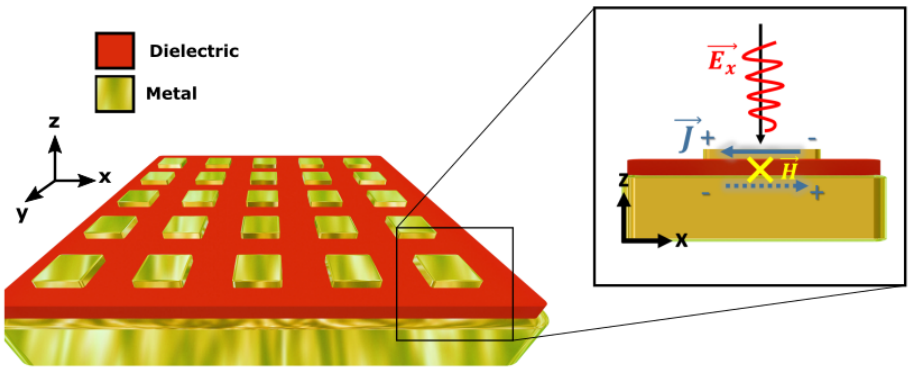

FIGURE 2.8: Schematics and working principle of a typical gap-plasmon metasurface

Because of the finite width of the top antenna, first and higher order standing wave GSP modes can be generated via changing its width. The resonant positions

can be therefore approximated by a simple Fabry-Pérot (FP) model [113, 115, 116, 117]:

$$wk_0 n_{GSP} = m\pi - \Delta\phi \tag{2.18}$$

where w is the strip width, n_{GSP} is the real part of the effective mode index of the GSP (which depends on the geometry and optical properties of the involved materials), m is an integer defining the order of the GSP mode, and $\Delta\phi$ is the optical phase shift acquired upon reflection [56, 117].

In analogy to FP cavities where a fraction of light is reflected by the first interface without coupling to the structure, when GSP metasurfaces are excited with EM waves only a fraction of the wave is coupled to the structure and thus part of the wave energy is reflected without interacting with the cavity. The resulting optical response arises from the superposition of both contributions, and depends on the so-called coupling coefficient (C_c), which is the ratio between the energy not coupled to the structure (external losses) and the energy dissipated inside the resonator (internal losses) [118, 67, 7]. When the external and internal losses are equal in amplitude, the metasurface reaches the critical damping (or critical coupling) condition (where $C_c = 1$), which provides the fastest approach to zero amplitude due to the superposition principle [118]. This unique solution gives way to two additional regimes:

- When the internal losses are higher than the internal losses (hence $C_c < 1$), the system is underdamped or overcoupled. This regime is characterised by a continuous near 2π optical phase control with high efficiency, which becomes accessible when the system is detuned from its resonant frequency (e.g. via varying the width of the top antenna). [117, 118].

- On the other hand, when internal losses are smaller than the external losses (thus $C_c > 1$), the resonance falls in the so-called overdamped or undercoupled regime, where only a π phase coverage is accessible.

The above described resonant regimes are indeed the same as those exhibited by classical Fabry Perot cavities and Gires-Tournoi etalons [67, 119], and can be used for different design purposes such as amplitude or phase control (see **Appendix A** for a

detailed analytical study of FP resonant regimes). For perfect absorption, however, the target design objective is the critical coupling condition where all the incoming light is absorbed by the system. One of the first (if not the first) experimental demonstrations of super-absorption employing GSP structures at optical wavelengths dates from 2009. The credit goes to H. Giessen and his group [120], who developed a perfect plasmonic absorber working at $\lambda_0 = 1600$ nm. The MIM configuration employed together with a false colour SEM picture are depicted in **Figure 2.9a**. It consists of a magnesium fluoride (MgF_2) film sandwiched between a continuous gold plane and a top patterned metasurface in the form of gold nano-disks. As shown in **Figure 2.9b**, an excellent agreement in the reflectance and absorbance spectra between simulations and experiments was achieved, with nearly perfect absorption (99%) at $\sim$ 188 THz ($\lambda \sim 1600$ nm). Furthermore, the authors suggested biological sensing as a potential device application, due to a change in the resonance position when changing the refractive index of the surrounding medium (from air to water in **Figure 2.9b**).

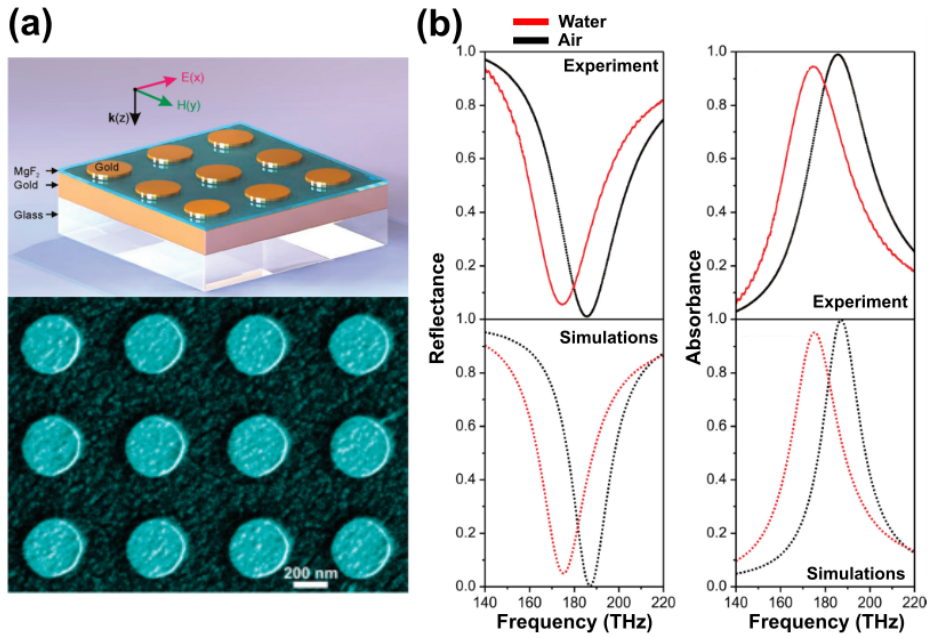

FIGURE 2.9: **(a)** Schematics of the perfect absorber reported by Giessen's group [120] (top), and SEM image of the fabricated device. **(b)** Experimentally obtained Reflectance (left) and absorbance (right) spectra for different surrounding media compared to simulations.Reproduced and re-adapted from [120].

Since then, a substantial amount of related work on super absorber structures

working at different optical frequencies has been carried out employing MIM arrangements [121]. More recently, such structures have been combined with tunable materials such as liquid crystals [122] or phase-change materials [76, 7], to provide reconfigurable amplitude control with different application purposes, going from optical signal modulation [7] to reconfigurable colour displays [76].

2.3.2 Metasurfaces for wavefront engineering

Optical metasurfaces for phase control share the essence of the well established reflectarray antenna technology used in the radio frequency and microwave regimes, where the phase of an input beam is locally controlled by means of resonant elements (antennas) to generate a particular output wavefront. In the case where arrays of meta-atoms are smaller than the wavelength, but are sufficiently well-separated to avoid strong near-field coupling between them, the phase of optical beams can be locally tailored by detuning individual elements from their resonant frequency (e.g. via variation of the geometrical parameters) [6, 102]. Such systems can be therefore employed to mimic the wavefront engineering capabilities of conventional optics without the need of bulky geometries, as their optical phase control capabilities rely in discretised abrupt phase jumps coming from subwavelength resonant elements (instead of propagation effects as in bulky optics).

These kind of structures are known as phase-gradient metasurfaces, and the design rules to generate a particular wavefront are governed by the generalised Snells law [6], which in one dimension (and in reflection and transmission respectively) is given by:

$$sin\theta_r - sin\theta_i = \frac{1}{n_i k_0}\frac{d\phi}{dx} \tag{2.19}$$

$$n_t sin\theta_t - n_i sin\theta_i = \frac{1}{k_0}\frac{d\phi}{dx} \tag{2.20}$$

where n_i and n_t are the refractive indices of the incident and transmission media respectively, θ_i and θ_r the incident and transmitted angles with respect to the surface normal; dx is the width of the meta-atom cell, and $d\phi$ is the phase delay introduced by the meta-atom. Such expressions can be derived via Fermat's principle, imposing a stationary phase condition between two infinitesimally close optical paths along

an interface with local phase discontinuities [6]. What this simple set of equations tell is that the local direction of a beam (and thus the local wavefront orientation, which is perpendicular to the beam direction) depends on the phase delay imposed over a discretised subwavelength distance (dx). This is of course obviating the other parameters involved in the classic form of Snells' law (i.e. angle of incidence θ_i and refractive indices of the media n_i and n_t) [4]. Due to their capability to provide abrupt phase jumps over subwavelength regions using flat geometries, phase-gradient metasurfaces can be therefore exploited to create a variety of novel and compact photonic devices, such as holograms, [123] or flat focusing lenses/mirrors (Fig. 1b)[6]. Despite a 2π optical phase control being not necessary for the successful realisation of certain devices, having a designer interface which offers a full 2π phase span is highly desirable, as it increases the flexibility of realisable designs [6]. Perhaps one of the most explored optical effects using phase-gradient metasurfaces is based on the so-called anomalous reflection (or refraction),[6, 124, 125, 126] which is employed to deflect a beam at a direction different from ordinary reflection (i.e. $\theta_i \neq \theta_r$). As depicted in **Figure 2.10a**, this can be achieved via imposing a constant linear phase shift $\Delta\phi$ across the surface, which in reflection and in 1D is given by:

$$sin\theta_r = \frac{\lambda_0 \Delta\phi}{2\pi d} + sin\theta_i \tag{2.21}$$

Another utility of phase-gradient metasurfaces relies on their capability to yield flat lenses [6, 110]. Here, a parabolic spatially varying phase is imposed across the surface via appropriate distribution of the the scatterers. Such a phase profile is indeed the same aimed when designing Fresnel lenses, where local phase shifts are induced by optical path differences emerging from its characteristic concentric prisms. The required spatial phase profile can be easily calculated depending on the desired focal length f via:

$$\phi(x, \lambda) = \frac{2\pi}{\lambda_0}\left(f - \sqrt{dx^2 + f^2}\right) \tag{2.22}$$

Accordingly, the numerical aperture can be finally defined with the effective lens area (i.e. the diameter of the lens D) via:

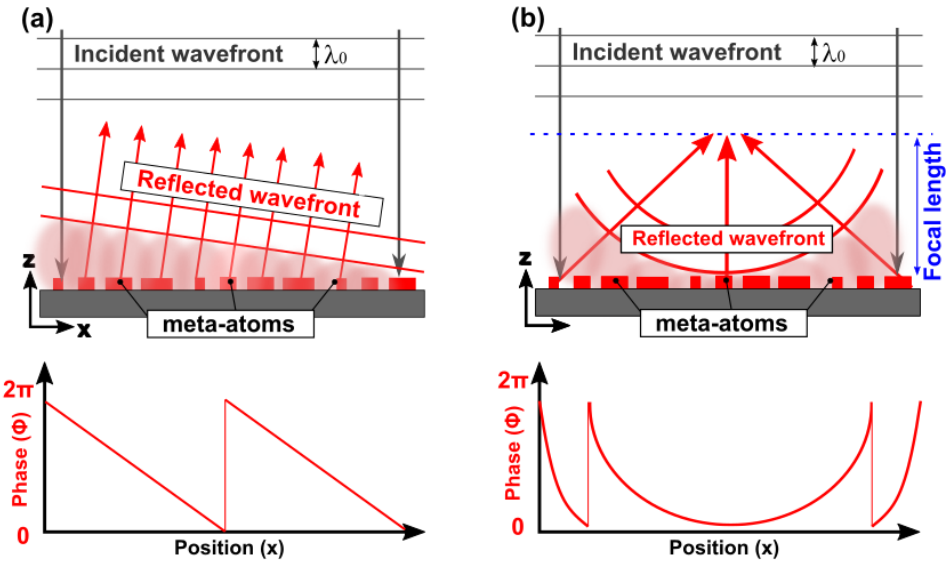

FIGURE 2.10: **(a)** Wavefront reconstruction employing Huygens' principle (top) and spatial variation of the discretised phase (bottom) for: **(a)** Beam steering metasurfaces, where the phase profile is tilted as a result of a constant phase gradient across the x-axis, **(b)** focusing mirror, where the phase profile is parabolic.

$$NA = sin\left(tan^{-1}\left(\frac{D/2}{f}\right)\right) \tag{2.23}$$

In addition to beam steering devices and flat lenses, other type of functionalities can be achieved employing phase-gradient metasurfaces, including flat holograms or vortex beam generators having different topological charges [6, 125]. The first experimental demonstration of this technology was carried out by Capasso's group in 2011 [125]. As shown in **Figure 2.11a**, the use of gold V-shaped antennas supporting both symmetric and antisymmetric modes (according to their current distributions) was proposed as a way to span a full 2π phase coverage of the cross-polarised scattered fields. This was achieved via changing the length and relative orientation of the antenna arms with respect to the electric field component of the incident light, thus allowing for the excitation of both resonant modes under a fixed polarisation direction [6, 125, 127] (**Figure 2.11b**). Such an elementary unit cell was then used as a building block to create a series of devices in order to prove its wavefront engineering capabilities, including vortex beam generators, beam steering metasurfaces and flat lenses operating in the long-wave infrared (LWIR) spectral regime. **Figure**

2.11c shows an SEM image of one of the realised devices, consisting of a beam steering working in transmission. Here, V-shaped antennas were arranged in a super cell made of 8 elements to impose a constant cross-polarised 1D linear phase-gradient of 45 ° along the surface. As it can be seen from the measured angular transmittance under normal incidence (in **Figure 2.11d**), the fabricated devices exhibited broadband (from $\lambda = 5.2\ \mu m$ to $\lambda = 9.9\ \mu m$) beam-steering capabilities. This was attributed to the low cross-polarisation conversion efficiency and thus low quality factors (and large bandwidth) of the V-antenna resonant modes, which in turn resulted in a reduced overall beam steering efficiency. Efficiencies relative to ordinary refracted light (i.e. at $\theta_t = 0°$ for an angle of incidence of $\theta_i = 0°$) were found to be around 30%, with absolute steering efficiencies below 10% [127].

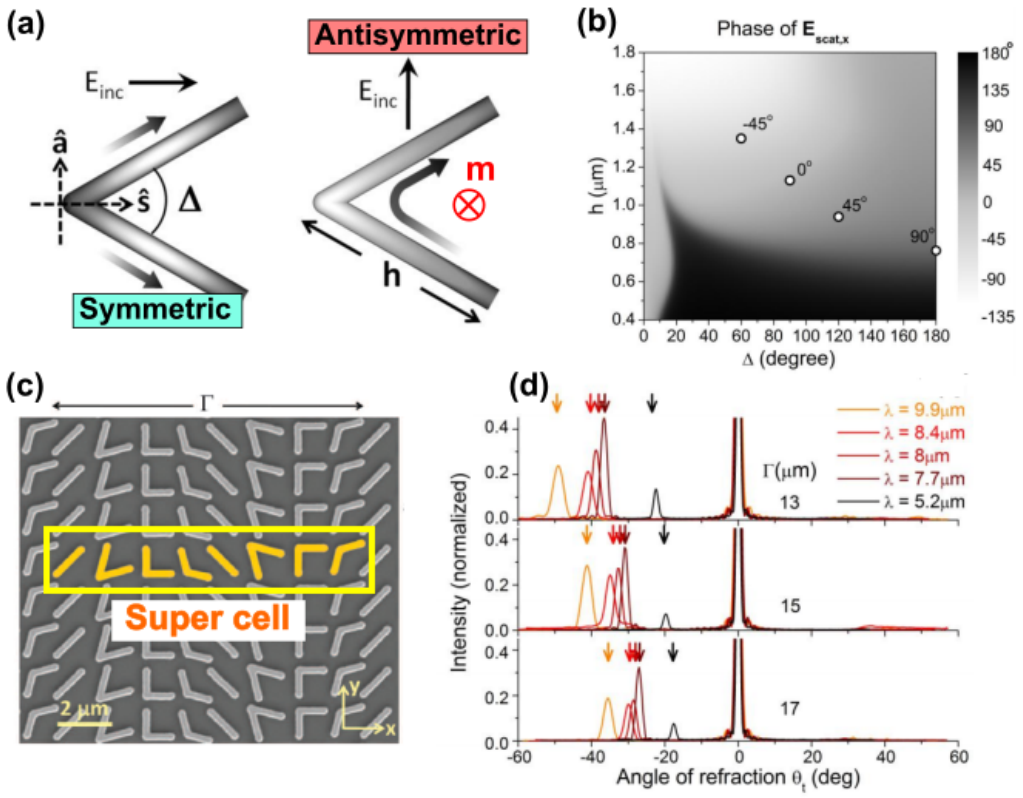

FIGURE 2.11: **(a)** Resonant modes supported by the V-shaped gold antennas developed by Capasso's group, where symmetric and antisymmetric states can be excited depending on the relative orientation between the incoming electric field and the antenna. **(b)** Phase of the cross-polarised scattered electric field as a function of the angle between the antenna arms Δ and the arm length h. The cobmination of symmetric and antisymmetric states gives raise to an entire 2π phase coverage. **(c)** SEM image of the fabricated metasurface (the super-cell made of 8 elements is highlighted in yellow. **(d)** measured angular transmission spectrum at different wavelengths under normal incidence, going from $\lambda = 5.2\ \mu m$ to $\lambda = 9.9\ \mu m$. Images reproduced and re-adapted from [127].

In spite of the low efficiency of V-shaped antennas reported by Capasso's group [6, 127], this work provided an excellent proof of concept towards the creation of flat optical components, and therefore inspired new research trends based on the same working principle [111, 128, 129]. Improved designs were quick to follow with the introduction of meta-atoms highly inspired by reflectarray RF and MW technology. That is, metal-insulator-metal (or GSP) meta-atoms described in the previous section. In addition to perfect absorption capabilities [7, 120], such structures can be designed to operate as highly efficient phase-shifters if their resonant behaviour falls in the underdamped (overcoupled) regime [118]. Contrary to V-shaped antennas, transmission is here completely suppressed, due to the presence of a metallic bottom plane. As a result, the conversion efficiency (i.e. the amount of light phase-shifted and re-radiated to the free space) can be significantly improved, with experimental efficiencies up to 80% in the near infrared when metals are the only source of optical losses [129]. Furthermore, if the resonant elements are isotropic, reflected waves preserve the same polarisation with respect to the incident wave, which can be regarded as an advantage for certain applications requiring polarisation insensitivity [129]. GSP metasurfaces are therefore an excellent platform to achieve versatile wavefront control with high efficiency, but perhaps have the small drawback of being limited to operate in reflection, as well as exhibiting degradation of the optical performance when approaching to visible frequencies (due to an increase of the plasmonic losses).

Theoretically, similar (and even better) beam control efficiencies could be achieved using all-dielectric meta-atom configurations operating in transmission [88]. As briefly introduced in the previous section, such structures can also support electric and magnetic dipole (and higher order) modes. However, contrary to the plasmonic approach where dipoles are originated via conduction currents, all-dielectric resonant behaviours are fully originated by strong displacement current loops confined inside the body of high refractive index subwavelength particles embedded in a low-index matrix [106, 130]. As a result, field interactions are free from ohmic losses, which gives raise to much better scattering efficiencies. **Figure 2.12a** shows the typical electromagnetic field distribution of magnetic (left) and electric (right)

dipole modes supported by arrays of silicon nano-disks. Via engineering the relative phase and amplitude of such resonances (which can be done via optimisation of the meta-atom geometrical parameters), it is possible to e.g. suppress back scattering radiation at one specific frequency, resulting in 100% of light being transmitted. Such phenomenon is known as the first Kerker condition [106], and it is characterised by a continuous 2π optical phase coverage with efficiencies potentially up to 90% in transmission [107], driven by small modifications of the disk radii (**Figure 2.12b**). Therefore, in analogy to Capasso's V-shaped antennas, one can arrange all-dielectric meta-atoms of different sizes to engineer optical wavefronts at will, but with the advantage of having access to superior efficiency: first due to the abscence of plasmonic losses, and second due the co-polarising scattering properties of such structures under normal incidence [131]. For example, in [132], Yu et al. showed both numerically and experimentally that arrays of properly arranged silicon nanodisks operating under the Kerker regime (**Figure 2.12c**) can be used to steer optical beams in transmission with absolute theoretical and experimental efficiencies of 85% and 50% respectively (**Figure 2.12d**).

Other approaches to wavefront engineering have been proposed during the evolution of phase-gradient metasurfaces. This includes meta-atoms with non-resonant phase-control capabilities (known as Pancharatnam–Berry meta-atoms)[133] where full phase control can be achieved by changing the orientation angle of antennas with identical geometry under circularly polarised excitation. Due to their non-resonant nature, Pancharatnam–Berry metasurfaces offer broadband operation capabilities, but on the other hand are limited to work under circular polarisation [133, 134]. More recently, arrays of TiO_2 truncated waveguides in the form of nanoposts or nanopillars having different diameters have been proposed to for the realisation of flat lenses in the visible spectrum, with focusing efficiencies above 70% [135].

In summary, phase-gradient metasurfaces are becoming a growing research field, due to their ability to yield optical components with non-bulky geometries. For this purpose, a wide variety of structures (meta-atoms) can be used to achieve discretised phase control over large areas, and thus produce different optical effects such as anomalous reflection, or flat lensing. Each meta-atom configuration has its own outstanding properties and limitations (e.g gap surface plasmon meta-atoms offers

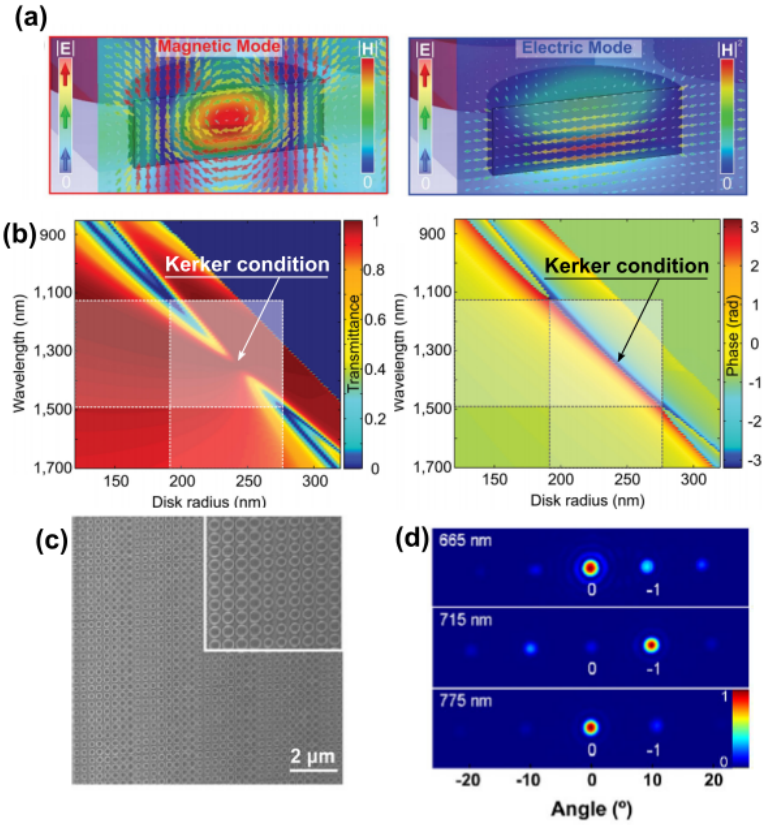

FIGURE 2.12: **(a)** Electromagnetic field distribution confined in a silicon nano-disk for the magnetic (left) and electric (right) dipole resonances [107]. **(b)** Transmittance spectrum (left) and phase in transmission (right) as a function of the cylinder radius. Dips in transmission correspond to the electric and magnetic dipole induction, and the region where both modes overlap (i.e. Kerker condition) is characterised by high transmittance with a 2π phase coverage [107]. **(c)** SEM image of silicon nano-cylinder arrays properly arranged to steer light at an angle of $\theta \approx 10$ ° [132] **(d)** Experimental resutls of the devices shown in **(c)**, where maximum steering efficiency is achieved at a wavelength of 715 nm [132].

high efficiency, but can only work in reflection). The designer interface needs to be therefore carefully selected depending on the design specifications [129].

2.4 Phase-change materials and their applications

2.4.1 Introduction to phase-change materials and their properties

There are many phase-change materials in nature which can switch reversibly between amorphous and crystalline phases as a function of the surrounding temperature. Perhaps the most simple example is water, which exhibits a liquid (amorphous) state at room temperature, but becomes solid (amorphous or crystalline) below 0 °C.

However, a smaller number of materials can exhibit both phases at a particular temperature value (e.g. silicon or TiO_2), from which only a few are accompanied by a sharp contrast in their physical properties: that is chalcogenide phase change materials (PCM). Such compounds are alloys containing elements from group VI-A of periodic table (typically sulphur, tellurium or selenium), and have been now used for a couple of decades in devices for non-volatile data storage such as re-writable optical disks [33] or electrical memories [136, 137]. Such a non-volatile storage concept is mainly based on their ability to switch between amorphous and crystalline states via appropriate heat stimuli; as well as to retain the required phase at room temperature. The amorphous to crystalline transition comes with abrupt changes in the electro-optical properties which can be of up to three times in the refractive index, and 5 orders of magnitude in electrical resistivity [33, 78]. Such outstanding properties and their potential to store data both electrically and optically were first reported by Ovshinsky in 1968 [138] and in 1972 [139] respectively.

Chalcogenide PCMs in their amorphous phase are typically characterised by having high electrical resistivity, as well as low optical losses (and lower refractive indices) below their energy bandgaps. On the other hand, high optical losses and low resistivity are typical characteristics of the crystalline phase. In addition, PCMs possess the ability to be switched between states (and indeed between intermediate states too) very quickly (nanoseconds or less) and reversibly, potentially up to 10^{15} cycles [78]. As summarised in **Figure 2.13**, the switching between structural phases is typically induced employing appropriate heat stimuli in the form of either optical or electrical pulses having different amplitudes and durations. Starting from the characteristic as-deposited amorphous state, the amorphous-to-crystalline phase transition is driven by large-duration, low-amplitude pulses [33]. Despite crystallisation being physically easy to achieve even over large material volumes, as highlighted in **Figure 2.13**, reamorphisation will only occur under specific physical constrains which might not be trivial to achieve. That is, the high temperatures needed for melting the material (melting temperatures T_m are generally around 600 °C for commonly used PCMs), together with the need for fast cooling rates (in the order of tens of °C/ns [33]) down to the glass temperature ($T_g \approx 200$ °C) to avoid material recrystallisation. Furthermore, due to the relatively low thermal conductivity of PCM

alloys ($\approx$ 0.5 W/mK at room temperature) [137, 140], reamorphisation over large volumes might simply become impossible due to thermal insulation (thus low cooling rates), or alternatively would require for a high power consumption [141]. As we will see in the next section where applications of PCMs are discussed in more detail, current memory devices are therefore based on the use of low PCM volumes integrated in thermally optimised environments to favour the cooling processes, while reducing the power consumption and increasing the storage capabilities [78, 142, 143].

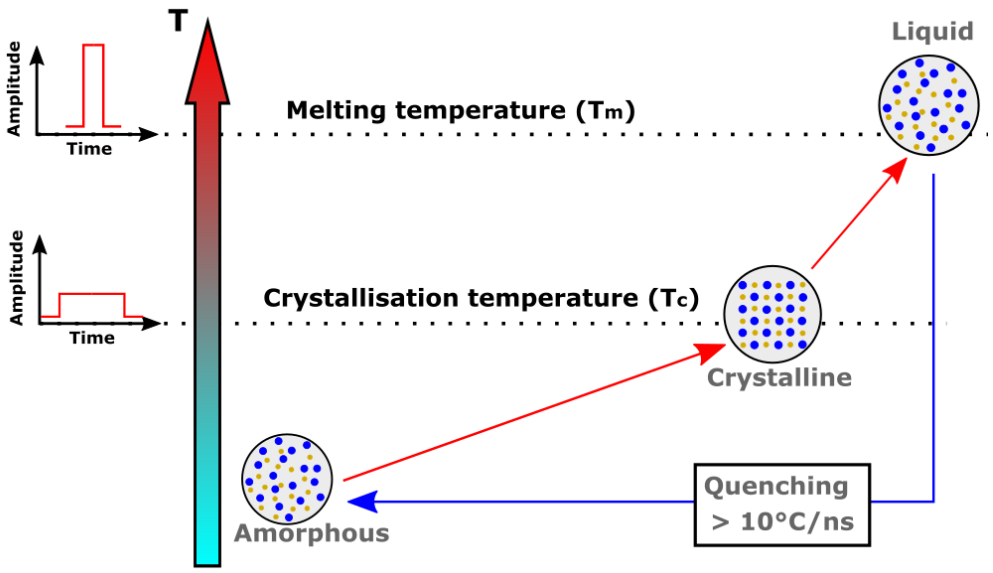

FIGURE 2.13: Crystallisation and reamorphisation conditions for a successful phase-change transition. Long duration, low amplitude optical or electrical pulses are typically used to heat the material above its crystallisation temperature. A short pulse of high amplitude is then used melt the material. For a successful reamorphisation process, the liquid phase needs to be cooled down at rates of at least 10 $^{\circ}$ C/ns.

The research for novel PCM compositions with improved properties is currently commonplace towards the development of more-efficient memory devices. That is, synthesising new PCMs alloys with enhanced phase transition speeds, larger optical and electrical contrast between states, and higher number of reversible transitions [33]. Within the current available PCMs, chalcogenide phase-change materials, particularly those based on GeSbTe or GeTe combinations are arguably the most widely employed. **Figure 2.14** shows the real and imaginary parts of the relative permittivity function (here named ϵ_1 and ϵ_2 respectively) of some commonly

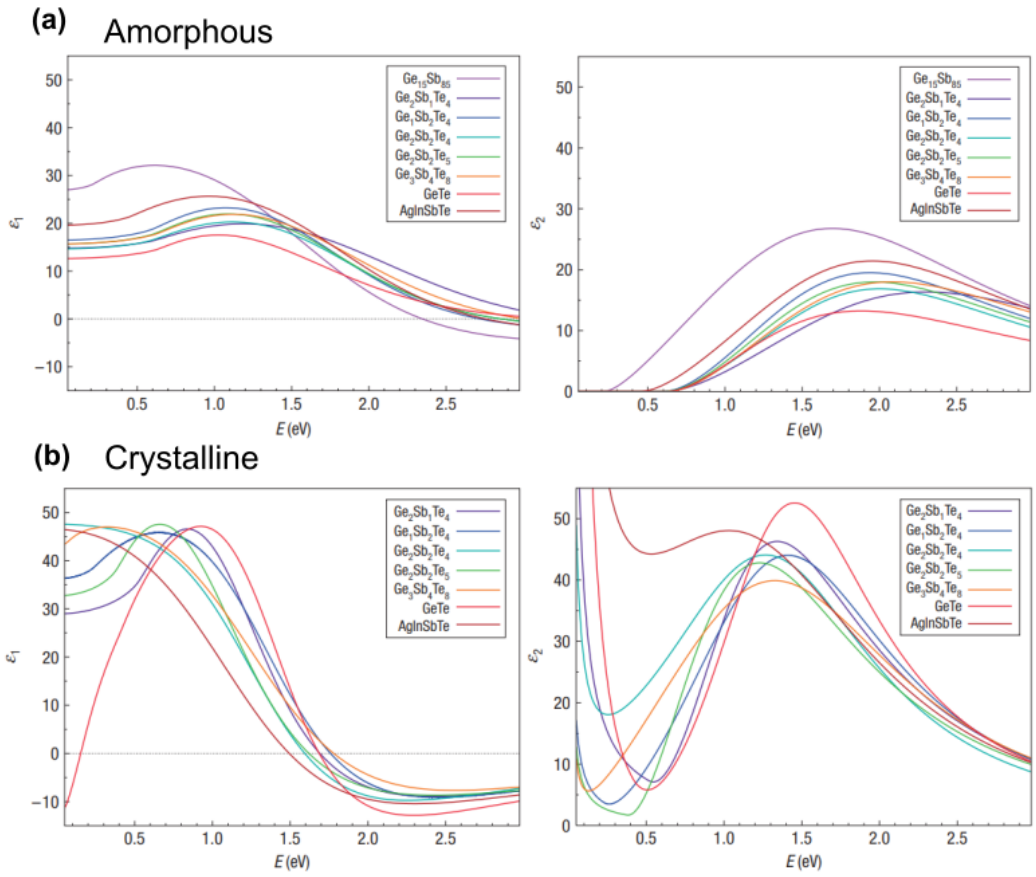

FIGURE 2.14: Real (left) and imaginary (right) parts of the permittivity function for various PCM compositions for **(a)** amorphous, and **(b)** crystalline states. Plots reproduced from [77].

employed compositions [77]. As it can be intuited from this plots, such PCM alloys are semiconductors having different bandgaps for amorphous and crystalline phases. Their typical energy bangaps E_g are located around 0.7 eV in the amorphous state and below at around 0.5 eV in the crystalline state [77], due to differences in their atomic structure. Localised electronic states characteristic from the randomly-structured amorphous phase results in a low overlap integral of the neighboring wave functions, with subsequent poor carrier transport which gives rise to the low conductivity state (and lower optical losses at high frequencies). On the other hand, the re-ordering and presence of resonant bondings after crystallisation improves the overlap of such wavefunctions, which turns into an increase of the carrier mobility [77, 137]. For reference, **Table 2.1** shows some of the most relevant compositions that have been successfully employed in optical and electrical non-volatile memories, together with their phase-transition temperatures and corresponding energy

Composition	$T^{\circ}_{cryst}C$	$T^{\circ}_{melt}C$	E_{ga} eV	E_{gc} eV
$Ge_2Sb_2Te_5$	160	610	0.77	0.48
$Ge_1Sb_2Te_4$	160	600	0.76	0.39
$Ag_3In_4Sb_{76}Te_{17}$	200	530	0.68	0.18
GeTe	180	720	0.78	0.55

TABLE 2.1: Some of the most successfully employed chalcogenide PCMs, with their corresponding transition temperatures and energy bandgaps for amorphous and crystalline states [77]

bandgaps [144, 145].

The above described physical properties have made chalcogenide PCMs a suitable platform for the development of non-volatile memory devices. More recently, their potential has been expanded to other fascinating technological fields, such as reconfigurable photonics and metasurfaces or biologically-inspired computing [34, 146]. In the next sections, the most relevant traditional and new applications of PCMs will be briefly discussed.

2.4.2 Applications of phase-change materials: From non-volatile memories to reconfigurable metasurfaces

Today, the use of phase-change materials in non-volatile optical memories such as rewritable CDs and DVDs is well established [33, 143, 147]. In such devices, the high optical contrast between the two PCM metastable phases and the large cycle number of reversible transitions are the key elements to store data optically. Re-writable optical disks consist of a set of thin layers which includes one or more thin PCM films sputtered on pre-grooved substrates. The films surrounding the active PCM layer(s), typically made of thermally insulating oxides (e.g. SiO_2) and thermally conductive metals and oxides (e.g. aluminum, ZnO), have a dual function: first, they provide protection of the PCM against oxidation due to air exposure, and second, they contribute to the realisation of thermally optimised heat sinks for a successful melt/quench (re-amorphisation) process. Optical pulses of visible-wavelength lasers (typically λ = 650 nm and λ = 405 nm) are used to switch the PCM between amorphous and crystalline phases, [33]. As a result of changing the complex refractive index, an abrupt change in the reflectivity of the device takes place between both

phases, allowing for a binary encoding of bits along a surface. Data can be therefore written, read, stored, and erased multiple times thus providing an all-optical, non-volatile memory platform. **Figure 2.15a** shows the cross-sectional diagram of a typical phase-change DVD. Here, two ultrathin $Ge_2Sb_2Te_5$ () layers (10 nm and 7 nm) allow for an enhanced recording capability of 8.5 GB at λ = 660 nm, and a theoretical recording capability of 20.0 GB for λ = 405 nm due to its lower diffraction limit (i.e. lower achievable laser spot size), which results in an enhancement of the recording capabilities over the same DVD disk area [143].

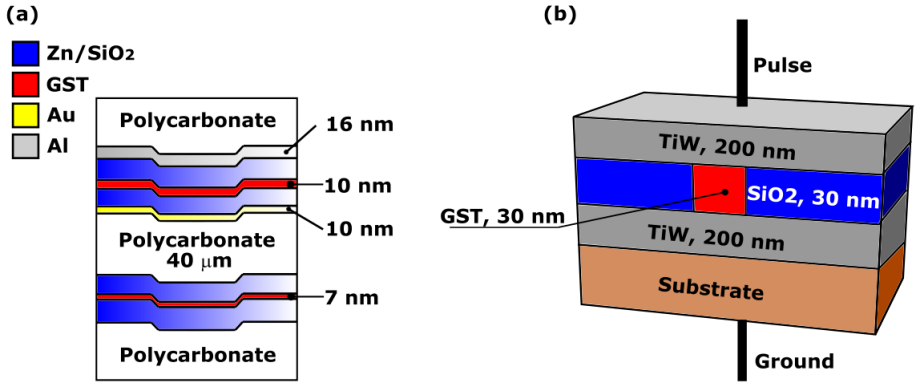

FIGURE 2.15: Non-volatile phase-change memories. **(a)** Cross-section of a dual-layer phase-change re-writable DVD. Re-adapted and reproduced from [143]. **(b)** Picture of a PCRAM structure with the pulse signal delivered to heat and crystallise the PC material. Re-adapted and reproduced from [78].

More recently, PCMs have been exploited towards the creation of electronic non-volatile memories [33, 78, 148]. The key feature here is the high contrast of the electric resistivity between amorphous and crystalline phases. Data can be written and erased via electrically driven heat stimuli of PCM bits in a memory cell. In analogy to optical memories, where the readout is based on a change in reflectance, a change in the resistivity between structural phases allows for modifications in the readout current flow. A typical phase-change random-access memory cell (PCRAM) is shown in **Figure 2.15b** [78]. It consists of a SiO_2 layer with an embedded ultra-thin 30 nm GST bit sandwiched between two TiW electrodes. Electrical pulses can be applied between the two electrodes to induce crystallisation and reamorphisation of the phase-change layer.

Despite phase-change materials having been mainly used in non-volatile optical

and electrical memories, their presence in other technological fields has been growing significantly over the last years. Within the emerging applications, one can now find devices for phase-change neuromorphic computing [149, 150], all-optical phase-change photonic circuits [151], as well as novel photonic devices such as reconfigurable colour generators based on PCM thin films [145, 152], or active phase-change metasurfaces having different functionalities [38, 7, 153, 154].

For example, thin PCM films combined with transparent conductors have been used by P. Hosseini et al. [145] to create reconfigurable colour displays. In this work, platinum mirrors were coated with Fabry-Perot cavity layer stacks consisting of a 7 nm thick GST film sandwiched between two transparent ITO electrodes of different thicknesses. As shown in **Figure 2.16a**, the PCM layer can be switched between amorphous and crystalline phases via Joule heating applying a voltage between the two electrodes. Colour tunability was achieved via changing the GST layer between its structural phases, resulting in a change in the device reflectance and thus colour appearance. **Figure 2.16b** shows the variety of colours obtained, for amorphous and crystalline GST, employing different ITO thicknesses (for a fixed GST thickness of 7 nm). The approach was also successfully demonstrated in transmission mode, and using both rigid and flexible substrates [145].

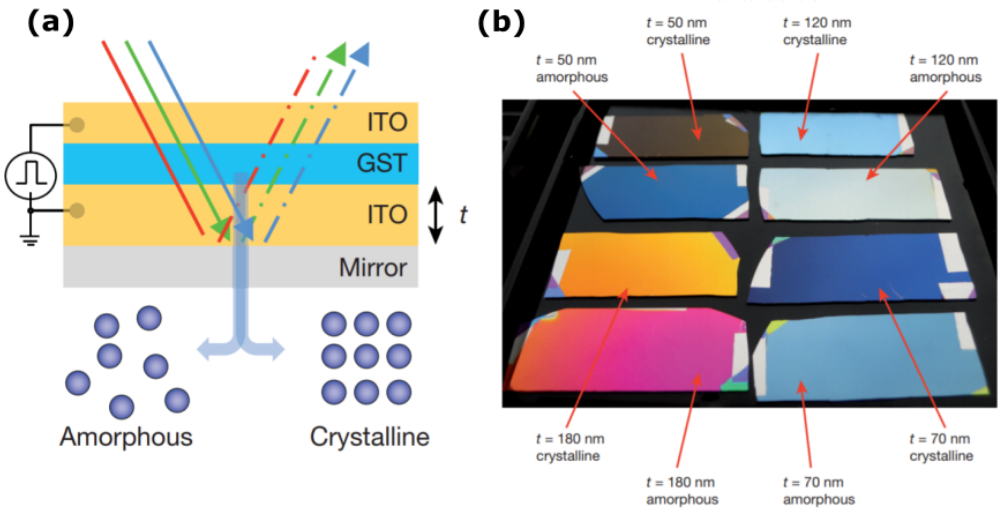

FIGURE 2.16: Phase-change colour displays (reproduced from [145]). **(a)** Cross section of the multilayer stack where a thin GST layer is sandwiched between 2 transparent electrodes (ITO) to produce active colour generation in reflection. **(b)** A photograph showing the variety of colours achievable using different film thicknesses.

Over the last years, the combination of phase-change materials with metasurfaces has been proposed towards novel forms of tunable metasurfaces [153, 154]. The ability of metasurfaces to provide selective control of amplitude, polarisation and phase of light at subwavelength scales, together with the characteristic optical contrast of PCMs has given rise to a wide range of novel compact reconfigurable devices. Some examples include tunable phase-change perfect absorbers in the near/mid infrared and visible spectra [7, 155, 156, 157], tunable negative index metasurfaces [58], phase-change reconfigurable meta-holograms and vortex beam generators [158], or phase-change active beam steering devices in the NIR [38, 159].

One of the first experimental demonstrations of a such concept was reported in 2013 by B. Gholipour et al. [70]. Here, a gold/insulator frequency selective metasurface consisting of Babinet inverted split ring resonators was combined with a multilayer stack including GST as a tunable environment. **Figure 2.17a** shows a detailed diagram of the proposed device. The GST thin film is sandwiched between two ZnS/SiO_2 layers, and located on top of the gold metasurface. When the GST layer is amorphous, the array supports trapped-mode plasmon excitations when the resulting in a peak in reflection at $\lambda = 1550$ nm with a subsequent dip in transmission [70]. After crystallisation, the resonant peak is shifted towards larger wavelengths due to an increase of the refractive index of the phase-change layer. Absolute contrasts of 15% in transmission and 35% in reflection were experimentally confirmed at $\lambda \approx 1310$ nm and $\lambda \approx 1550$ nm respectively (**Figure 2.17b**). Reversible (ex-situ) optical switching between amorphous and crystalline phases was also demonstrated for the first time in phase-change metamaterial based devices.

Work as such as that above, together with similar work based on amplitude control and dating from the same period [64, 160] provided the basic framework of phase-change metasurface technology, which soon stimulated researchers to explore the development of a wide range of phase-change reconfigurable metasurfaces, now commonly known as "phase-change metadevices". Since then, a substantial number of device proposals based on both experimental and numerical demonstrations have been published. Much of them consist of absorbing gap plasmon MIM configurations, where the characteristic dielectric spacer located between two metallic planes consist of a PCM layer (typically GST) providing a tunable dielectric environment

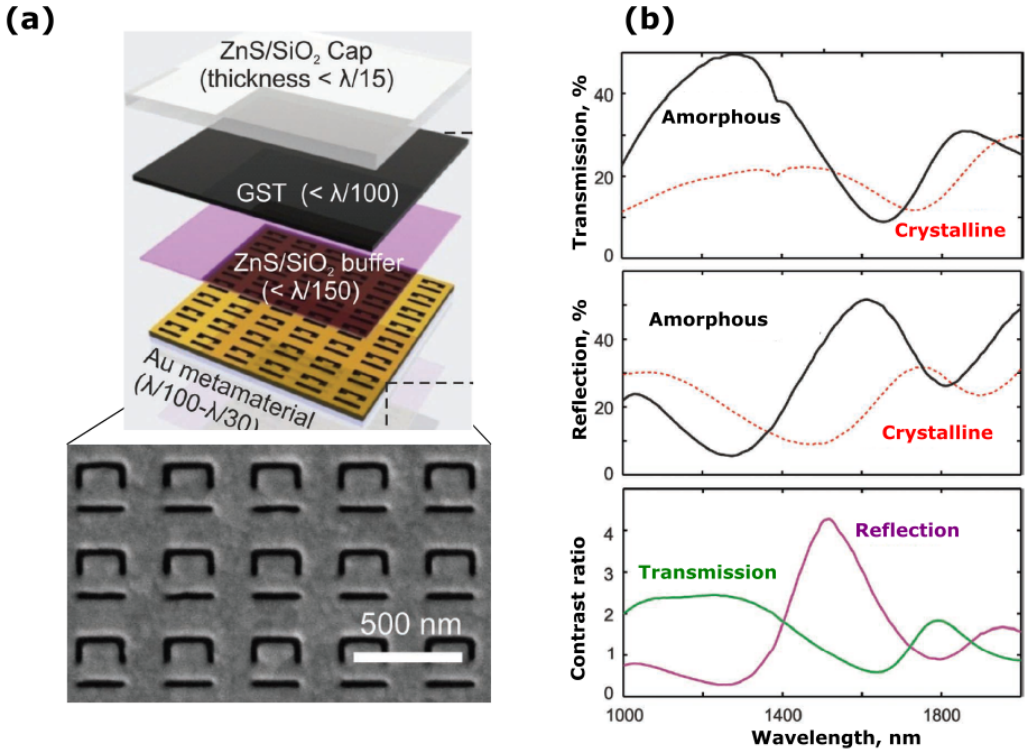

FIGURE 2.17: Plasmonic phase-change meta-switch. Reproduced and re-adapted from [70] **(a)** Schematics of the proposed device (top) and SEM picture of the fabricated structure (bottom) **(b)** From top to bottom: transmission and reflection spectrum for amorphous and crystalline GST, and contrast ratio between phases in reflection and transmission.

[7, 112, 76, 156, 157, 161, 69, 162]. Active control over the phase and polarisation of optical beams employing PCMs is still therefore relatively unexplored, with only a few experimental demonstrations of devices based on phase-control, consisting of dynamic beam steerers (shown in Chapter 4) [38], bifocal lenses [66], and vortex beam generators [158] employing plasmonic metasurfaces combined with GST alloys. Moreover, only a few proofs of reversible optical switching (i.e. crystallisation and re-amorphisation) over various cycles are currently available in the literature [7, 38, 70, 72], and no phase-change active metasurfaces with reversible electrical switching capabilities have been reported so far. Instead, the typical procedure relies on optical characterisation of the as-fabricated devices (in the amorphous phase), with subsequent hot plate crystallisation followed by optical characterisation of the crystalline state [33, 63, 66, 69, 71, 163, 164]. This indeed provides a good proof-of-concept, but also results in one-directional, single-use devices with lack of technological practicability. Such a practice has been repeated for several years since phase-change metasurface technology emerged in 2013 with the work of Gholipour

et al. described above [70]. Research trends in the field seem therefore to be focusing more and more in the conceptual demonstration of new meta-device concepts mostly based on amplitude control, rather than in increasing their practicability and optical functionalities towards their future integration in real applications. That said, the ability of being reversibly switched between amorphous and crystalline states over various cycles while keeping a good optical performance is arguably one of the most important points to start with, and perhaps research efforts should be now re-directed in that way.

The reason why reversible switching of phase-change metasurfaces have been so poorly reported is typically not clarified, but can be attributed to several technological challenges and engineering trade-offs; which have been briefly introduced in **Chapter 1** and are discussed in detail below:

- The first challenge becomes clear by comparing current PCM metasurface device architectures with the well-stablished PCM non-volatile memories, where a minimum of 1×10^{6} switching cycles is guaranteed [33]. In the latter case, small PCM volumes typically not larger than 1.25×10^{-4} μm^3 are embedded in thermally optimised cells or layer stacks to provide effective heat sinks [78, 143]. As a result, the necessary cooling rates (after melting) required for the re-amorphisation to occur ($\sim$ tens of $^{\circ}$C/ns) become accessible. On the other hand, current phase-change optical metasurfaces are based on the use of active PCM volumes sometimes many orders of magnitude larger in comparison with memories [46]. It is therefore straightforward to conclude that the PCM will take longer to cool down to the glass temperature, thus full or partial re-crystallisation of the material after melting might occur, making the re-amorphisation process unaccessible. Reducing the amount of PCM alloy within the metasurface would be therefore beneficial from both thermal and power consumption points of view. However, this might have a direct negative impact over the degree of tunability and/or optical contrast, due to a reduction of the amount of tunable environment. Since meta-atom dimensions scale with the wavelength of operation [6], such thermo/optical trade-off becomes even more challenging when the wavelength increases. In turn, it is

exactly at larger optical wavelengths (NIR and MWIR) where GST based alloys exhibit better optical performance (i.e. major contrast with small dielectric losses), thus where better device efficiencies and tunability ranges can be achieved [34].

- Another (very often ignored) key point for a successful progress of phase-change metasurface technology is the fact of accounting for unwanted chemical reactions and/or incompatibilities. A good example is the phenomenon of thermally induced diffusion of noble metals into PCM alloys, which results in the generation of "parasite" layers at the PCM/metal interfaces ([74, 46, 61, 67, 68]. For example, gold reacts with GeSbTe phase-change alloys to form a AuTe thin layers of up to $\sim$ 5nm between the two interfaces [74]. This is particularly critical, as plasmon excitations occurring in metallic-based optical metasurfaces are extremely sensitive to the permittivities of the dielectric/metal interface [74, 75]. Furthermore, it turns out that metals exhibiting low plasmonic losses in the NIR and MWIR spectra (such as Ag or Au) easily diffuse into chalcogenides [74]. Alternative metals such as TiN, or aluminum Al could be used instead to avoid diffusion; but the former material has severe plasmonic losses at optical frequencies (thus degrades the optical performance) [112], whereas the later melts at temperatures which are only slightly above the melting point of commonly used GST alloys.

- Finally, the last critical point relies on the compromise between the required switching method (i.e. electrically, thermally or optically induced) and the desired final optical performance. For instance, despite the fact that ex-situ optical switching can be suitable for certain applications, ideally pixel by pixel electrically addressed switching is highly desirable to achieve a near real-time active control [145, 165]. On the other hand, certain device functionalities such as active beam steering or lensing would benefit from the use of all-dielectric metasurfaces with no plasmonic losses [88], where electrical switching of individual pixels becomes an extremely challenging task due to the abscence of surrounding good electrically conductive materials.

Overcoming the above-described technological challenges would certainly push phase-change metasurface technology a step closer to become real devices. Therefore, before further development of "in-lab" demonstrations of new exciting (but impractical) devices. Efforts should be focused on practicable phase-change metasurface design and development, taking into account not only the final optical response, but also the important (critical) aspects of thermal, environmental and chemical performance to guarantee both device switchability and endurance.

Chapter 3

Methods

3.1 Finite Element Methods

Finite element analysis (FEA) based on finite element methods (FEM) is a computer-assisted numerical tool which allows for complex physics/engineering problem solving. The areas of application include mechanical, thermal, acoustic or electromagnetic analysis, and indeed any problem based on physical phenomena described by partial differential equations which cannot be analytically solved. The way in which FEM deals with this is via discretisation (subdivision) of a large geometry into simple small parts, named finite elements [166]. Individual equations that arise from each element are re-assembled into a system of linear equations, which is numerically solved to obtain an approximation to the real solution [166].

Due to the need for splitting the geometry under study, FEMs require a very precise and adaptive meshing, which is the process in which the geometry is subdivided and thus distribution and sizes of the constituent elements are defined. To guarantee convergence and accuracy of the obtained solutions, the size and shape of such sub-elements need to be adjusted depending on how much the solution is expected to vary as a function of the space. For example, due to shrinking of the wavelength as a function of the medium refractive index, the electric field distribution of a wave across the propagation direction over a given distance will experience more spatial variations as the refractive index of the medium increases, thus a finer meshing will be required [166]. This might result in memory-intensive, time-consuming simulations, specially in 3D geometries. Nevertheless, FEM offers clear advantages over other numerical methods such as FDTD (finite differences in the time domain), due

to its ability to solve coupled physical phenomena in a single model. That is, solving various partial differential equations simultaneously, and/or employing results from a specific study as an input for for a second one [81]. For example, the power loss density resulting from optical absorption inside a material and calculated via frequency domain electromagnetic simulations can be used to compute the time dependant temperature distribution employing a heat transfer model.

In this thesis, the FEM commercial package COMSOL multiphysics has been employed for realisation of design and analysis tasks. Particularly, electromagnetic FEA models have been used to design the phase-change material based metasurfaces and a heat transfer analysis coupled to the electromagnetic model has been employed to calculate the optically induced heat diffusion of the devices and evaluate the occurrence of a phase transition of chalcogenide PCM alloys.

3.1.1 Electromagnetic model

Computational electromagnetism has a clear goal, which is solving Maxwell's and wave equations in a given region of interest under specific boundary conditions (BC) [81]. FEM allows for electromagnetic problem solving over a wide variety of cases involving different materials (such as metals or dielectrics) and/or excitation conditions (e.g. frequency, polarisation and angle of incidence).

In this work, electromagnetic design and analysis tasks have been carried out employing the *RF* module from the FEM commercial software package COMSOL Multiphysics. Both 3D and 2D models have been employed to solve the Helmholtz equation, where the time component is not present [166]:

$$\nabla \times \Big(\nabla \times \mathbf{E}\Big) - k_0^2\Big(\varepsilon_r - \frac{i\sigma}{\omega\varepsilon_0}\Big)\mathbf{E} = 0 \tag{3.1}$$

where symbols have their usual meanings, i.e. E denotes the electric field, k_0 is the free space wave vector, ε_r is the relative permittivity of the medium, σ is the electrical conductivity of the medium, ω is the angular frequency of the excitation beam and ε_0 is the vacuum permittivity. Results are displayed as a scattering matrix, which contains the frequency dependent amplitude and phase of the reflected, transmitted, and diffracted waves (i.e. modulus and argument of the S parameters). Particularly,

electromagnetic FEA models have been used to design and analyse the optical response of the phase-change material based metasurfaces developed in **Chapters 4**, **5** and **6**.

Two-dimensional analyses were employed for geometries with translational symmetry, such as thin films or one-dimensional metasurface arrays like the ones discussed in **Chapter 4**. In such models, an adaptive meshing with triangular elements was employed. The maximum element sizes were defined as a function of the domain material. For metals, the maximum allowed size was determined by the skin depth δ at the frequency of interest [81], that is:

$$\delta = \sqrt{\frac{2\rho}{\omega}} \tag{3.2}$$

where ρ is the resistivity In the case of dielectrics, the largest element was set as $\lambda_0/50n$, where λ_0 is the free-space excitation wavelength, and n is the real part of the material refractive index. **Figure 3.1a** shows a 2D meshing example, here specifically of a one-dimensional plasmonic antenna in a metal-insulator-metal configuration such as the devices shown in **Chapter 4**.

The boundary conditions employed in the 2D electromagnetic models are summarised in **Figure 3.1b**, and listed below:

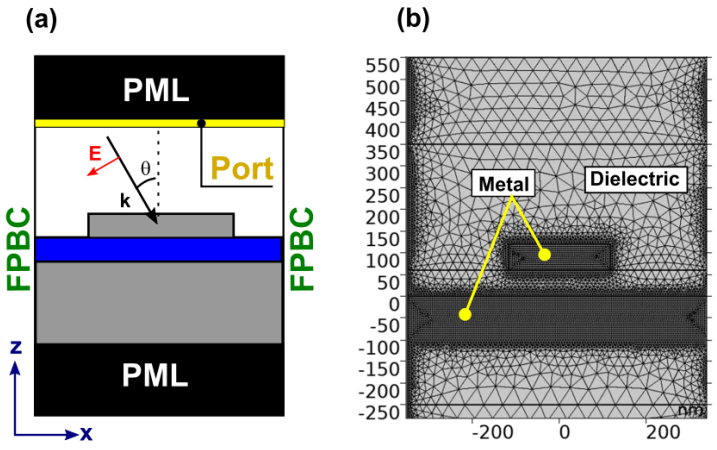

FIGURE 3.1: **(a)** Mesh of a 2D electromagnetic model based on triangular elements. **(b)** Schematics summarising the boundary conditions employed in 2D electromagnetic models. Spatial coordinates are given in nm.

- Floquet periodic boundary conditions (FPBC) were applied on the lateral limits of the cell in order to mimic an infinite array of elements.

- A periodic port is located at the top boundary, in order to excite the structure under the required conditions in terms of frequency, polarisation, power, and angle of incidence.
- Perfectly matched layers (i.e. artificial absorbing layers) were placed at the top and bottom to avoid reflections from the boundaries and thus truncate the computational region [166].

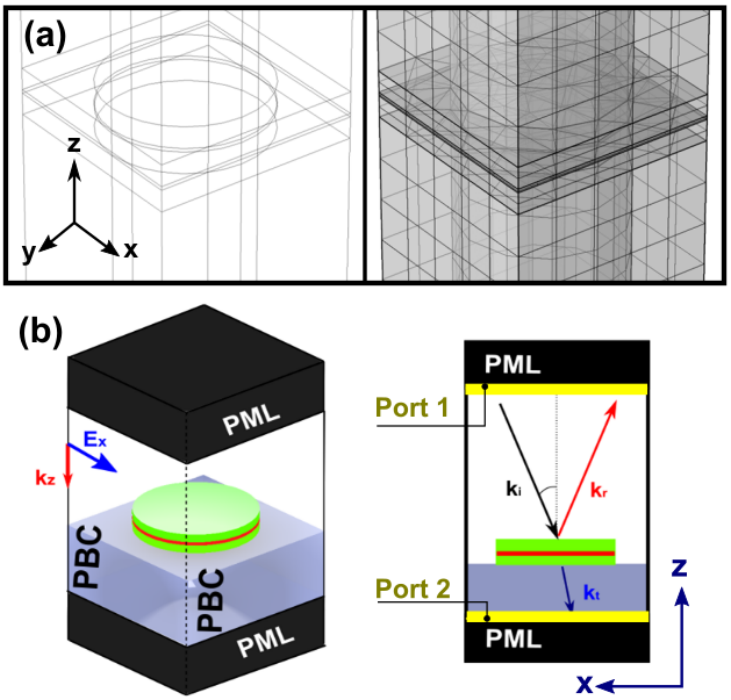

FIGURE 3.2: **(a)** Mesh of a 2D electromagnetic model based on triangular elements. **(b)** Schematics summarising the boundary conditions employed in 2D electromagnetic models.

Geometries with no translational symmetry were analised employing 3D modelling, and thus slightly different meshing and BCs definitions. Meshing of three-dimensional models were made with triangular elements in the x and y axes, under the same conditions described above in terms of maximum allowable element sizes. Mesh resolution in the z direction was set by projecting elements from the x and y along the different material layers. **Figure 3.2a** shows the 3D meshing employed for hybrid all-dielectric PCM/silicon nano-cylinders discussed in-depth in **Chapter 5**. Here, the boundary conditions are essentially the same as for 2D structures described previously, with the only difference of FPBC placed in both x and y axes to simulate two-dimensional arrays.

Property	Amorphous GST	Crystalline GST
C_p [J/kg.K]	220	260
k_t [W/m.K]	0.19	0.58
ϱ [kg/m^3]	5870	6270

TABLE 3.1: Thermal properties of amorphous and crystalline GST at room temperature, taken from [167, 168, 169]

3.1.2 Thermal model

The switching mechanism of a phase change material requires for electrical or optical heat stimuli in the form of pulses having different durations. During a pulse, the way in which heat flows through the neighbouring media is governed by the heat equation (eq. 3.3, which can be solved in COMSOL employing the *heat transfer in solids* module:

$$\varrho C_p \frac{\partial T}{\partial t} - k_t \nabla^2 T = Q \tag{3.3}$$

where ϱ, C_p and k_t are the temperature dependant density, heat capacity and thermal conductivity of the medium respectively. Q is the volumetric heat source; and T and t have their usual meanings (i.e. temperature and time). When the heat stimulus ceases, a cooldown process as a function of time takes place. As it can bee seen from eq. 3.3, both heating and cooling mechanisms are strongly dependant on the thermal properties of the surrounding materials. The temperature dependant thermal properties and density of $Ge_2Sb_2Te_5$ employed in our simulations have been taken from refs. [167, 168, 169]. Values at room temperature are shown in **Table 3.1** for a quick reference.

As described in the previous chapter, the rate at which commonly employed chalcogenide PCMs (such as GST) reach their glass temperature ($T_g < 200^\circ C$) after melting ($\approx 600^\circ C$) is a critical parameter for a successful re-amorphisation process, and thus a key design parameter which might be challenging due to thermal insulation as a result of the low thermal conductivities shown in **Table3.1**. On the other hand, since crystallisation temperatures are relatively low ($T_c \approx 130^\circ C$), special attention should be given to the amount of optical power that the device can hold at the design wavelength without heating above this point. In this context, thermal modeling has been therefore carried out in this project for the following purposes:

- To estimate the power handling capabilities of the fabricated PCM metasurfaces. That is, how much power per unit of area can be irradiated on the device without optically crystallizing it.
- To verify that the cooling rates of the phase change layer are fast enough for a successful re-amorphisation (tens of celcius per nanoseconds in [33] and estimations of at least $\approx 20°C/ns$ in [170]).
- To estimate the experimental laser fluences required for the switching experiments.
- To ensure no melting of the surrounding materials.

i. Optically induced heat transfer

Light absorption in lossy materials becomes a source of heat which can be controlled via external laser pumping with different amplitudes and durations. Simulations of optically induced heating of the phase-change metasurfaces developed herein were therefore carried out employing the electromagnetic models described in the previous section, coupled to the *heat transfer in solids* module.

Figure 3.3 shows a simple case scenario of such simulations, where the influence of different substrates on the heating and cooling rates of a 50 nm thick GST film was evaluated. First, the the structure is excited (here with a wavelength λ = 1550 nm) employing the electromagnetic model in order to solve the power density loss (W/m^3) within the film. The resulting power loss map (**Figure 3.3a**) is then used as a volumetric heat source Q to calculate the time-dependant temperature distribution during a given pulse, as shown in **Figure 3.3b**. The cooling rates can be finally calculated when the pulse terminates, as shown in **Figures 3.3c-d**.

For a SiO_2 substrate, a laser fluence of ≈ 250 pJ/μm^2 was calculated to melt the GST layer (i.e. to increase its temperature above $T_m = 600°C$) as shown in **Figure 3.3c**. However, it can bee seen from the same plot that the glass temperature ($T_g < 200°C$) cannot be reached in 15 ns (to guarantee cooling rates above $20°C/ns$ as estimated in [170]. This can be explained by the low thermal conductivity of SiO_2 (1.4 W/mK at room temperature according to the manufacturer specifications),

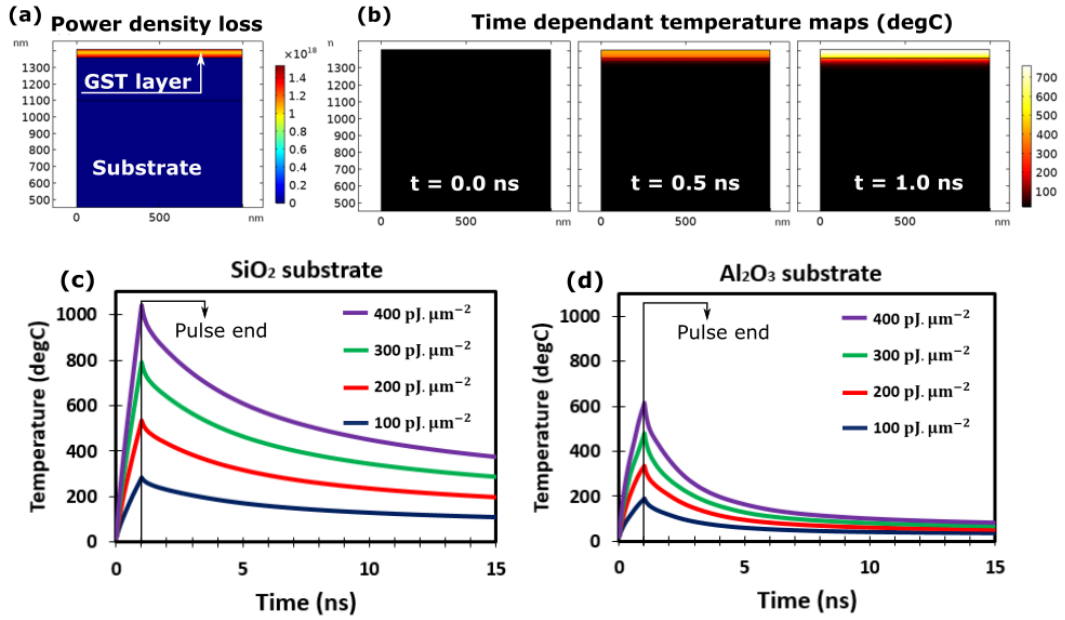

FIGURE 3.3: **(a)** Power density loss map calculated for a 50 nm thick crystalline GST film on top of a SiO_2 substrate. The excitation wavelength was 1050 nm (pulse 1 ns), and the fluence 200 $pJ/\mu m^2$. It can be seen how losses are concentrated in the GST layer, since SiO_2 exhibits no optical absorption at λ = 1050 nm **(b)** Evolution of the map temperature during the pulse. **(c-d)** Heating and cooling rates calcualted for different laser fluences, employing 2 different substrates: **(c)** SiO_2, **(d)** Sapphire.

which acts as a heat barrier that slows down the cooling rates, thus preventing a successful re-amorphisation under this excitation conditions.

Same calculations employing a sapphire substrate are displayed in **Figure 3.3d**. Here, the layer cools down to the glass temperature in 15 ns, thus re-amorphisation becomes possible due to the thermal conductivity of sapphire being nearly 20 times higher than SiO_2 ($\approx$ 28.0 W/mK at room temperature, again based on manufacturer specifications). The sapphire substrate acts therefore as a very efficient heat sink to speed up the cooling rates, but in contrast, higher fluences of $\approx$ 400 $pJ/\mu m^2$ are required to achieve the melting temperature since the heat is not easily retained inside the GST layer.

ii. Resistive heat transfer

As an alternative to optically-induced heating, resistive Joule heating can be also utilised to induce the phase transition in PCM-based devices [37]. In this approach, the passage of an electric current through a micro-heater is employed as a volumetric source of heat generated by Ohmic losses. **Figure 3.4** shows a case scenario

of such simulations, where a pixelated microheater was used to study the electrical switchability of the devices shown in **Chapter 6**, which consist of hybrid silicon/GST antennas in the form of nanocubes (**Figure 3.4a**). As shown in **Figure 3.4b**, here an Au/SiO_2 strip placed underneath the antennas was employed to study both the temperature distribution and heating/cooling rates at different currents (detailed analysis of such calculations will be presented in the relevant chapter).

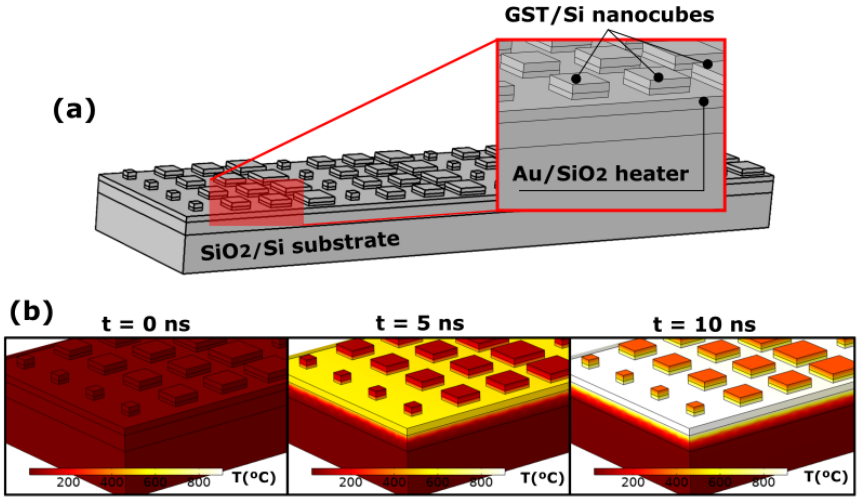

FIGURE 3.4: **(a)** Pixelated micro-heater for the electrical switching of devices shown in **Chapter 6** (b) Example of the evolution of the temperature map as a function of time during an electrical pulse

iii. Boundary conditions

Thermal insulation boundary conditions were applied to all the air/material interfaces, since fluid convection heat flow can be neglected at the nanosecond timescales. At the bottom interface, The model was truncated via fixing the temperature to 20 °C in the lower boundary of the substrate.

3.2 Nano-fabrication methods

Fabrication of optical metasurfaces requires accurate deposition of continuous thin films of different materials, with subsequent high resolution patterning via lithography combined or not with reactive ion etching. This section is meant to describe the working principle and fabrication procedures of the various methods employed

during the development of this thesis. Specific details about individual device fabrication will be discussed in the relevant experimental chapters.

3.2.1 Thin film deposition via magnetron sputtering

In magnetron sputtering, the surface of a target material is bombarded with noble gas ions (usually argon), which results in a momentum transfer that ejects atoms from the target [171]. The process starts by injecting argon (Ar) into a vacuum chamber at a low base pressure (usually in between 1×10^{-8} and 1×10^{-6} mbar) where a plasma is then generated after applying a DC or RF potential between two parallel electrodes. As shown in **Figure 3.5**, the atoms detached from the target material "travel" towards the substrate forming a thin film due to the voltage applied between the cathode (target) and the anode (substrate). This technique can be used to fabricate thin films of a wide variety of materials (from insulators to metals), thus has been chosen for the elaboration of thin films and devices developed during this thesis. The main advantages of sputtering techniques over other methods are mainly due to high kinetic energy of ejected atoms, which results in better substrate adhesion and high uniformity films (in terms of thickness, roughness and density) over large surface areas [172].

Due to the relatively large variety of materials employed in this work, as well as the need for certain layer stacks to be sputtered in a single sputtering session (e.g. thin films of phase-change materials need to be capped when in vacuum to avoid oxidation), three different magnetron sputtering systems have been used (Moorfield Nano-PVD, Nordiko 2000 and a custom-built magnetron sputtering machine). The film quality, sputtering yield and deposition rate of each material strictly depend of a series of factors listed below:

- Sputtering conditions: Power, base pressure, argon flow, and argon pressure.
- Machine characteristics: target geometry, target-to-substrate distance and target orientation relative to the substrate.
- Material properties: binding energy and atomic mass of the target material.

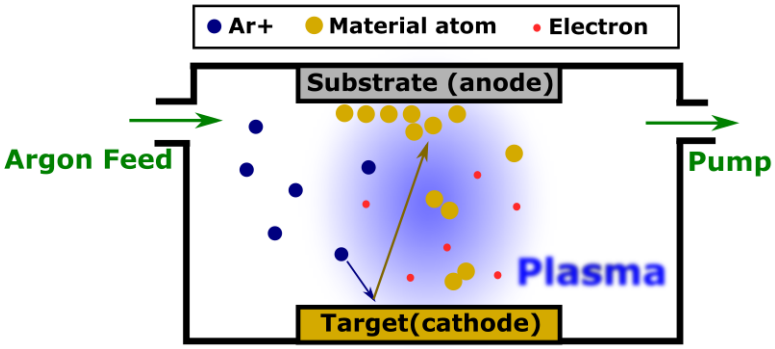

FIGURE 3.5: Diagram of a typical magnetron sputtering system. argon ions are accelerated towards the cathodic target, resulting in ejection of atoms and their subsequent deposition onto a substrate (anode).

Therefore, optimisation of the above parameters are required to obtain homogeneous good quality films [173] (details about the sputtering parameters for each material will be given in the relevant experimental chapters). In addition, in order to maintain accuracy, consistency and repeatability of the deposition processes; the sputtering conditions were always kept the same, and the deposition rates of each material was recalculated periodically to ensure accuracy of the film thicknesses. An example of a deposition rate calibration is shown in **Figure 3.6**. Here, three different layers of amorphous silicon were sputtered over different times (10, 20 and 30 min) under the same conditions. The thicknesses of each layer were measured employing contact atomic force microscopy (described in **section 3.4.3**), and a linear regression was then carried out to obtain the deposition rate in nm/min.

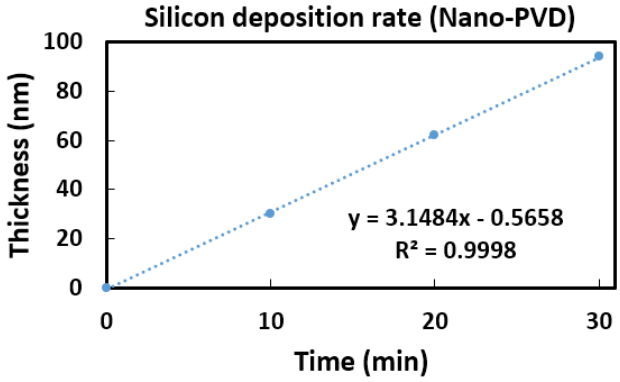

FIGURE 3.6: Calibration of the silicon deposition rates employing the Moorfield Nano-PVD sputtering system

3.2.2 Nano-patterning via electron beam lithography

Fabrication of optical metasurfaces requires for accurate lithography processes, as the sizes of their constituent meta-atoms are subwavelength in nature. When the design wavelength shrinks, the required spatial resolution falls beyond the capabilities of conventional optical lithography, which is fundamentally limited by light diffraction. Electron beam lithography (EBL) is currently the most employed technique for the fabrication of meta-devices below the mid-wave infrared (MWIR), where the required sizes and/or gaps between elements are in the order of tens to hundreds of nanometers [174]. In this thesis, therefore, EBL has been used to transfer the desired patterns onto the substrates for the realisation of the devices discussed in Chapters **4**, **5** and **6**.

In a typical EBL process, an electron beam is highly focused onto a electron-sensitive resist following a pre-designed pattern. Electron exposure produces a change in the resist molecular structure and solubility, and thus a sacrificial mask can be then generated via subsequent development of the resist employing a suitable solvent or developer. Therefore, the key determinants for a good quality pattern are the choice of resist, developer, process conditions (i.e. electron beam current and dose) and development time and temperature [175] as discussed below:

- **Resist selection and spin coating.**

  The first step in a EBL process consists of depositing a layer of resist onto a substrate via spin coating, followed by annealing of the sample to harden the resist. As a rule of thumb, the resist thickness has to be typically around 3 times thicker than the thickness of the desired pattern, however this can/might need to be modified depending on the process complexity [176].

  Two main types of resist can be selected at this step: positive and negative resists. As shown in **Figure 3.7a**, exposure to electrons causes rupture of bonds in positive resists, making them more soluble. A solvent or developer is then used to wash away the weakened resist, which results in a positive mask. Positive masks are typically used for the fabrication of low aspect ratio nano-patterns, where sputtering inside the clear regions followed up by a lift off process in a solvent results in the desired structure [175].

On the other hand, negative resists experience cross-linking after electron exposure and become less soluble. As shown in **Figure 3.7b**, after development only the cross linked regions which have been exposed to electrons remain intact, resulting in a negative mask. A reactive ion etching process is then carried out to remove the unprotected regions and obtain the desired nano-pattern. Negative resist masks are typically used for the realisation of high aspect ratio structures, where magnetron sputtering inside a mask fails [175].

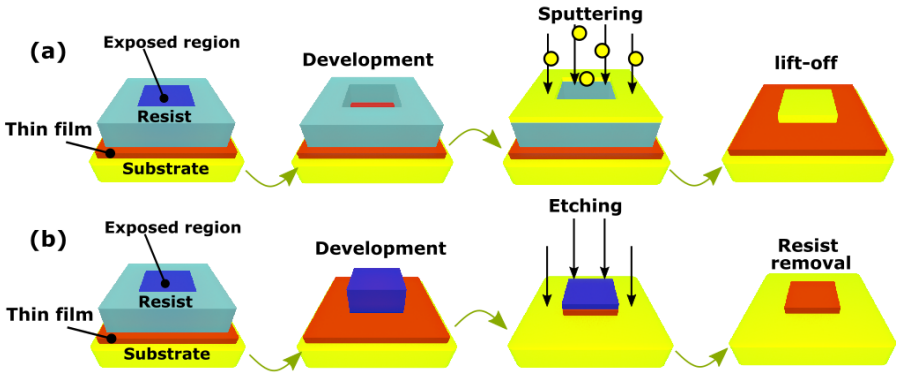

FIGURE 3.7: Electron beam lithography steps employing: **(a)** a positive resist followed by a magnetron sputtering process to fill the gaps. **(b)** A negative photoresist followed by reactive ion etching.

- **Electron exposure**

  After spin coating with an appropriate resist, the sample is introduced inside the EBL system (in this thesis, a NanoBeam NB4). The chamber is then pumped down to pressures below 2×10^{-7} mbar before starting the writing process. As shown in **Figure 3.8**, the electron exposure system consists of an electron gun, a condenser/focusing set of magnetic lenses, a beam blanker to switch the beam on and off, and a deflection system which allows the beam to be moved [176]. The beam is focused onto the resist and scanned across the sample to transfer a pre-designed pattern.

  The quality and sizes of the resulting mask will strictly depend on the resist employed, electron acceleration voltages, current and exposure dose utilised during the process. Due to charging effects, low beam currents are typically used to achieve small sizes and high resolution patterns [177]. The exposure dose D_s can be also optimised to modify the size of the final nano-pattern:

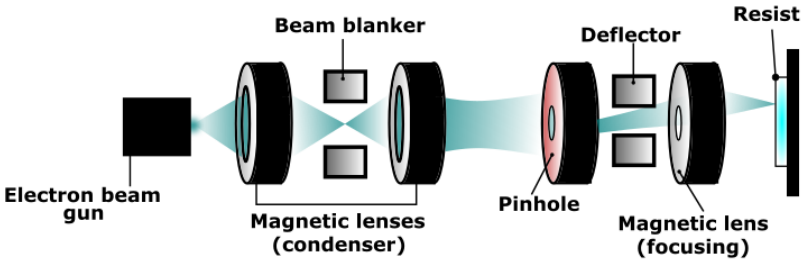

FIGURE 3.8: Schematic of a typical EBL writing system

$$D_s = \frac{It}{A} \tag{3.4}$$

where I is the current, t is the exposure time and A is the exposed area. Particularly in this thesis, low currents (below 2 nA) were employed to ensure high pattern resolution, and dose tests followed by morphological characterisation were carried out to determine the optimum lithography parameters of the metasurfaces discussed in Chapters **4**, **5** and **6**.

- **Resist development**

  As described previously in this section, after being exposed to electrons the resist undergoes either cross linking or rupture of bonds, which modifies its solubility depending on its nature (negative or positive). A solvent is then employed to remove the unwanted resist areas.

3.2.3 Reactive ion etching

Etching processes can be carried out either in a wet or dry atmosphere. In wet etching techniques, the use of liquid etchants induces chemical reactions which allow the removal of material that is not protected by the resist mask. On the other hand, in a dry etching process (also known as reactive ion etching, or RIE) the material removal is driven by a combination highly and/or low reactive gases in a plasma environment, which involves both chemical and physical processes [178]. Selective reactive ion etching (Moorfield nano-etch) was employed in this thesis after a negative-resist EBL process in order to remove spare material and achieve the required nano-pattern.

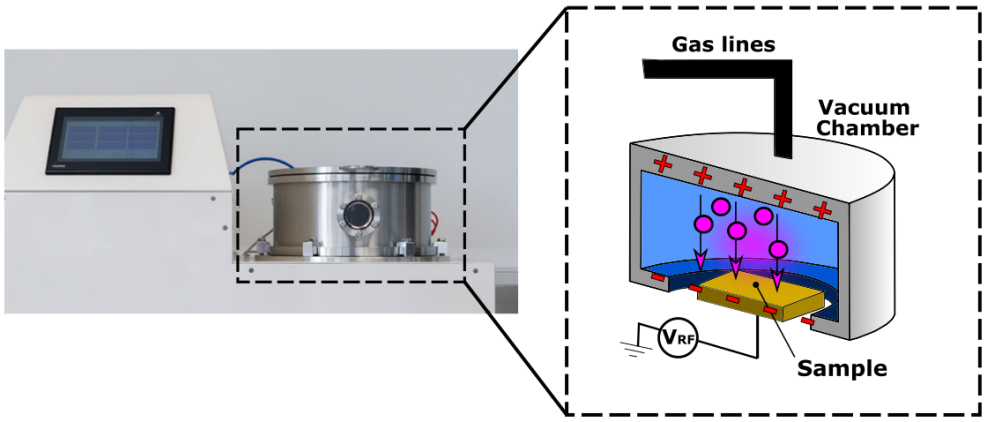

FIGURE 3.9: Schematics describing the working principle of a reactive ion etching process

The working principle of RIE is somwhat analogous to magnetron sputtering, since the process involves the use of ionised gases in a low pressure plasma environment. Gas ions are accelerated towards the sample (previously protected with a resist mask) in order to remove material from the unwanted areas via both mechanical (particle momentum exchange) and chemical (reactive) processes [178].

As depicted in **Figure 3.7**, RF power is applied to the chamber cathode, which results in an electric field towards the (grounded) anode that ionises the gas and creates a plasma. Generation of accelerated reactive ions allows for a selective material removal. As in a sputtering process, each material to etch requires specific conditions that need to be optimised for a successful process. This can be achieved via adjustment of etching conditions listed below:

- Gas composition and flow. For example, highly reactive Halogen-based combinations of gases with different flow rates (SF_6/O_2, CF_4/O_2...) are typically used for the etching of dielectrics and semiconductors like SiO_2, Si, or SiN [179].
- Etching parameters such as RF power, base pressure and gas pressure.
- Plasma induction characteristics, such as density, directionality and ionisation efficiency, which can be adjusted via capacitive or inductive plasma generation.

A successful process should ideally give highly selective and anisotropic profiles, as well as low roughness profiles [179], which can be checked via morphological

characterisation techniques such as atomic force microscopy (described in section **3.4.3**) or scanning electron microscopy (section **3.4.4**).

3.3 Characterisation methods

The optical, morphological and compositional characteristics of the samples and devices developed during this thesis were measured employing a variety of experimental techniques. Therefore, this section aims to give a brief description of the working principles of the experimental setups utilised, as well as to describe the measurement steps and any post-processing and/or consideration required for a correct interpretation of the raw data.

3.3.1 Optical micro-spectroscopy

Optical spectroscopy is a globally employed characterisation technique which allows the quantification of emission, reflection, transmission and absorption spectra of light by matter [180]. Its working principle consists of measuring the wavelength dependant amplitude carried by a beam which has previously interacted with a specimen. Particularly, the term micro-spectroscopy refers to measurements carried out over microscopically sized areas employing a focused beam of polychromatic light.

In this thesis, visible and near-infrared microscpectroscopy measurements were employed to obtain reflectance measurements of thin films and metasurfaces developed during this thesis, as well as to provide a complementary method to X-ray diffraction for checking the structural phase transition of PCM films after annealing processes (i.e. via changes in the reflectance spectra). In addition, microspectroscopy has been used in this thesis as an intermediate quality control between fabrication steps, for example, to check the reflectance spectrum of a specific device layer stack before proceeding with an e-beam lithography process.

Figure 3.10 shows a schematic of the instrument utilised for the above (JASCO MSV-5300, spectral range λ = 200 nm to λ = 1600 nm). It consists of a microscope

with a deuterium-halogen based illumination system linked to a spectrometer (maximum spectral resolution $\Delta\lambda$ = 0.2nm). A collimated beam is focused onto the sample under test. The beam is then reflected by the specimen, re-collected by the objective and re-imaged onto the slit of a spectrometer, which acts as a field stop. The sample image is then re-collimated using an off axis parabolic mirror, and re-directed to a blazed grating which splits the polychromatic beam into different monochromatic channels. Spectrally separated beams are finally focused onto a cooled InGaAs detector which measures the signal associated to each wavelength.

Three different focusing objectives with different numerical apertures (NA) can be used for the measurements ($\times$10 - NA 0.20, $\times$20 - NA 0.25 and $\times$32 - NA 0.50). The employed numerical aperture determines the amount of signal that reaches the detector, as well as both the range of incident and collection angles via the following relation:

$$NA = sin(\beta) \tag{3.5}$$

where β is the maximum semi-angle of the light cone that can be collected by the objective. Thus, lower NA objectives are better suited for the measurement of samples which exhibit strong angular dependence of the reflectance spectrum (at the cost of a lower signal to noise ratio and resolution).

Absolute reflectance measurements $Rs(\lambda)$ can be obtained via normalizing the signal reflected by the specimen to the signal from a reference surface of known reflectance R_m (here specifically, a protected aluminum mirror previously calibrated by Optical Reference Laboratory LLC, as shown in **Figure 3.11a**)[180]:

$$R_s(\lambda) = \frac{I_s(\lambda)}{I_m(\lambda)} R_m(\lambda) \tag{3.6}$$

where I_s and I_m are the raw signals (in counts) collected from the specimen and the reference mirror respectively. For example, **Figure 3.11b-d** shows the above described normalisation process of a typical aluminum/GST/ITO Fabry-Pérot (FP) cavity depicted in **Figure 3.11b**. First, the wavelength-dependent raw signals from the calibrated mirror, amorphous and crystalline samples are measured (**Figure 3.11c**).

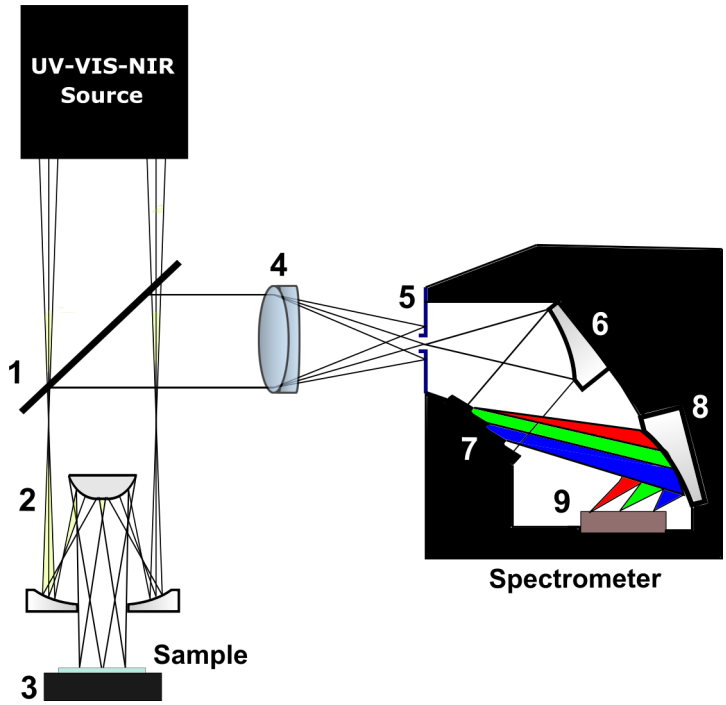

FIGURE 3.10: Diagram of JASCO MSV-5300 microspectrometer and its main components: **(1)** beam splitter, **(2)** x32 cassegrain objective, **(3)** sample holder, **(4)** focusing lens, **(5)** field stop aperture, **(6)** collimating mirror, **(7)** blazed grating, **(8)** focusing mirror, **(9)** InGaAs detector.

The absolute reflectance spectra for amorphous and crystalline GST can be then calculated via eq. 3.2, as shown in **Figure 3.11d**.

3.3.2 Fourier imaging near-infrared micro-spectroscopy

In a conventional micro-spectrometer operating in reflection, an objective lens is used both to focus and to collect light emerging from a specimen. The beam is then re-directed and focused onto a (real) image plane where spectral information is measured employing a spectrometer as described in the previous section. In other words, the measurement plane coincides with the image plane of the sample, thus the analysed signal is a weighted sum of different plane wave components emerging from the specimen at different angles [181]. In the case of Fourier imaging spectroscopy, measurements are performed in the back focal plane of a microscope objective, where such plane wave angular components are separated. Additional information about both spectral and angular characteristics of the sample can be therefore obtained employing this method.

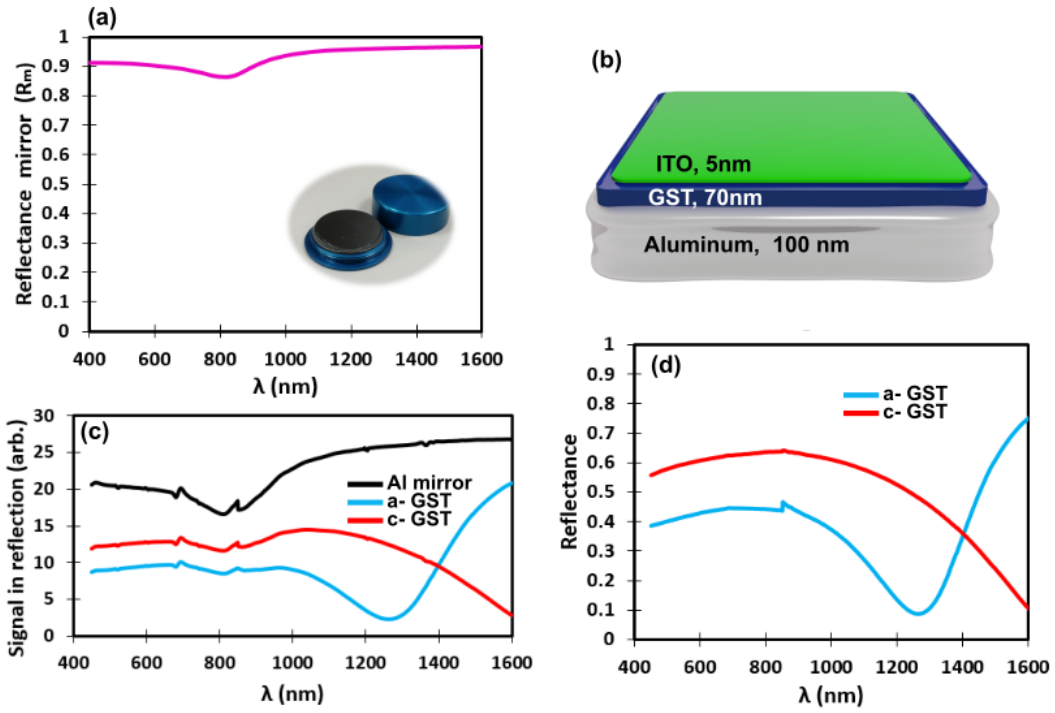

FIGURE 3.11: **(a)** Reflectance spectrum of the calibrated aluminum reference surface (shown in the inset). **(b)** GST-based Fabry-Pérot cavity. **(c)** Measured raw signal from the aluminum reference surface, amorphous, and crystalline GST-based FP cavity. **(d)** Calculated absolute reflectance spectra for amorphous and crystalline GST.

To summarise this concept, let's consider a sample located in the rear focal plane (RFP) $h(x,y)$ of a convergent lens as shown in **Figure 3.12**. When light emerging from the sample at different angles passes through the lens, each of the plane waves components is focused onto a a different point at the back focal plane $H(x,y)$. Information about the outgoing angles $(\theta_{xi}, \theta_{yi})$ is therefore encoded as spatial coordinates, which conceptually and mathematically corresponds to a Fourier transformation [182]. Therefore, performing spectroscopic measurements in the back focal plane of a lens allows the mapping of both angular and spectral characteristics of a specimen at the microscopic scale, something that cannot be achieved with traditional micro-spectroscopy. This technique has therefore emerged as an important characterisation tool in research fields like nanophotonics, and has been successfully employed in measuring radiation patterns of e.g., optical reflectarray antennas [11, 38] single quantum emitters [183, 184] or non-linear scattering [185].

Particularly in this thesis, Fourier imaging spectroscopy (operating in reflection) has been employed to characterise the radiation patterns of the fabricated plasmonic

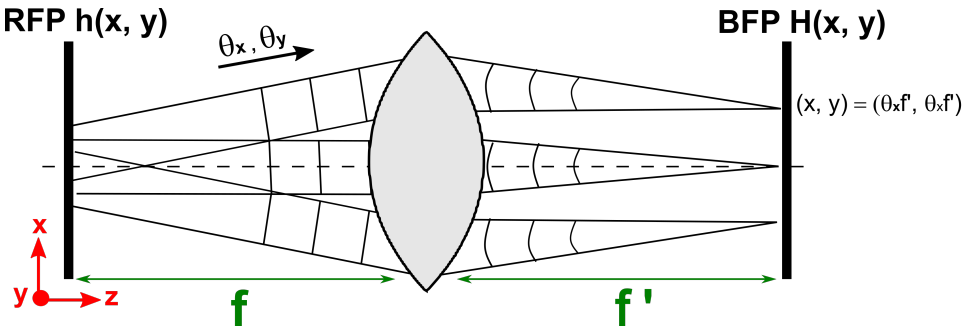

FIGURE 3.12: Schematics showing the concept of a Fourier transform employing a convergent lens.

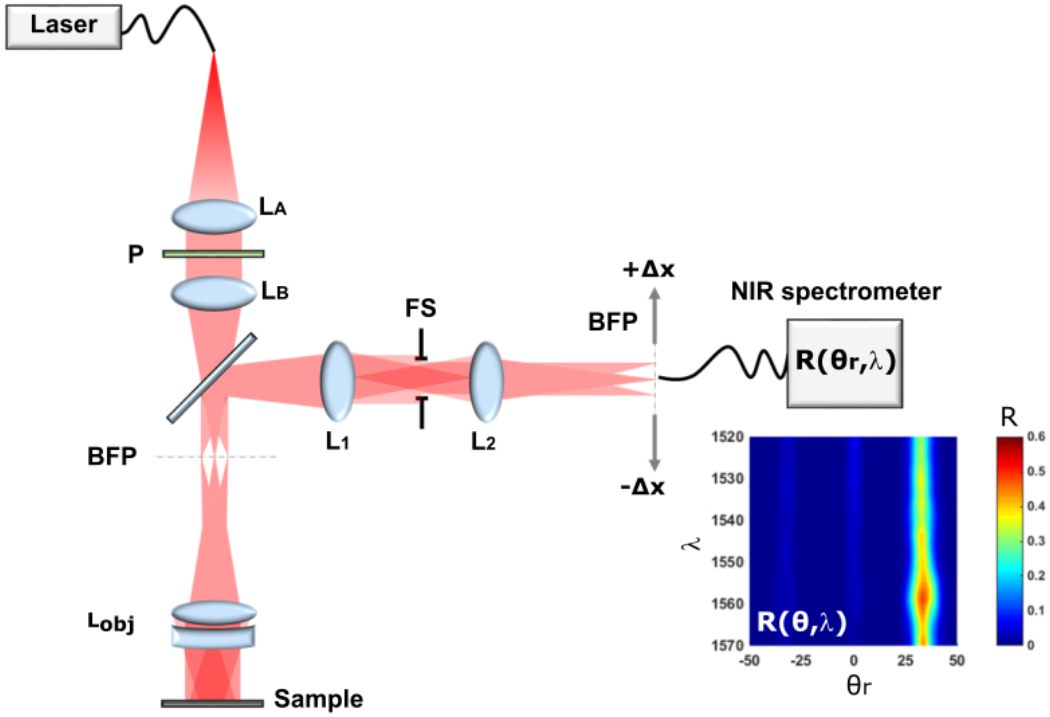

FIGURE 3.13: Fourier imaging micro-spectroscopy setup, located at the University of Bristol.

phase-change beam steering devices (**Chapter 4**), as well as the band diagram of the all-dielectric hybrid phase-change metasurfaces shown in **Chapter 5**. A detailed diagram of the setup employed within the development of this work is depicted in **Figure 3.13**. It consists of a microscope operating under a Kohler illumination system which collimates light from the source into the sample via a set of lenses (L_A, L_B and L_{OBJ}), ensuring uniform illumination and normal incidence ($\theta_i = 0$). A polariser P is located within the illumination system to control the polarisation of light. The setup is fed by a supercontinuum laser source (NKT Photonics superK COMPACT, spectral range λ = 400 nm to λ = 2200 nm) with a total output power of

110 mW. The radiation pattern of the sample under test is imaged into the back focal plane of the microscope objective lens L_{OBJ} as described previously in this section. The BFP is then re-collimated by L_1, and re-imaged by L_2. Then, an optical fiber connected to a NIR spectrometer scans the BFP plane in discrete steps of 20 μm , allowing measurements of the reflectance spectrum of the sample as a function of the fibre position, which encodes the angular coordinates of the radiation pattern as described in **Figure 3.12**. The relation between the axial position of the fiber Δ_x and outgoing angle of reflection θ_r is calculated through the Abbe sine condition,

$$sin(\theta_r) = \frac{\Delta_x f_1'}{f_2' f_{obj}'} \tag{3.7}$$

where f_1' and f_2' are the focal lengths of L_1 and L_2 respectively (f_1' = f_2' = 300 mm), and f_{OBJ}' = 2.6 mm is the focal length of the microscope objective. Accuracy of calculations employing Abbe sine condition were validated by measuring a commercial grating of known period (and thus known angular position of the diffraction orders).

3.3.3 Surface characterisation: Atomic force microscopy

Atomic force microscopy (AFM) is an optomechanical characterisation technique capable of detecting forces in the order of nanonewtons, as well as characterising geometrical details down to the Angstrom scale [186]. Within its various applications, AFM is mainly employed for morphological (e.g. topography) characterisation of samples at the nano and micro scale. Particularly in this thesis, an atomic force microscope (model Bruker Innova AFM) operating in contact mode was used to characterise the dimensions and morphology of the realised devices, and thus to validate the fabrication processes. This technique has been also used to calibrate the sputtering deposition rates as described in **section 3.1**, via measuring the thicknesses of the as-deposited thin films.

The working principle of a typical atomic force microscope operating in contact mode is summarised in **Figure 3.14a**. It consists of a tip integrated at the end of a spring cantilever. When the instrument operates in contact mode, the tip touches the surface and moves across the x and y directions, resulting in height variations

(z direction) induced by the sample relief. A laser source is projected onto the cantilever, and reflected towards a quadrant detector which allows a topography map to be obtained via calculation of the sample height for each (x, y) coordinate. **Figure 3.14b** shows a typical micro scale topograpic map obtained via AFM measurements in contact mode (here specifically, an array of hybrid silicon GST nano-cylinders).

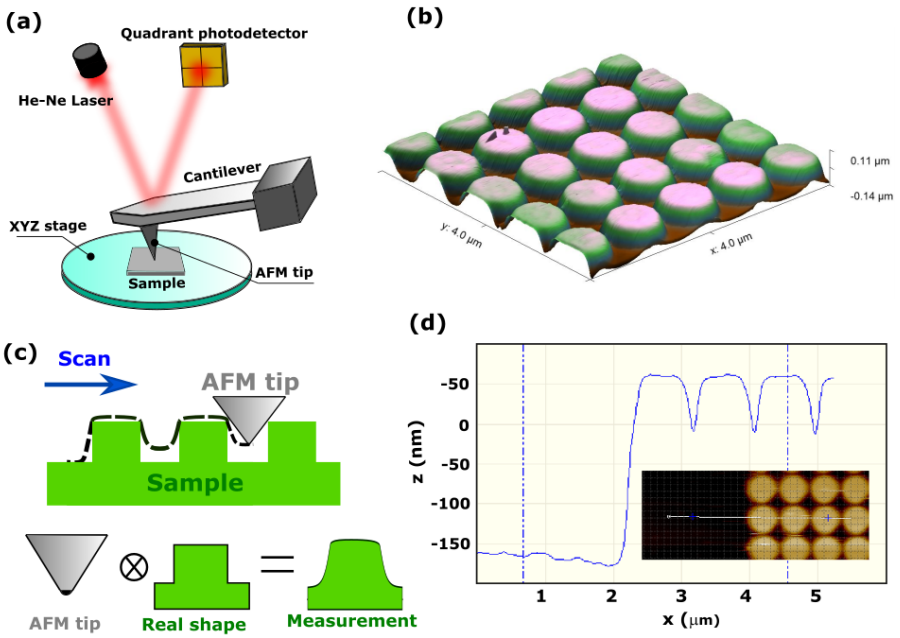

FIGURE 3.14: Atomic force microscopy. **(a)** Shcmematics of the operating principle, where a laser source. **(b)** Topography of an array of nano cylinders the measured via AFM in contact-mode. **(c)** Diagram showing tip convolution effects in periodic structures, where spatial information might be lost due to the tip size. **(d)** 2D cross section of the same array as in (b), showing loss of spatial resolution within gaps, and a well resolved step at the edge.

AFM offers precise, non-destructive, and accurate topographic characterisation at micro and nanoscales. However, the occurrence of measurement artifacts is also common, depending on the nature of the sample under test, as well as the dimensions and orientation of the tip utilised. It is therefore essential to recognise artifacts in AFM images in order to avoid misinterpretation of the acquired data. As depicted in **Figure 3.14c**, a common unwanted feature when measuring arrays at the nanoscale is a loss of resolution due to a tip/sample convolution effect caused by the tip finite sharpness interacting with a periodically patterned surface [187]. This occurs when the tip is in contact with more than one edge of the sample simultaneously. A clear example of such effect is shown in **Figure 3.14d**, where loss of spatial information in the x and z axes can be appreciated within the gaps of an array of

hybrid silicon/GST nanocylinders (discussed in **Chapter 5**). At the edge of the array, however, dimensions along the z axis are well resolved due to the absence of periodicity, showing a total array thickness of 220 nm. Convolution effects can be sorted out via employing expensive ultra-sharp tips to increase both in plane and out of plane resolution [187]. Alternatively, in-plane spatial information can be complemented using other morphological characterisation techniques, such as scanning electron microscopy described in the next section.

3.3.4 Scanning electron microscopy

In scanning electron microscopy (SEM), a high energy focused beam of electrons is used to scan a specimen. Interaction between accelerated electrons and the sample produces a wide range of EM signals such as secondary electrons, back scattered electrons, characteristic x-rays and visible light [188]. These signals are detected by an appropriate sensor and can be used to obtain morphological and chemical information about the specimen under test. For example, the detection of secondary and back scattered electrons can be used to image a sample with magnifications from x10 to x500 000, allowing for a spatial resolution down to tens of nanometers. On the other hand, some SEM systems are equipped with x-ray detectors, which can be used to analyse characteristic x-rays and thus to map the chemical properties of the specimen via energy-dispersive spectroscopy (EDS).

In this thesis, morphological sample characterisation has been carried out using an SEM (TESCAN VEGA3 SEM) in combination with AFM described in the previous section. **Figure 3.15a-c** shows three examples of SEM images from various devices fabricated. Note that, contrary to AFM scans shown in **Figure 3.14d**, well resolved gaps between nano cylinders in **Figure 3.15c** can be now observed and measured.

In addition, the TESCAN VEGA3 SEM is combined with an EDS X-ray detector (X-MAXN EDS, Oxford instruments) which was employed to ensure a correct atomic composition of the as-deposited thin films. For example, **Figure 3.15d** shows an EDS measurement of $Ge_2Sb_2Te_5$ thin films employed in this thesis, confirming that the bulk material composition has been successfully transferred to the film during the sputtering process (Ge 21.0%, Sb 24.6%, Te 54.5%).

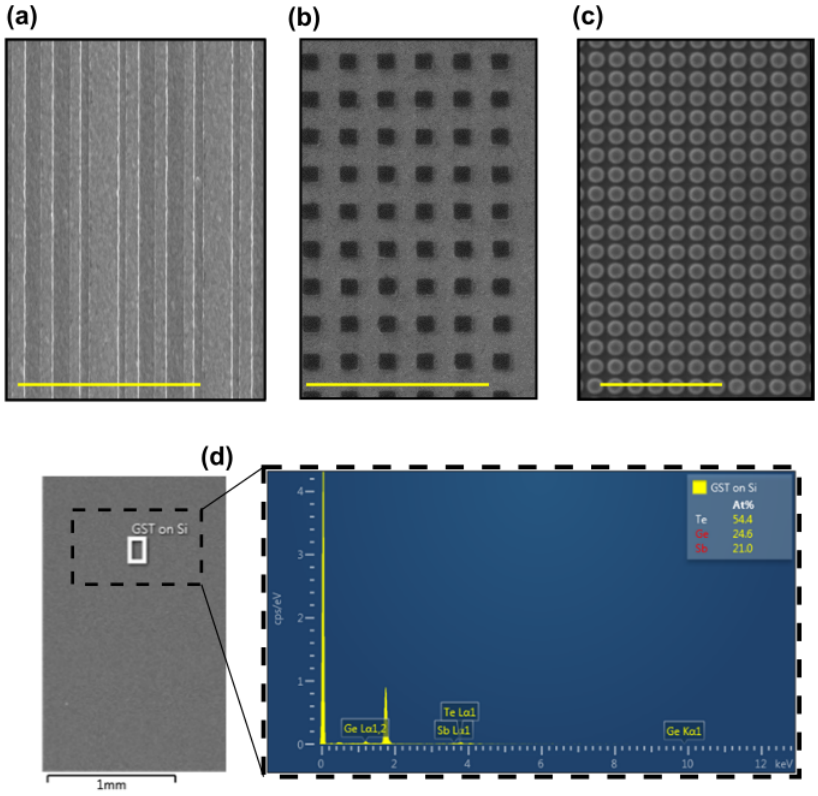

FIGURE 3.15: **(a-c)** SEM images of 3 different phase-change meta-devices developed in this thesis (scale-bar is 5): **(a)** Plasmonic phase-change beam steerer (Chapter 4), **(b)** EBL dose test for the realisation of GST nano-cubes on gold (Chapter 6) **(c)** Array of all-dielectric hybrid silicon/GST nano cylinders (Chapter 5). **(d)** EDS measurement of a 200 nm thick amorphous GST film, confirming an adecuate film composition (Te 54.5 %, Sb 24.6 %, Ge 21.0 %).

3.3.5 X-ray diffraction

X-ray diffraction (XRD) is a material characterisation technique which is primary used to obtain information about the structural phase and dimensions of crystals. Since the wavelength of x-rays (λ = 0.01 nm to λ = 10 nm) is comparable to the inter-atomic spacing of crystalline materials, the main principle of such technique is based on the Bragg effect [5], which can be used to analytically extract dimensional and morphological information of a crystalline structure, In this thesis, XRD was employed to confirm the amorphous to crystalline phase transition of PCMs after an annealing process, as well as to identify the nature of the resulting structural phase (e.g. cubic, hexagonal...). A picture of the instrument employed for such measurements (Bruker D8 advanced) is shown in **Figure 3.16a**. Briefly, it consists of an X-ray gun, a sample holder and and an X-ray detector. The X-ray source is stationary, whereas the the sample moves by an angle θ (and the detector by 2θ

accordingly) in order to scan the sample at different angles of incidence.

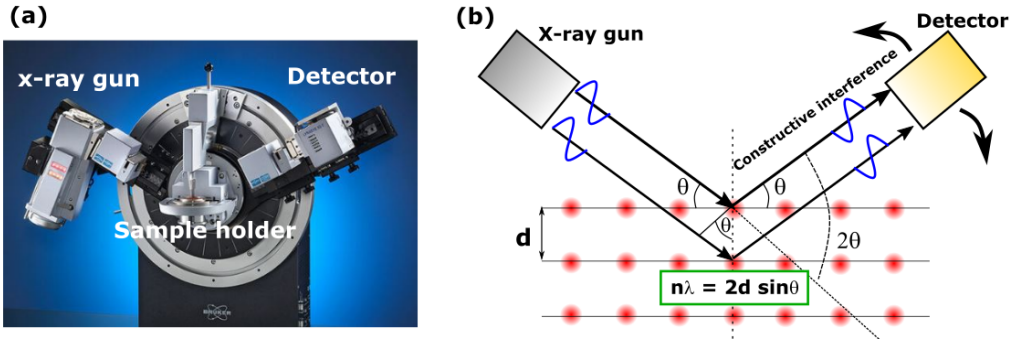

FIGURE 3.16: X-ray diffraction **(a)** Photograph of the instrument employed for XRD measurements, model Bruker D8 advanced. Picture reproduced from the public domain (www.Bruker.com) **(b)** Schematics summarising the Bragg condition in a crystalline atomic structure under the x-ray EM regime.

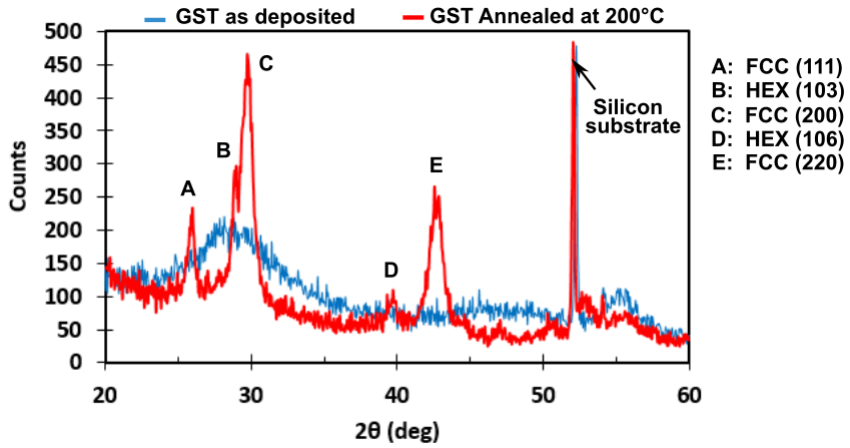

FIGURE 3.17: Typical X-ray diffraction measurement of an as-deposited 100 nm GST thin film before (blue) and after (red) annealing at 200°C, confirming crystallisation of the film due to the presence of interferencial Bragg peaks.

A simple case of study is summarised in **Figure 3.16b**, where a wave reflected by the second atomic row will have a path difference of $dsin\theta$ with respect to the wave reflected by the first row, with d being the crystal lattice and θ the angle of incidence. Following the Bragg condition,

$$dsin(\theta) = \frac{n\lambda}{2} \tag{3.8}$$

when $dsin\theta$ happens to be equal to an integer of half of the incident wavelength, the waves reflected at each row will be in phase and thus interfere constructively and reinforce each other, resulting in an increase of the signal detected. The relation between the incident/collection angles and the signal detected allows therefore to

obtain information about the atomic structure and compare it to a database in order to identify the nature of the crystal under test.

Figure 3.17b shows a typical XRD measurement of an as deposited (amorphous) $Ge_2Sb_2Te_5$ film on a silicon substrate, compared to its crystalline phase after an annealing process (10 minutes in a hot plate at 200 °C) . Due to the absence of an ordered lattice in the amorphous phase, only 1 peak corresponding to the silicon substrate can be detected. After crystallisation however, strong Bragg signals coming from the characteristic GST centered cubic phase (FCC) can be observed, as well as some evidences of weak peaks corresponding to the hexagonal phase (HEX), which usually takes place at higher annealing temperatures (> 250 °C) [189, 190].

Chapter 4

Near-Infrared Active Phase-Change Plasmonic Beam Steerers

4.1 Introduction and motivation

Compact beam steering with no moving parts would revolutionise technological systems based on random access pointing, such as free-space inter/intra chip interconnects for optical telecommunications. In such systems, optical beams are commonly guided and focused through conventional bulky optics such as moving mirrors or prisms and lenses, which are slow in nature and occupy large amounts of space. Optical telecommunications would therefore benefit from new technologies offering dynamic, and high speed beam steering and shaping capabilities. Reconfigurable, optically-thin phase-gradient metasurfaces (i.e. where the beam steering capabilities are not locked-in at the fabrication stage) would allow not only for high-speed and compact optical telecommunications, but would also open up a new route to a variety of exciting applications, such as light imaging detection and ranging (LIDAR) scanning systems for autonomous vehicles, robotics or sensing. On the other hand, such an approach employing phase-change materials has not been experimentally realised so far.

In this chapter, therefore, the non-mechanical beam steering capabilities of phase-change materials combined with plasmonic phase gradient metasurfaces is investigated, and a working prototype device based on this technology is successfully designed, fabricated and tested. As depicted in **Figure 4.1a**, the proposed PCM based reconfigurable beam steering meta-devices consist of plasmonic metal/insulator/metal

1D metasurfaces with an embedded GST thin layer serving as a tunable environment. The devices were designed to operate in the NIR C-band (λ = 1530 nm to λ = 1570 nm, particularly at λ = 1550 nm) due to its technological importance in optical telecommunications [191].

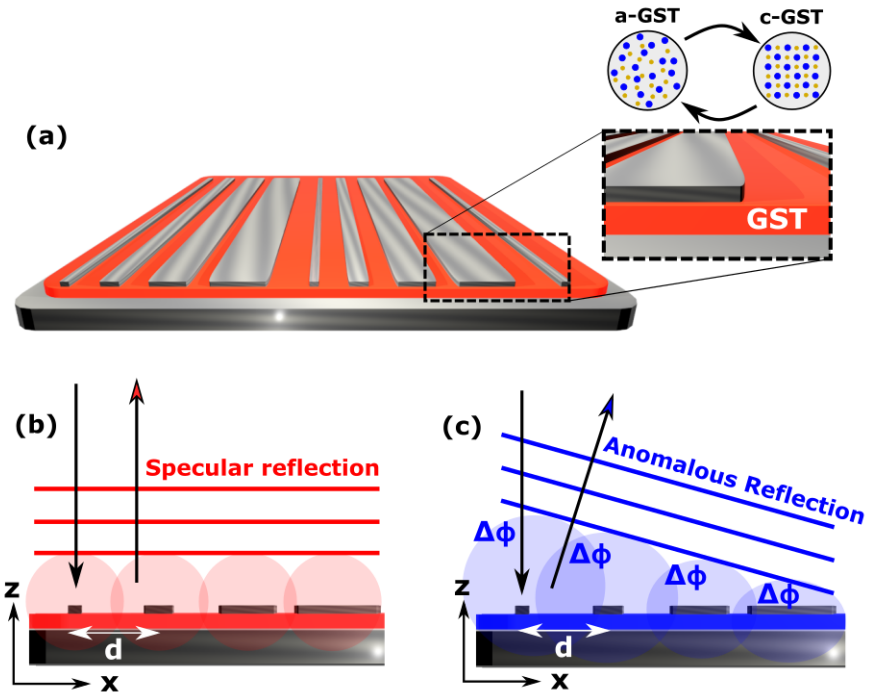

FIGURE 4.1: **(a)** Phase-change beam steering meta-device concept. The dielectric spacer of a typical MIM metasurface configuration is filled with a tunable PCM (here GST) to change its EM response. **(b-c)** Huygens' principle showing the wavefront reconstruction when the GST is crystalline **(b)** and amorphous **(c)**.

When the GST layer is in its crystalline state, the structure behaves as a mirror-like surface, and thus light is reflected according to conventional specular reflection laws where the angle of reflection θ_r is equal to the angle of incidence θ_i (**Figure 4.1b**). In the amorphous state, however, the device has been specifically designed to operate as an optical phase-gradient metasurface. That is, as shown in **Figure 4.1c**, each antenna has been properly arranged to introduce a linear optical phase shift $\Delta\phi$ with respect to its neighbour along the x-axis. The sum of these local phase jumps results in a constructive interference at a pre-designed anomalous angle of reflection, dictated by the generalised Snells law shown in eq. 2.21 [6]. The developed device allows therefore to selectively change the angle of reflection without the need of mechanically-rotating mirrors or bulky optics, by simply changing the phase-change medium between its two meta-stable states. The use of PCMs in combination with

metasurfaces offers therefore real applications advantages, such as compactness, fast switching times (potentially in the time scales of nanoseconds) and, due to the non-volatile nature of chalcogenide phase-change materials, low power consumption [33].

4.2 Metasurface design and analysis

4.2.1 Unit and super-cell design

As discussed in C**hapter 2 (section 2.3**), MIM based metasurfaces are well known for their versatility in manipulating the amplitude and phase of light, and require relatively simple building blocks with only one lithography step [96, 115, 116, 124]. In addition, phase-gradient metasurfaces based on MIM configurations are capable of achieving near 2π optical phase coverage in reflection, as well as beam shaping efficiencies up to 80% in the NIR [115, 124]. Therefore, a MIM architecture was chosen for the development of this device.

The scattering properties (i.e. phase and amplitude in reflection) of the MIM unit cell were first analysed via finite element modelling (as described in **section 3.1.1**), using a generic structure depicted in **Figure 4.2a**. It consists of a dielectric layer of varying thickness t and refractive index n_D sandwiched between a continuous aluminum layer and a top 1D strip-like Al antenna. To account for the unavoidable dielectric losses present in GST, the absorption coefficient of the spacer was fixed to k = 0.07, i.e. the same as that of amorphous GST at λ = 1550 nm (the refractive index and absorption coefficient for both amorphous and crystalline states are shown in **Figure 4.2b**). The pitch spacing d was set to 700 nm to provide a good compromise between reducing unwanted diffraction effects while keeping a sufficiently large spacing between antennas to ease the fabrication process. The dielectric spacer thickness t, antenna width w and refractive index n_D were set as variables. Note that the use of strip-like 1D antennas allows for a faster computation time, since the structure can be simulated in 2D due to its translational symmetry. This means however that the devices are polarisation sensitive; thus they operate under transverse-magnetic (TM) polarisation. On the other hand, additional device functionalities could arise

from such anisotropy, as will be discussed later in this chapter. Polarisation insensitivity could be anyway readily achieved using square or circular-shaped antennas [46, 112, 115, 170]).

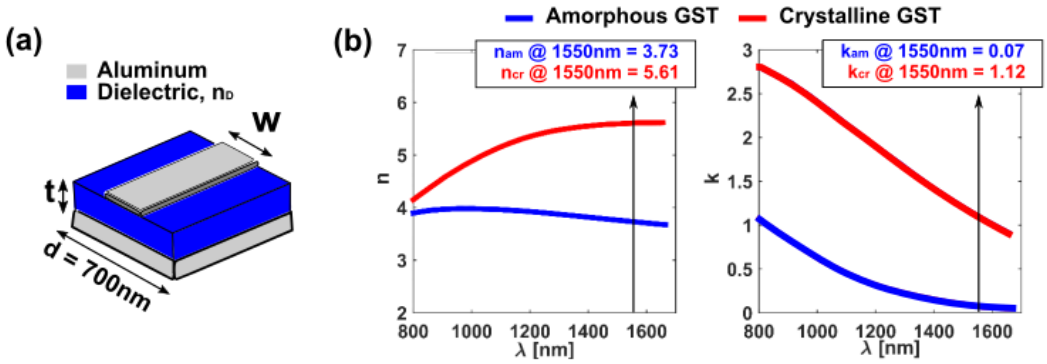

FIGURE 4.2: **(a)** Generic unit cell structure used to numerically study the scattering properties of MIM plasmonic resonators, where t is the thickness of the dielectric spacer, w is the antenna width, and n_D is the dielectric refractive index. **(b)** Refractive index (left) and absorption coefficient (right) of amorphous and crystalline GST in the NIR. The values at the design wavelength (λ = 1550 nm) are highlighted.

Figure 4.3a shows the computed amplitude (left) and phase (right) results (in reflection) at λ = 1550 nm for a spacer thickness of t = 60 nm. Both amplitude and phase were computed as a function of the dielectric spacer refractive index n_D (ranging from n_D= 1 to n_D= 4) and the antenna width w (from w = 100 nm to w = 650 nm) for an excitation wavelength of λ = 1550 nm. From these results, the three characteristic GSP resonant regimes can be identified [118, 192, 119]:

- **when 1 < n_D < 2.5**

  This region offers a continuous near 2π optical phase control with superior efficiency when varying the antennae width w (i.e. when going in and out of the GSP resonance). As described in **section 2.3.1**, such parametric space corresponds to the overcoupled (underdamped) resonant regime, which is the most suitable space to design metasurfaces for wavefront engineering [118, 192].

- **when 2 < n_D < 2.5**

  Again, a near 2π phase coverage can be achieved via varying the antennae with w. However, the amplitude (reflectance) of the first order (m = 1) GSP

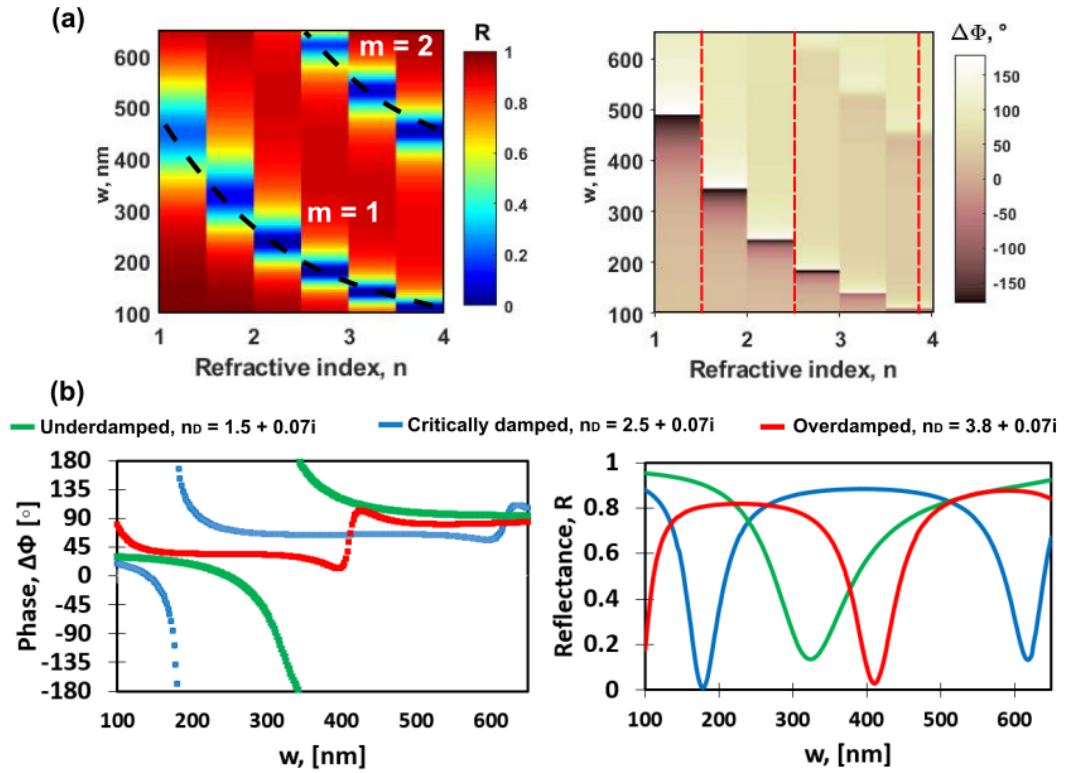

FIGURE 4.3: **a)** Amplitude (left) and phase (right) as a function of the dielectric spacer refractive index n_D and antenna width w for t = 60 nm. **(b)** Cross section plots showing an example of the characteristic phase (left) and amplitude (right) response of a MIM configuration as a function of the antenna width w in the 3 resonant regimes (undercoupled, overcoupled and critically coupled), for a spacer thickness of t = 60 nm.

mode drops to near 0%. This regime is known as critical coupling [7, 118, 192], and results in light being perfectly absorbed by the system. Such phenomenon can be quite attractive for certain applications such as photovoltaics or signal modulation, but at the same time it is something to avoid when designing devices based on optical phase wavefront control, where the amount of light phase-shifted and re-radiated to the free-space should be ideally kept to a maximum [6].

- **when $n_D > 2.5$**

  Due to an increase of the refractive index, and thus an increase of the effective GSP mode index (see eq. 2.18, a second order mode (m = 2) can be identified when varying the aluminum antenna width. It is also noted that the amount of phase coverage is significantly reduced to below $\sim 180\ ^\circ$, thus the system operates under the undercoupled (overdamped) regime [118, 192].

For more clarity, **Figure 4.3b** shows a 2D plot containing the scattering phase (left) and amplitude (right) response of the three resonant regimes described above (i.e. undercoupled, critically coupled and overcoupled). The optimum refractive index range is therefore the one that satisfies the overcoupled condition (from n_D = 1 and n_D= 2.5), since it provides a good compromise between amount of phase coverage (near 2π) and efficiency.

Since the refractive index of GST is significantly higher than 2.5 in both amorphous (n_{aGST} = 3.73) and crystalline (n_{cGST} = 5.61) states, fully filling the dielectric spacer with GST is therefore an impracticable option from a design point of view, as revealed in **Figure 4.3b** (red curve), where only a maximum optical phase span of $\Delta\phi_{max}$ = 110 ° can be achieved. This is clearly insufficient for a versatile designer interface, where ideally a 2π phase coverage is desired to increase the realisable number of designs [6, 93, 113, 118]). To overcome this limitation, the combination of low-index, loss-free dielectric films (SiO_2) with deeply subwavelength sized ($\approx \frac{\lambda_0}{60}$) GST layers was proposed to hybridise the dielectric spacer. A schematic of the resulting unit cell is depicted in **Figure 4.4a**. Here, a 33 nm thick SiO_2 layer (t_{SiO_2}) fills half of the dielectric spacer volume, while a GST layer sandwiched between two 5 nm thick ITO films (to avoid oxidation of the PCM) occupies the space. The GST thickness was fixed to t_{gst} = 26 nm, as it was found to provide a good compromise between reducing the effective refractive index of the layer stack, while contributing to a sufficient amount of active volume to tune the optical response of the device after crystallisation. **Figures 4.4b** and **4.4c** show the computed phase and amplitude response in reflection respectively (the complex refractive indices of Al, ITO and SiO_2 employed for the calculations can be found in **Appendix B, section B.1**). As expected, splitting the dielectric spacer between optically thin low and high index materials (SiO_2/ITO and amorphous GST respectively) allows a reduction of the effective refractive index of the stack, thus locating the GSP resonance in the overcoupled regime required for a better optical phase control (here up to $\Delta\phi \approx 300°$) [118, 192]. After crystallisation of the GST layer, the phase profile as a function of the antenna width w becomes nearly flat **Figure 4.4b**. As shown previously (in **Figure 4.3b**), this is due to an increase in both real and imaginary parts of the GST

refractive index, which shifts and locates the GSP resonance in the overdamped (undercoupled) regime after crystallisation.

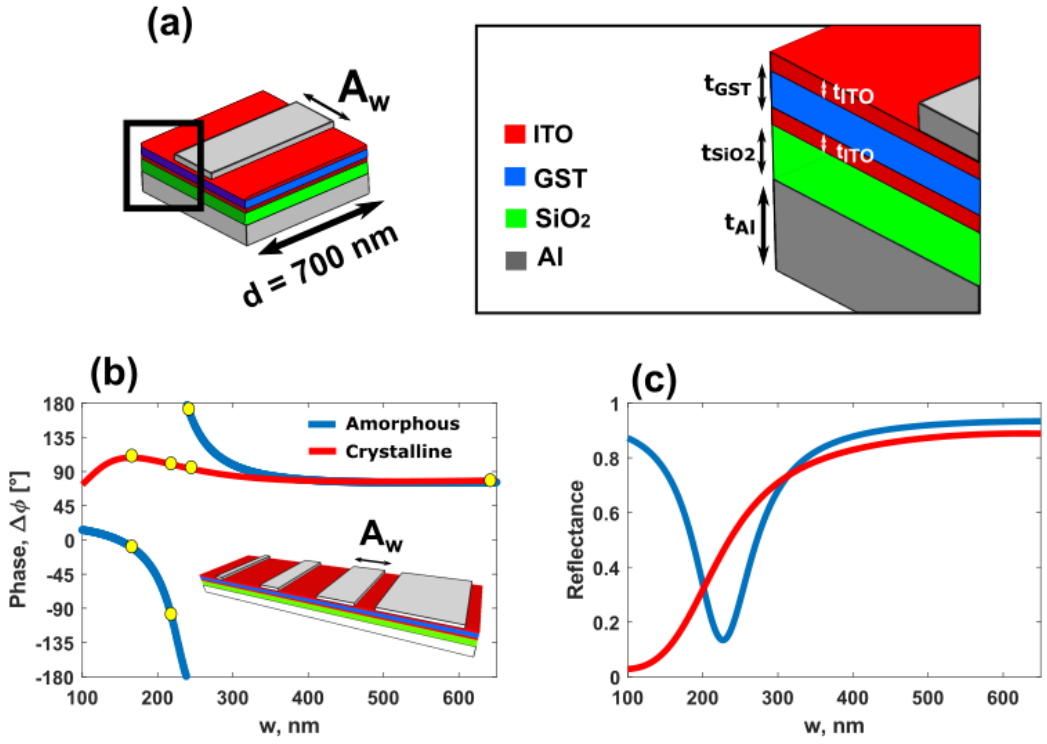

FIGURE 4.4: **(a)** Schematics showing thicknesses and dimensions of the unit cell, where t_{Al} = 100 nm, t_{SiO_2} = 33 nm, t_{ITO} = 5 nm, t_{gst} = 26 nm, and d = 700 nm. The width of the top aluminum antenna (w) can be varied to tune the optical phase response upon reflection. **(b)** Phase in reflection as a function of w for both amorphous (blue) and crystalline (red) states of the GST layer. The yellow dots correspond to the antenna sizes selected to build the super-cell represented by the inset (w_1 = 166 nm, w_2 = 214 nm, w_3 = 239 nm, and w_4 = 650 nm). **(c)** Reflectance as a function of w for amorphous (blue) and crystalline (red) states.

Due to the near 2π optical phase coverage offered by the proposed device unit cell in the amorphous phase, different types of active beam steering configurations can be therefore designed via changing the unit cell period d and/or the local phase increment $\Delta\phi$ imposed by each element of the array (see eq. 2.21 and [127]). Anomalous reflection can be then selectively switched to ordinary reflection via crystallisation of the GST layer, as the resulting phase profile when varying w becomes flat. Here specifically, a super-cell based on four "amorphous antennas" with each imposing a phase increment of $\Delta\phi = 90°$ has been chosen. The required antennae widths w to satisfy this condition are marked with yellow dots in **Figure 4.4b**. According to the generalised Snells' law (eq. 2.21), for a period of d = 700 nm and a wavelength λ= 1550 nm, such arrangement gives an anomalous angle of reflection

θ_r = 33.6 ° when the GST layer is amorphous. After crystallisation, the linear phase gradient along the surface is cancelled, leading to ordinary reflection (i.e. $\theta_r = \theta_i$), with negligible maximum phase differences between elements of $\approx 17°$ when the GST layer in the crystalline state.

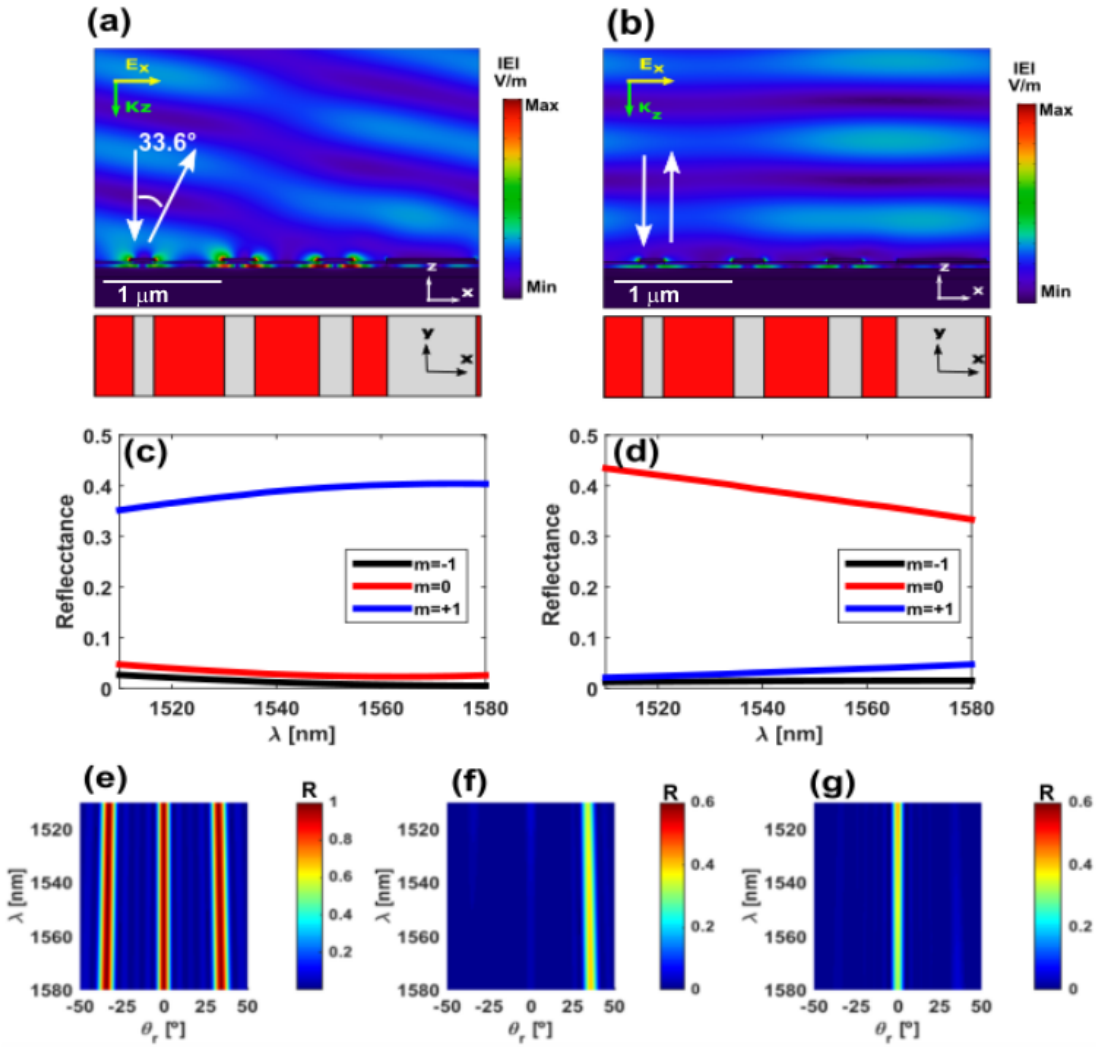

FIGURE 4.5: **(a-b)** Instantaneous electric field distribution under normal incidence excitation, confirming: **(a)** anomalous reflection (θ_r = 33.6°) when the GST layer is amorphous, **(b)** ordinary specular reflection when the GST layer is crystalline. **(c-d)** Numerically resolved reflectance of the three diffraction orders (m = 1, m = 0, and m = +1) when the device is amorphous **(c)**, and crystalline **(d)**. **(e-g)** Normalised far-field radiation pattern for an array made of 10 super-cells, and calculated via eq. 4.1 **(e)**. Angular and spectral response of the device for its two operational modes: anomalous reflection when the GST layer is amorphous **(f)**, and specular reflection in the crystalline state **(g)**.

4.2.2 Analysis of the device performance

The radiation pattern (i.e. its reflectance as function of the angle of reflection θ_r) of the proposed PCM-enabled metadevice was assessed via simulation of an infinite array of the super-cells shown in the inset of **Figure 4.4b**. **Figures 4.5a** and **b** show the instantaneous electric field distributions under normal incidence conditions, confirming anomalous reflection when the GST layer is amorphous, and ordinary mirror-like reflection when crystallised. The spectral and angular characteristics of the device were then analysed via grating and antenna theory. The far-field behavior can be interpreted in a similar way to a conventional diffraction grating of period Λ = 2800 nm [11, 193], but with the majority of the power being radiated towards the first diffraction order (m = +1) when the GST layer is amorphous, and in the zeroth order (m = 0) when it is crystalline.

Figures 4.5 and **d** show the numerically computed reflectance of the three diffraction orders (m = $\pm$ 1, m = 0), over a range of wavelengths from 1515 to 1580 nm for amorphous and crystalline GST respectively. The anomalous efficiency (m = +1) is, over this range, always above 36% while the residual ordinary reflectance (m = 0) is less than 4%. With the GST layer in the crystalline state, ordinary reflection dominates (m = 0), with an overall reflection efficiency above 32% and a small residual anomalous reflection (m = +1) below 5%. This can be attributed to the phase profile after crystallisation (shown in **Figure 4.4b**, which is not completely flat as it ideally should be. Increasing the volumes of GST was found to flatten the phase profile in the crystalline state (due to further resonant damping and shifting), but on the other hand the optical performance in the amorphous phase was significantly degraded in terms of both amount of optical phase coverage and efficiency. The best compromise between amorphous and crystalline states is located, as expected, at the design wavelength (λ = 1550 nm) with 40% reflection efficiency for both anomalous and specular reflection modes. The missing energy is inherently absorbed by the array as plasmonic and dielectric losses in the aluminum and ITO/GST, respectively.

The normalised far-field radiation pattern of the device was then calculated independently via the array factor (AF), which under normal incidence conditions

becomes [100]:

$$AF^2 = \frac{1}{N^2}\left[\frac{\sin\left(\frac{Nk_0\Lambda\sin(\theta_r)}{2}\right)}{\sin\left(\frac{k_0\Lambda\sin(\theta_r)}{2}\right)}\right]^2 \tag{4.1}$$

Here, Λ is the period of the super-cell (made of 4 unit-cell elements of period d = 700 nm, thus Λ = 2800 nm), θ_r is the angular coordinate in reflection, and N is the number of supercells taken into account (which has direct influence on the width, thus directionality of the diffraction lobes). **Figure 4.5e** shows the normalised far-field distribution calculated using 4.1 for N = 10.

The final radiation pattern containing both spectral and angular characteristics of the device was then calculated by multiplying the numerically obtained reflectance coefficients of the three diffraction orders shown in **Figures 4.5b-c** by the normalised radiation pattern calculated via eq. 4.1. **Figures 4.5** and **g** show the results for the amorphous and crystalline states of the GST layer, i.e., for anomalous and ordinary specular reflection, respectively.

4.3 Fabrication of Phase-Change Plasmonic Beam Steerers

Batches of PCM-enabled beam-steering metadevices were fabricated in areas of 70×70 μm as follows (a schematic flowchart of the fabrication process is depicted in **Figure 4.6**):

1. First, 1×1 cm SiO_2/Si substrates were cleaned in acetone under sonication for 10 min, and rinsed with isopropyl alcohol (**Figure 4.6a**).

2. Next, the continuous layer stacks were deposited onto the previously cleaned substrates using magnetron sputtering in an Ar atmosphere (Ar flow 10 sccm). The base pressure was 1×10^{-6} mbar, and the sputtering Ar pressure was 1.3×10^{-6} mbar. DC sputtering was used for the deposition of conductive materials (i.e. GST, ITO and Al) , whereas RF sputtering was employed for the SiO_2 layer. (**Figure 4.6b**).

3. As shown in **Figure 4.6c**, a 250 nm thick layer of positive PMMA resist (Microchem 950K A4) was then spun (6000 rpm) onto the sample and baked at

low temperatures (70 °C) for 15 min to harden the resist while avoiding crystallisation of the GST layer (since the as-deposited GST state was amorphous).

4. An e-beam lithography process was carried out to transfer the nano-strip antennae pattern onto the resist (**Figure 4.6d**). The writing was made employing low currents of 1.5 nA and high voltages of 80 kV in order to increase the pattern resolution [194]. A dose test was carried out with exposure doses ranging between 4 and 11 Cm^{-2} in increments of 0.25 Cm^{-2}, to increase the chances to hit the correct sizes. Optimum doses were found to lie between 7 and 8 Cm^{-2}.

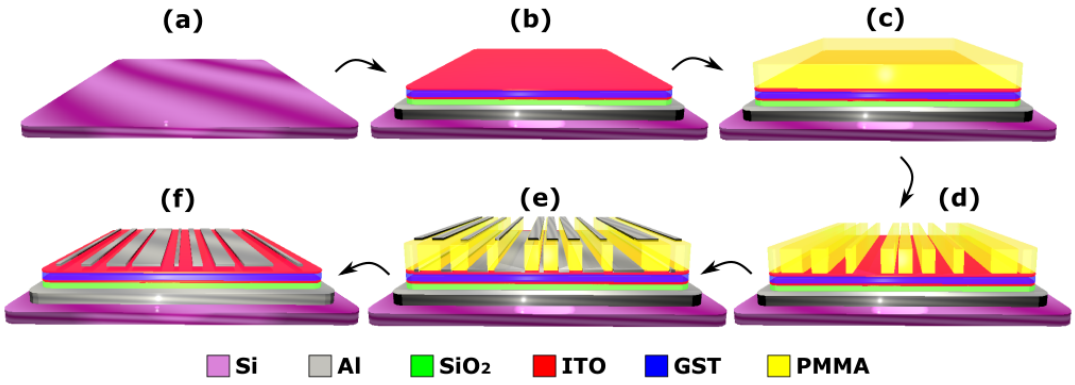

FIGURE 4.6: Schematics summarising the fabrication of phase-change plasmonic beam steerers. **(a)** SiO_2/Si substrate cleaning in acetone and isopropyl alcohol **(b)** Magnetron sputtering of the layer stacks **(c)**, PMMA spin coating and e-beam exposure **(d)** PMMA development **(e)** Magnetron sputtering of aluminum **(d)** PMMA lift off.

5. The resist was then developed in a 15:5:1 (isopropyl alcohol:methyl isobutyl ketone:ethyl methyl ketone) solution for 30 s at room temperature in order to dilute and remove the exposed regions (**Figure 4.6d**). The sample was gently shaked during the process.

6. Aluminum antennae were sputtered inside the mask pattern, using the same conditions as for the bottom aluminum layer, described in step 2 (**Figure 4.6e**).

7. Finally, The PMMA/aluminum masks were removed by first delaminating most of the film using warm acetone flow from a pipette and subsequent soft sonication in acetone for 5 min (**Figure 4.6f**). Pictures of the as-fabricated devices at different scales are shown in (**Figure 4.7**).

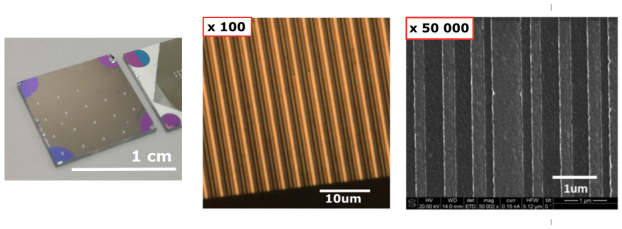

FIGURE 4.7: Pictures of the as-fabricated phase-change plasmonic beam steering devices. From left to right: a photograph of a 1×1 cm chip containing various arrays; an optical microscope image; and an SEM image showing fine details of the plasmonic antennae.

4.4 Optical characterisation: radiation patterns

Devices were optically characterised via NIR Fourier imaging micro-spectroscopy, which allows for angle-resolved reflectance measurements at the micro-scale [181], as described previously in (**section 3.4.2**). Results from such measurements are depicted in **Figure 4.8**. Particularly, **Figure 4.8a** and **4.8b** show the measured radiation pattern, compared to simulations for both amorphous and crystalline states of the GST respectively. It can be seen that indeed, the as-fabricated device reflects anomalously with the GST layer in the amorphous phase. The anomalous reflection angle was found to be $\theta_r \approx 33 \pm 3°$, matching, within experimental error, the design angle of 33.6°. The overall efficiency across the whole spectral band (from 1515 to 1580 nm) when operating in anomalous reflection mode was found to be above 34%, again in line with design predictions (numerical simulations). After thermal crystallisation, the device reflects in an ordinary specular fashion at $\theta_r = 0°$, with an efficiency across the range of wavelengths measured above 22 % (*cf.* 32 % from the numerical simulations). Small discrepancies in the crystalline state could be caused by the several factors such as:

- A mismatch (between simulations and experiment) of the complex refractive index of crystalline GST.
- Changes in the ITO refractive index after annealing [195].
- Device fabrication errors such as layer stack thicknesses.
- Surface imperfections not taken into account in simulations, such as roughness or the presence of native aluminum oxide islands around the Al resonators.

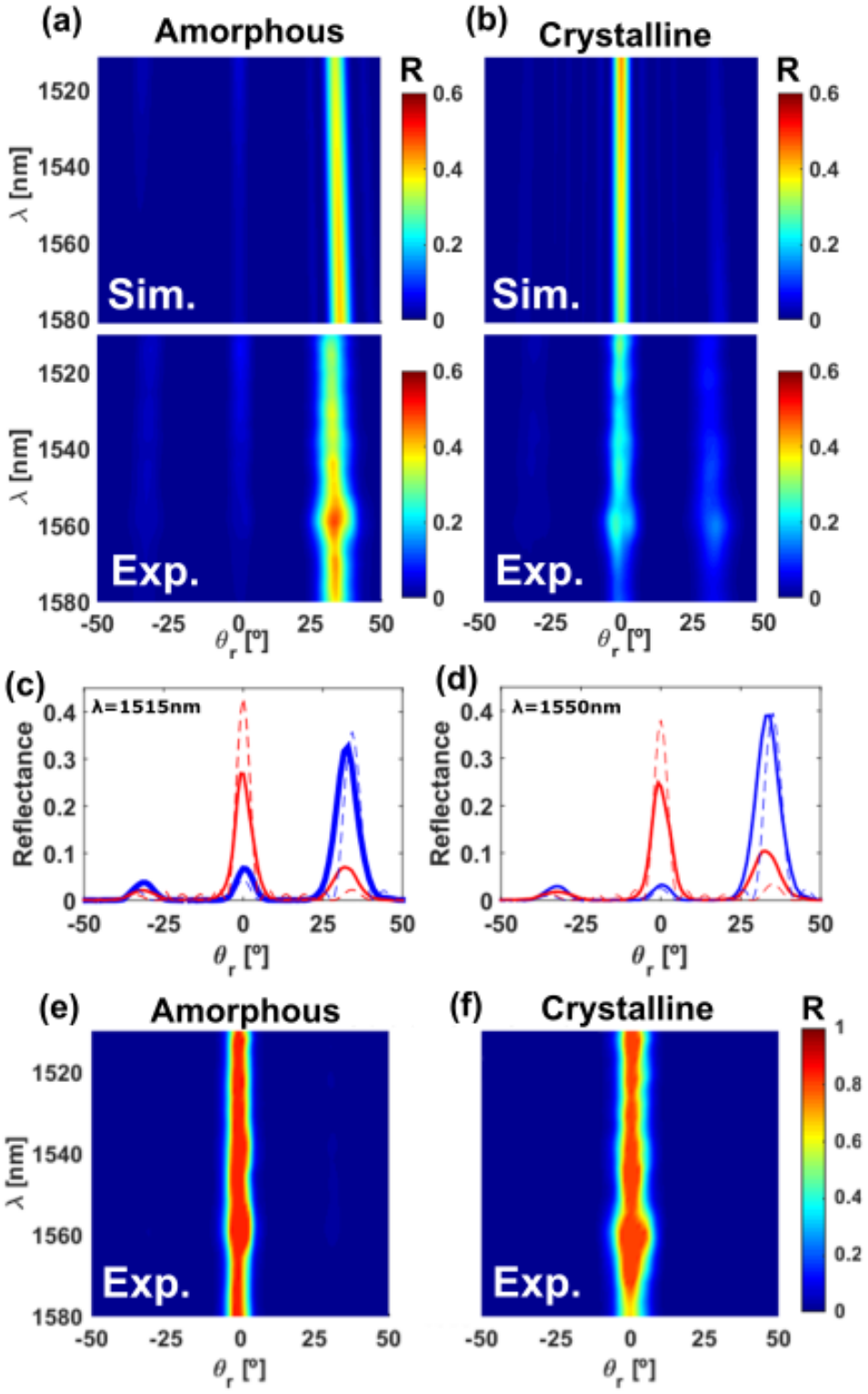

FIGURE 4.8: Optical characterisation of PCM enabled beam steering meta-devices. **(a-b)** Measured angular reflectance under TM excitation, compared to simulations across the C-band for both amorphous **(a)** and crystalline **(b)** states. **(c-d)**Transverse 2D plots showing details of the measured angular reflectance (solid) against numerical simulations (dashed) at two different wavelengths: **(c)** λ = 1515 nm, and **(d)** λ = 1550 nm. **(e-f)**

For more clarity of the results, **Figures 4.8c-d** show the measured angular reflectance (solid curve) of the as-fabricated devices, compared with simulations (dashed curve) for both anomalous (blue) and specular (red) reflections and at λ = 1515 and λ =1550 nm, respectively. At the design wavelength (λ = 1550 nm), the agreement between experiment and simulation for the GST in the amorphous state is striking, with only a small decrease in device performance (*cf.* simulation) for the crystalline state. The best balance between states was found at 1515 nm with ≈30 % of light being reflected both anomalously (at ≈32° at this wavelength) and specularly (i.e., at 0°).

For curiosity, the device performance under transverse-electric (TE) polarisation was also measured, and the obtained results are shown in **Figure 4.8e** and **Figure 4.8f** for amorphous and crystalline states respectively. As expected, due to the translational symmetry (thus anisotropy) of the Al antennas as well as to the abscence of periodicity in one axis, the device reflects light specularly in both amorphous and crystalline states across the whole spectrum. These results suggest that the proposed configuration could also have tunable polarising beam splitting capabilities, which could be further investigated in the future. For example, in the amorphous phase one should expect splitting of the electric field component perpendicular to the 1D antennas towards the predesigned anomalous reflection angle (here 33°) when the structure is excited with circularly or eliptically polarised light, with the splitting effect being cancelled after crystallisation.

4.5 Optically induced reversible switching

Finally, the device switching capabilities (i.e. its ability to be reversibly changed between amorphous and crystalline states over repeated cycles) were demonstrated via optically induced heating using a scanned laser. A diagram of the optical system employed is depicted in **Figure 4.9**. The setup can be divided in 3 optical channels:

Finally, the device switching capabilities (i.e. its ability to be reversibly changed between amorphous and crystalline states over repeated cycles) were demonstrated via optically induced heating using a scanned laser. A diagram of the optical system employed is depicted in **Figure 4.9**. The setup can be divided in 3 optical channels:

1. A CCD camera fed by a visible light source (Thorlabs MCWHLP1) to obtain visual information about the sample and localise the region to switch.

2. A shutter-assisted, fiber-coupled, blue-wavelength pulsed laser (λ = 405 nm, model RS 713-3908) focused onto the sample to optically switch the GST layer.

3. A fiber-coupled NIR micro-spectrometer fed by a source (Thorlabs HEP3965) to obtain the sample reflectance spectra after each laser scan.

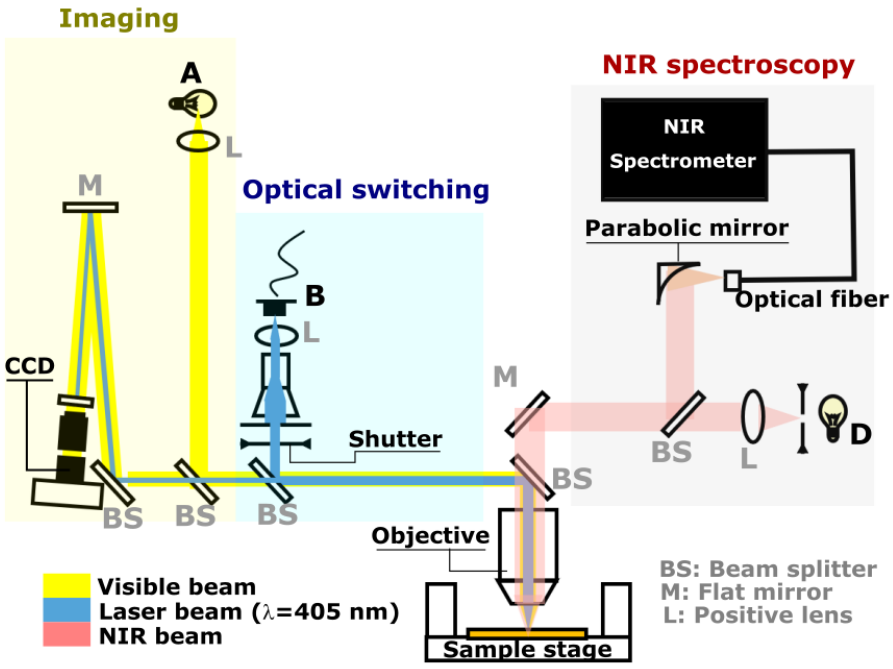

FIGURE 4.9: Optical setup employed for the laser switching experiments

Laser Parameter	Crystallisation	Re-amorphisation
Pulse Duration (ns)	200	20
Pulse Rise/fall time (ns)	50	1
Pulse Peak Power (mW)	6	18
Pulse Repetition Rate (Hz)	1×10^5	1×10^3

TABLE 4.1: Laser parameters employed for optically driven crystallisation and re-amorphisation of the plasmonic phase-change beam steering devices.

Crystallisation and re-amorphisation cycling experiments (or "SET" and "RESET" cycling in phase-change terminology) were carried out on both “blanket” film structures and as-fabricated devices in areas of 40 x 40 μm. A scanning-pulsed laser (λ = 405 nm) was focused into an 0.5 μm diameter spot through an Olympus LMPLFLN

50x objective (NA 0.5) across a zig-zag path with a speed of 50 μm/s and a pitch distance between adjacent lines of 0.433 μm. Switching experiments were first performed over the Al/SiO_2/ITO/GST/ITO multilayer stacks (outside of the top Al antenna array) in order to determine the optimum laser parameters required for the switching in terms of power, pulse duration, rise/fall time and repetition rate, without potentially damaging the devices. Crystallisation and re-amorphisation laser switching experiments were made with single pulses, and specifications are shown in **table 4.1**.

Figure 4.10a shows four images of an unpatterned device area after two successive SET and RESET cycles, where a change in reflectance on changing phase is clearly apparent (i.e. crystal regions are lighter than amorphous regions due to a change in the reflectivity). For more quantitative data, verification of the occurrence of phase switching as a result of such experiments was carried out by measuring the in-situ reflectance, and comparing with results from thermally crystallised devices (i.e. via hot plate annealing at 200 °C for 10 min) previously measured with an XRD system to check the sample crystalinity (see section 3.4.5). **Figure 4.10b** shows the results from these measurements, revealing a very good agreement between the NIR spectra for as-deposited amorphous/thermally crystallised samples and those subjected to the optically induced phase changes, which confirms successful reversible switching between states in the unpatterned device region.

The experiment was then repeated for completed devices (i.e., in regions with the top-patterned Al antenna array). The resulting microscope images are shown in **Figure 4.10c** and the corresponding NIR reflectance spectra under TE illumination in **Figure 4.10d**. Again, very good agreement between the NIR spectra for optically switched devices and the fully amorphous (as-deposited) and fully crystalline (thermally induced) cases confirms successful laser-induced switching of the device itself. In the case of TM illumination (see **Figure 4.10d**), the devices have beam steering capabilities, thus most of the reflected power is concentrated in the first diffraction order when the GST is amorphous (**Figure 4.10f-top**), and in the zeroth order after crystallisation (**Figure 4.10f-bottom**). The large numerical aperture of the lens (NA 0.5) collects light from both states (were the scattering efficiency is similar), resulting in small changes in the reflectance spectra between phases.

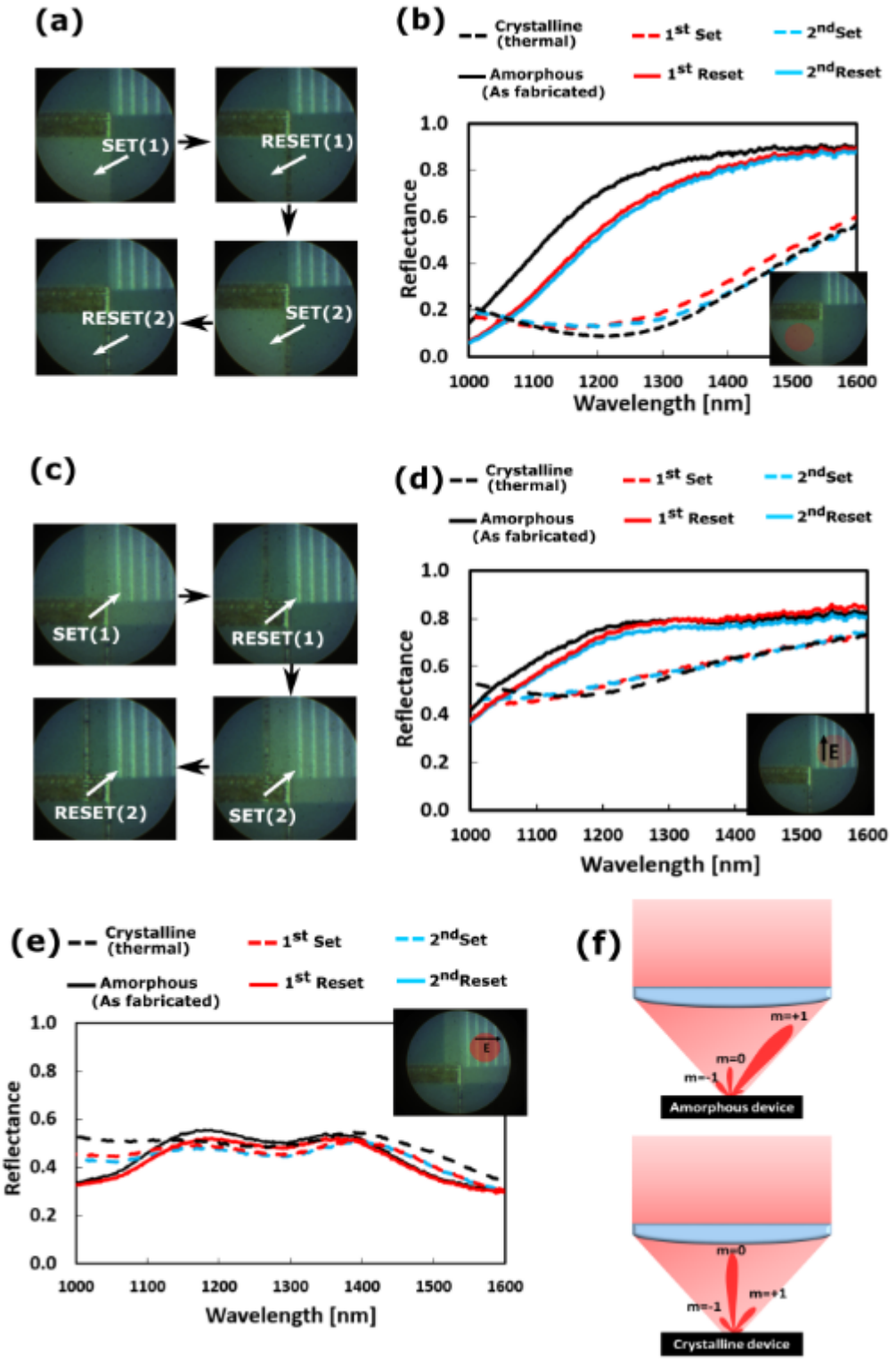

FIGURE 4.10: **(a)** Optically induced phase-change experiments carried out in an unpatterned region of the device. A change in colour can be appreciated after each SET/RESET. **(b)** Experimental reflectance spectra of the unpatterned region after each cycle, compared with fully amorphous (as fabricated) and fully crystalline (thermally crystallised) spectra. **(c)** Optically induced phase-change experiments carried out inside the device. **(d-e)** Experimental reflectance spectra of the device under TE **(d)** and TM **(e)** polarisations, again compared with fully amorphous and fully crystalline states.**(f)** Schematics showing the radiation patterns generated under TM incidence, and collected by the lens in both amorphous (top) and crystalline (bottom) states.

Finally, since aluminum's melting point (660 °C) is relatively close to GST ($\sim$ 600 °C), the device morphology was re-checked via SEM imaging after the laser scans, in order to check if any melting and/or deformation of the Al antenna pattern occured during the GST melt/quench re-amorphisation process. Aluminum antennae of the devices remained intact after several crystallisation and re-amorphisation cycles, as shown in (**Figure 4.11**).

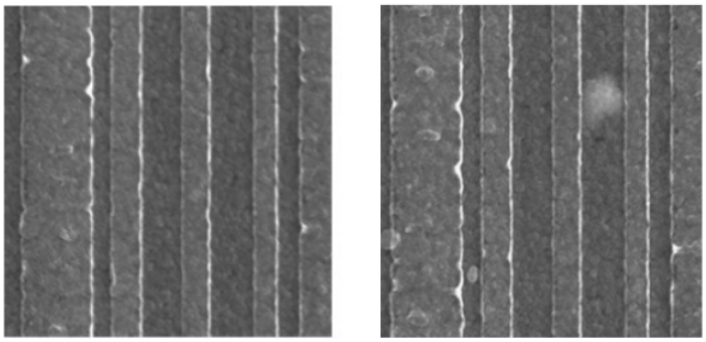

FIGURE 4.11: SEM images of the Al antennas before (left) and after (right) crystallisation and re-amorphisation laser scans. Both scans are approximately 3×3 μm.

4.6 Summary and Conclusions

The primary objective of this section was to provide a demonstration of the capabilities of phase-change metasurfaces towards active wavefront control, as most of the work carried up to now relies on amplitude manipulation. For this purpose, non-mechanical and fully reversible beam steerering devices working in the NIR were developed. This was achieved via successful combination of plasmonic metal/insulator/metal metasurfaces with the worldwide known chalcogenide PCM alloy $Ge_2Sb_2Te_5$. The use of a novel hybridised dielectric spacer which combines SiO_2, GST and ITO ultrathin films was found to be a key point for a successful development of practicable devices, since:

- It allows the location of the GSP resonance in the overcoupled resonant regime, where a near 2π optical phase coverage with superior efficiency is accessible.

- It provides, at the same time, a way to reduce the amount of GST to values closer to what is employed in conventional and well-stablished optical memories, which facilitates re-amorphisation processes and thus device cycling between structural states.

In addition, the GST was encapsulated and thus protected against oxidation, something that is commonly ignored in reconfigurable metasurfaces involving the use of PCMs reported in the literature [39, 48, 64, 159, 196]. The relative simplicity of the presented architecture (based as it is on a MIM resonator type structure which requires for a single lithography step) led to successful and repeatable device realisation using common microfabrication techniques.

Experimental angle-resolved Fourier imaging microspectroscopy along with detailed numerical simulations confirmed that devices reflect an incident NIR optical beam (C-band) in a specular mirror-like fashion when the phase-change layer is in the crystalline state, but reflect anomalously at a pre-designed angle when the phase-change layer is switched into its amorphous state. Experimental results under TM and TE polarisation excitation suggest that additional device features such as active polarising beam splitting could arise from this configuration, thus opening the possibility of developing active metasurfaces with different functionalities employing the same building blocks. Furthermore, reversible switching between states was successfully achieved using optical pulses from an ex-situ laser, something that is rarely seen in phase-change material based reconfigurable metasurfaces reported in the literature, but at the same time is crucial towards their future integration in real-world devices.

In terms of future perspectives, it is expected that the performance and practicability of PCM metasurfaces based on MIM configurations could be further improved via:

- Replacing the GST layer by recently-reported PCM compositions such as $Ge_2Sb_2Se_4Te_1$ (GSST) which have shown lower dielectric losses in both amorphous and crystalline states with even superior optical contrast in the NIR and MWIR [197].

- Employing other metals with less plasmonic losses in the NIR, such as Au or Ag [75]. This should also decrease the risk of geometry deformation during the GST switching processes, since both gold and silver melting points are higher than aluminum (i.e. 1064 °C and 962 °C for Au and Ag respectively). In such a case, special attention should be put to diffusion, as those specific metals exhibit high thermally induced diffusion in GeSbTe-based alloys [74].

Finally, as we will see in the next chapters, following the same design philosophy of keeping the PCM volumes to a minimum, as well as employing other architectures (such as all-dielectric or hybrid metasurface configurations) could potentially result in improved efficiencies, as well as multilevel beam control or additional device functionalities such active optical filters/switches or band structure engineering.

Chapter 5

Reconfigurable dielectric metasurfaces enabled by phase-change materials

5.1 Introduction and motivation

Metal/insulator/metal (or gap surface plasmon) meta-atoms can exhibit beam steering efficiencies up to 80% in the NIR [129], but results from the previous chapter have shown that such values can be reduced to 40% when combined with phase-change materials, mainly due to additional unavoidable dielectric losses present in GeSbTe alloys. While an efficiency of 40% is in fact rather good and could compete with mainstream beam steering devices such as acousto-optic deflectors [198], the use of all-dielectric configurations could potentially improve this value by fully eliminating plasmonic losses coming from metals [88]. Furthermore, additional features such as active optical filtering or switching could emerge from this approach, since dielectric metasurfaces can operate readily in reflection and transmission, and can do this even simultaneously. In fact, very recent work carried out earlier this year by Tian et al.[39] demonstrated the use of GST dielectric metasurfaces for active beam filtering in the MWIR. In that work, directly structured GST dielectric meta-atoms in the form of microcylinders were employed to spectrally shift the characteristic electric and magnetic dipole resonances (via crystallisation of the cylinders) in order to induce broadband changes in the transmittance and reflectance spectra. However, the achieved absolute switching contrasts ($\sim$ 40%) were of the same order of

as achieved by Gholipour et al. in 2013 [70] using plasmonic phase-change meta-atoms in the form of Babinet-inverted SRR (MWIR). This is attributed, in the Tian et al work, to the presence of strong dielectric losses arising from the use of large PCM volumes (up to $\sim 1\mu m^3$ per cylinder) and hence damping (broadening) of the ED and MD resonant modes. As a result, cylinders entirely made of GST clearly hinder the most relevant benefit offered by dielectric metasurfaces, which is the ability to manipulate light efficiently. Furthermore, reversible switching (i.e. crystallisation and re-amorphisation of the devices) was as usual not reported nor justified, and crystalline results were obtained via hot plate annealing of the fabricated devices [39]. That said, the need for novel and smart active metasurface architectures with PCM volumes closer to optical and electrical PCM memory technology (i.e. tens of nm) [78, 143] becomes once again evident.

In this chapter, we propose and experimentally demonstrate a new class of dynamically reconfigurable, fully reversible, and multilevel all-dielectric metasurfaces based on the combination of lossless silicon nanoresonators functionalised with extremely thin (down to $\lambda_0/100$) inclusions of GST. This novel concept was realised via designing, fabricating and experimentally characterizing hybrid Si nanocylinder /$Ge_2Sb_2Te_5$ devices that work at telecoms wavelengths as reconfigurable dual-band (O and C band) to mono-band (C band only) multilevel filters/switches. More specifically, such functionality was achieved by strategic positioning the PCM inclusions at the electric field anti-nodes of a particular mode of the nanoresonator, which allows for selective and continuous switching via gradual re-amorphisation of the PCM layer driven by femtosecond laser pulses. In that way, superior optical performance as well as switching capabilities over multiple cycles was achieved; due to both minimisation of optical losses and GST volumes.

5.2 Design concept and FEM analysis

An illustration of our proposed hybrid dielectric/PCM metasurface working at telecom bands is shown in **Figure 5.1a**. It consists of an array of Si/$Ge_2Sb_2Te_5$ nanodisks arranged in a square lattice on top of a SiO_2 substrate. The choice of $Ge_2Sb_2Te_5$ as

the active material is justified by the fact that, as shown in **Figure 5.1d**, its complex refractive index (when amorphous) matches very well the refractive index of (amorphous) silicon in the target λ = 1300 nm to λ = 1600 nm window. After crystallisation, however, an increase of the refractive index n and absorption coefficient k takes place, with an overall increment of $\Delta n \approx 1.6$ and $\Delta k \approx 1.1$ in the spectral region here of interest [38]. Therefore, the proposed hybrid Si/GST nano-cylinders effectively behave as silicon-only building blocks when the GST is amorphous, but the resonant modes supported by the array (thus its optical response) can be modified on demand by switching the GST layer between its amorphous and crystalline states (**Figure 5.1c**).

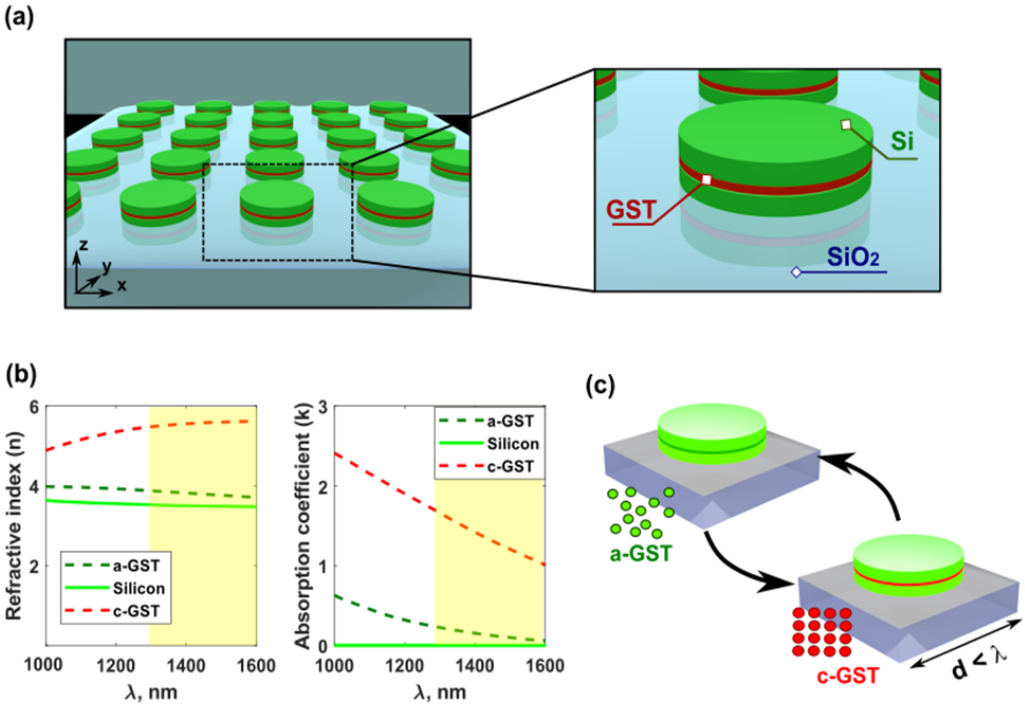

FIGURE 5.1: **(a)**Hybrid dielectric/PCM metasurface concept, here consisting of arrays of Si/GST nano-cylinders on a SiO_2 substrate. **(b)** Refractive index (left) and absorption coefficient (right) of amorphous GST (a-GST), crystalline GST (c-GST) and (amorphous) silicon. The spectral region of interest is highlighted in yellow: in this spectral band, n and k of a-GST and silicon are closely matched. **(c)** Generic scheme of the device working principle: the hybrid Si/GST cylinders effectively behave as Si-only when the GST is amorphous, and the optical response can be disturbed via switching the GST layer between its amorphous and crystalline states.

The expected optical properties of the hybrid nanodisks (shown in **Figure 5.1**) were first studied using the commercial software package COMSOL Multiphysics, described in **section 2.1**. As depicted in **Figure 5.2a**, a generic unit cell consisting of

a tri-layered Si/GST/Si nanodisk on top of a SiO_2 substrate was first employed to analyse the electromagnetic response of the proposed architecture. The GST thickness, t_{gst}, was fixed to have a value of 15 nm, here again to avoid the use of large PCM volumes thus guarantee re-amorphisation while mantaining a decent optical contrast. Since electric dipole (ED) and magnetic dipole (MD) resonances are morphologically dependent [106, 107, 199, 200], the cylinder radii r were varied from r = 140 nm to r = 400 nm in steps of Δr = 5 nm in order to gradually change the aspect ratio ($AR = t_{cyl}/2r$ with t_{cyl} here fixed at 245 nm), and thus investigate its influence on the spectral position of the resonant modes. Following the same approach reported by Staude et al. [106], the lattice constant Λ was varied along with r according to $\Lambda = 2r + 220$ nm. This maintains the array in the sub-wavelength regime (therefore restricting the generation of diffraction orders) while at the same time avoids very small, and hard to fabricate, spacing between the nanocylinders.

The simulated reflectance (R) and transmittance (T) of the device, under normal incidence excitation, are shown in **Figure 5.2b**, for the spectral range 1000 to 1700 nm, as a function of cylinder radius r and with the GST in the amorphous phase. The results reveal the presence of resonant modes associated with both ED and MD resonances, which can initially be identified as an abrupt increase of the reflectance as a function of the cylinder radius, with a corresponding dip in transmittance. An overlap of both electric and magnetic modes takes place at r = 275 nm (λ = 1395 nm), which results in suppression of back scattering (i.e. $R = 0$), with subsequent high optical transmittance. As briefly discussed in Chapter 2, this phenomenon is known as the first Kerker condition [88] and occurs here when the effective electric and magnetic polarisabilities of the nanodisks are in phase and of comparable in strength. It can be also noticed from **Figure 5.2b** that since silicon and amorphous GST (a-GST) are optically similar (i.e. have close matching of their refractive indices in the considered spectral range), the scattering properties of hybrid Si/a-GST nanodisks are, as would be expected, in good agreement with recently published work based on silicon-only nanodisks [106, 107], with the exception of small residual absorption (i.e. $T + R \neq 1$) due to dielectric losses induced by the GST layer. The presence of absorption coming from GST is therefore another major reason for keeping its volume to a minimum.

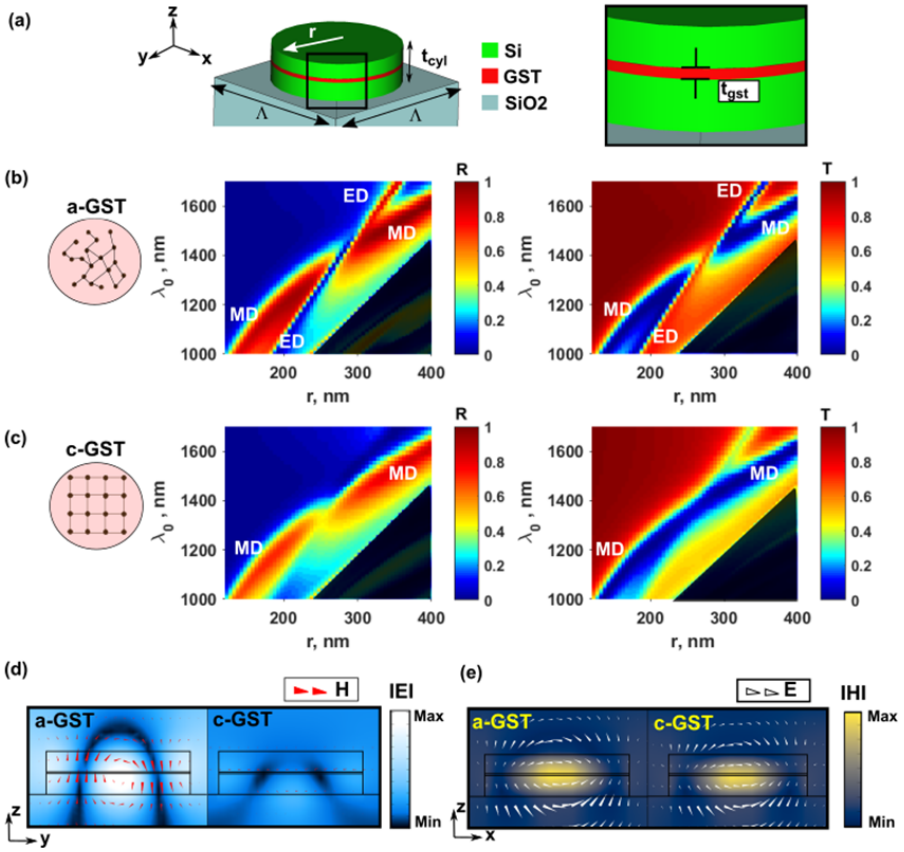

FIGURE 5.2: **(a)** Dimensions and materials of the unit cell employed in our initial FEM analyses, where t_{cyl} = 245 nm, t_{gst} = 15 nm, r = variable, and $\Lambda = 2r + 220$ nm. **(b)** Reflectance R (left) and transmittance T as a function of the cylinder radius r, showing the presence of ED and MD modes when the GST layer is amorphous. Both resonances spectrally overlap at λ = 1395 nm, for a cylinder radius of r = 265 nm, resulting in near-zero backscattering (first Kerker condition). **(c)** Reflectance R (left) and transmittance T (right) after crystallisation of the GST layer. The electric dipole is cancelled in most of the spectral region, with subsequent disruption of the Kerker condition. **(d-e)** Electromagnetic field distribution of the electric **(d)** and magnetic **(e)** resonances for amorphous and crystalline phases of the GST. Note that the 'black' regions in reflection/transmission spectra of **(b)** and **(c)** correspond to the diffractive regime (i.e., where light splits into different diffraction orders).

The above discussed results show that the proposed hybrid Si/PCM configuration offers a flexible designer interface for the realisation of compact and reconfigurable photonics. The location and thickness of the PCM layer within the silicon cylinder body provides additional design degrees of freedom not achievable otherwise (e.g. with cylinders fully made of GST [39]), since separate control of the amplitude and/or spectral position of the ED and MD resonant modes can be realised by placing the PCM layer in the regions where the electric field of each particular mode are strongly confined (in the antinodes of E).

In the next section, we will see both numerically and experimentally that the proposed approach based on the combination of silicon nanocylinders with PCM inclusions can provide for highly flexible, highly efficient and dynamic multilevel control over amplitude and phase of optical wavefronts in reflection and transmission respectively, leading, potentially, to the realisation of a new generation of practicable active photonic meta-devices.

5.3 A dual-to-mono band multilevel meta-switch

To highlight the exciting capability of providing independent control over ED and MD resonances, the design, fabrication and characterisation of devices based on this phenomenon has been carried out. More specifically, devices capable of simultaneous active filtering, switching, and modulation suitable for the O and C telecommunications bands (1320 nm and 1550 nm respectively) were developed. They consist of square arrays of low aspect-ratio hybrid Si/GST nanodisks, which allows for a spectral splitting of the electric and magnetic dipole resonances (as shown in **Figure 5.1b**). This creates a dual-band filter when the GST layer is in the amorphous state, but leads to a mono-band filter when the GST layer is crystallised (due to selective suppression of the ED mode located at the C-band). A schematic of the unit cell is depicted in **Figure5.3a**, where Λ = 850 nm, t_{cyl} = 195 nm, and r = 666 nm. The GST layer is placed in the middle of the nanodisk and has a thickness of t_{gst} = 15 nm. The simulated transmittance, reflectance and absorbance spectra at normal incidence and for the GST layer in its amorphous and crystalline states, are depicted in **Figure 5.3c to d** respectively. Results reveal that with the GST in its amorphous phase (green lines), the device shows ED and MD resonant peaks located at the required O and C bands, with very high device reflectances (and 0% transmittance) of 93% and 80% at λ = 1320 nm and λ = 1550 nm respectively. However, as desired, crystallisation of the GST layer shifts and damps the ED resonance (due to the increased value of n and k for crystalline GST), thus light is transmitted instead with an amplitude of 65%. On the other hand, the MD spectral position remains nearly unaffected. This, essentially, leads to switching from a dual-band to mono-band filtering by the device. The absolute modulation depth, *MDR*, in reflection (*MDR* =

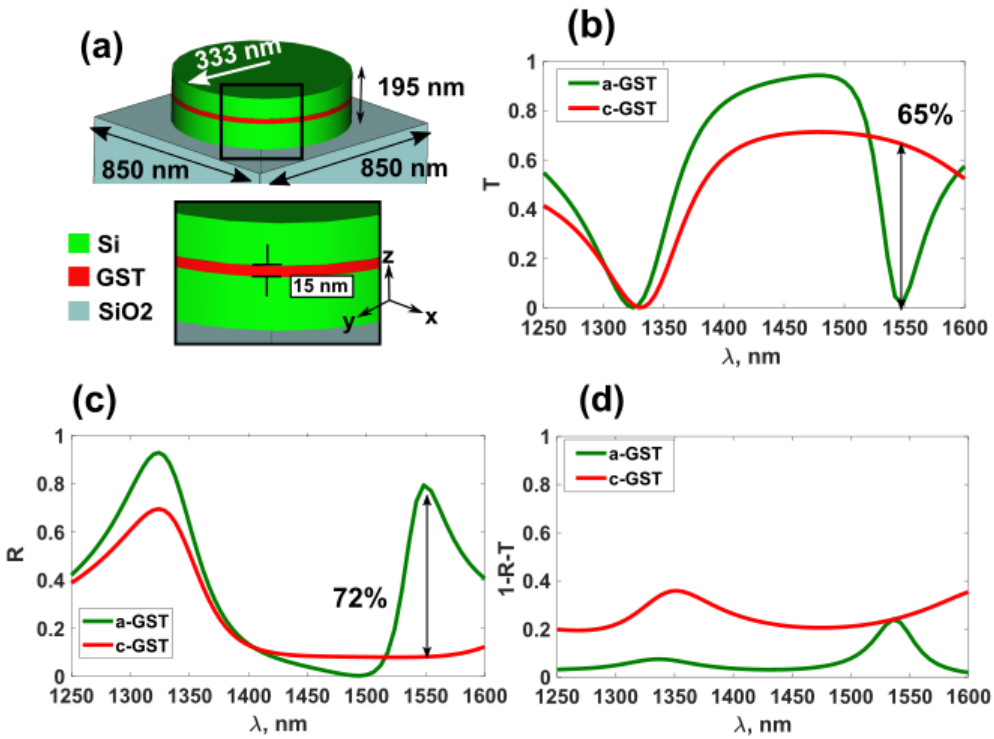

FIGURE 5.3: Summary of the dual-to-monoband Si/GST based meta-switch. **(a)** Schematics and dimensions of the proposed hybrid Si/GST meta-device unit cell. **(b-d)** Numerically obtained transmittance **(b)**, reflectance **(c)** and absorbance **(d)** spectra at normal incidence for a-GST and c-GST.

R_{am} - R_{cr}) is 72% at λ = 1550 nm, with a modulation depth intransmission at the same wavelength of $MDT = T_{am} - T_{cr}$ = 65%. The small amount of energy missing is absorbed as dielectric losses by the thin GST layer as plotted in **Figure 5.3d**

Recently, all-dielectric metasurfaces have been proven to be highly dispersive and thus sensitive to oblique incidence [201] compared to plasmonic metasurfaces [202]. Therefore, the device robustness at oblique incidence was also investigated. For this purpose, the reflectance spectra were calculated for a range of angles of incidence θ_i going from -15° to 15° in steps of $\Delta\theta_i$ = 0.5° for both TE and TM polarisation states.

Figures 5.4a and **5.4b** show the angular dependence of the reflectance spectra under TM excitation for a-GST and c-GST respectively. It can be seen from **Figures 5.4a** that the mode associated with the ED resonance of the disk is dispersionless (i.e. remains in the same spectral position when varying θ_i), whereas the MD associated mode for non-zero angles of incidence splits into two separate leaky Bloch

modes with high dispersion and opposite sign of group velocity due to coupling between the disks, as shown in **Figures 5.4e-g**. Here, the y-component of the magnetic field (H_y) is plotted in the colorbar, and black arrows represent the Poynting vector which confirms the presence of energy transport in the x-axis at oblique incidence (**Figures 5.4e** and **5.4g**). On the other hand, non-propagative standing waves were identified at normal incidence (**Figure 5.4f**). Crystallisation of the GST layer results, as expected, in the cancellation of ED mode for every angle of incidence, while the splitting of MD mode is conserved.

For TE-polarised excitation (see **Figures 5.4c** and **5.4d** for a-GST and c-GST cases, respectively), both ED and MD associated modes remain unaffected by the oblique incidence while maintaining the characteristic cancellation of the ED mode after GST crystallisation. These results suggest that the proposed PCM/silicon metasurface configuration offers additional potential such as reconfigurable band-structure engineering.

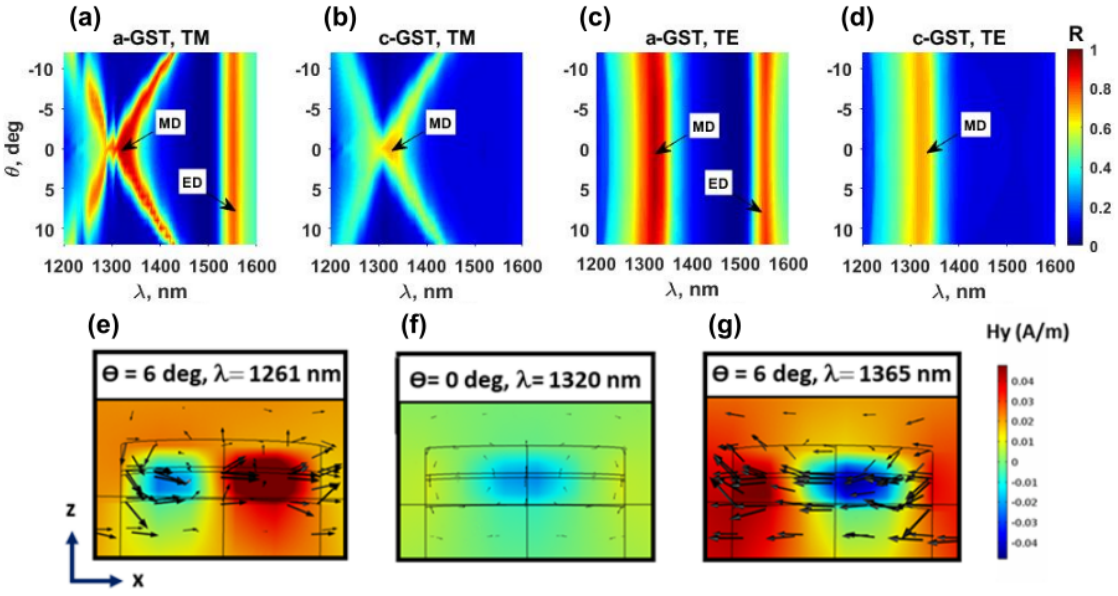

FIGURE 5.4: Angular reflectance under TM polarisation for **(a)** amorphous and **(b)** crystalline states, showing splitting of the MD with angle of incidence, and cancellation of the ED in the crystalline phase. **(c-d)** Angular reflectance under TE polarisation for **(c)** amorphous and **(d)** crystalline states, showing a dispersionless behavior of the MD, and cancellation of the ED in the crystalline phase. **(e-g)**Distribution of the Magnetic field y-component (colorbar) under different excitation conditions. The presence of leaky Bloch modes is confirmed by the Poynting vector (black arrows), which shows energy transport in opposite directions at oblique incidence (here 6 deg, λ_0= 1261 nm and λ_0 = 1365 nm), and a standing wave at normal incidence (λ_0 = 1320 nm).

5.3.1 Fabrication of all-dielectric GST/Silicon nanocylinders

Devices discussed in the previous sections were fabricated over areas of 100 μm$\times$100 μm on 1 cm$\times$1 cm SiO_2 substrates previously cleaned with acetone and rinsed in isopropyl alcohol. Magnetron thin film sputter deposition, e-beam lithography and etching techniques were employed for the process, as described in **section 3.2.** Fabrication steps are illustrated in **Figure 5.5** and detailed below:

- First, a silicon/GST/silicon tri-layer stack was deposited using a magnetron sputtering system (Nordiko). RF sputtering in an argon atmosphere (50 sccm) with a plasma power of 200 W was used to deposit the top and bottom silicon layers. DC sputtering was employed for the GST deposition, under the same atmosphere with a plasma power of 20 W. The chamber pressure and base vacuum for both processes were 8.5×10^{-2} Pa and 1.0×10^{-5} Pa respectively (**Figure 5.5a-b**).

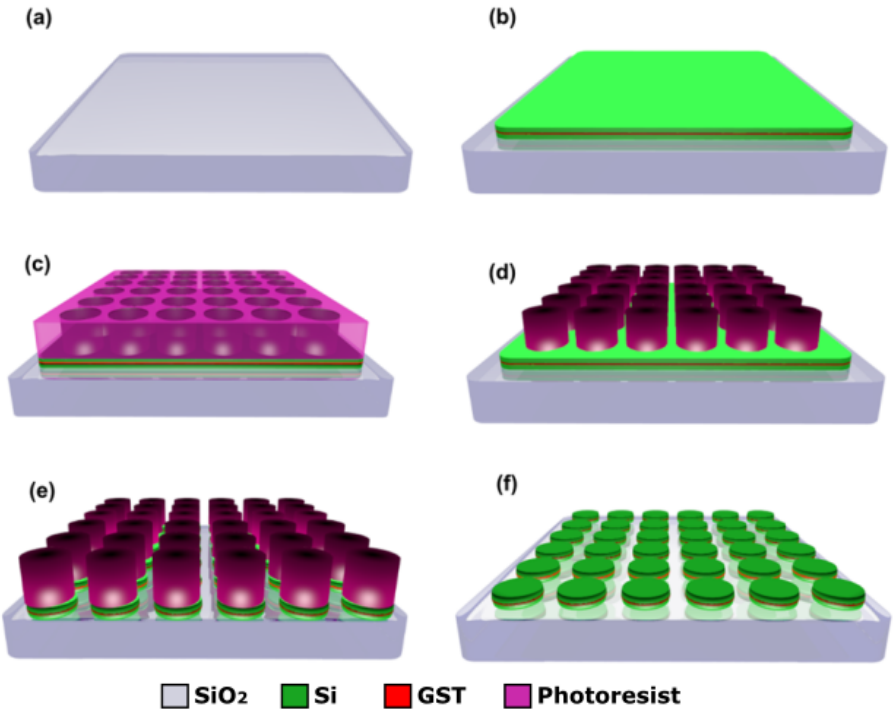

FIGURE 5.5: Flowchart describing the fabrication process of active dual-to-mono band phase-change metasurfaces. **(a)** Substrate cleaning. **(b)** Deposition of silicon, GST and silicon layers. **(c)** Spin coating of the adhesion layer, negative photoresist and conductive layer with subsequent e-beam exposure. **(d)** Development of the pattern. **(e)** Reactive ion etching. **(f)** Photoresist removal.

- Next, the samples were covered with an adhesion layer (Ti-Prime) using a spinner at 4000 rpm for 20 s, with subsequent post-baking at 90 C for 5 min. A negative resist (ma-N 2403) was then spin-coated at 2500 rpm for 60 s and post-baked at 90 °C for 10 min. Finally, a thin layer of conductive resist (Electra) was spun to ease the charge dissipation during e-beam lithography (2500 rpm for 50 s, post-baking at 90 °C for 2 min).

- The required array pattern was then transferred to the resist via e-beam lithography, and subsequent development in MF-319 solution for 45 s was carried out in order to remove the unexposed areas. After lithography, the sample was post-baked at 90 °C for 5 min to increase the hardness of the remaining exposed areas (**Figure 5.5c-d**).

- Finally, the samples were etched in a $CHF_3/SF_6/O_2$ plasma mixture using an inductively coupled plasma reactive ion etching (ICP-RIE) system. ICP (300 W) was used to create high-density plasma which was then accelerated towards the sample by the RIE (200 W) component to achieve directional etching (**Figure 5.5e**).

- The remaining photoresist (after the RIE process) was removed via soft sonication in warm acetone (**Figure 5.5f**).

SEM pictures of some of the fabricated devices are shown in **Figure 5.6**, with measured nanodisk diameters of 668 nm, extremely close (in fact within measurement error) of the target design diameter of 666 nm.

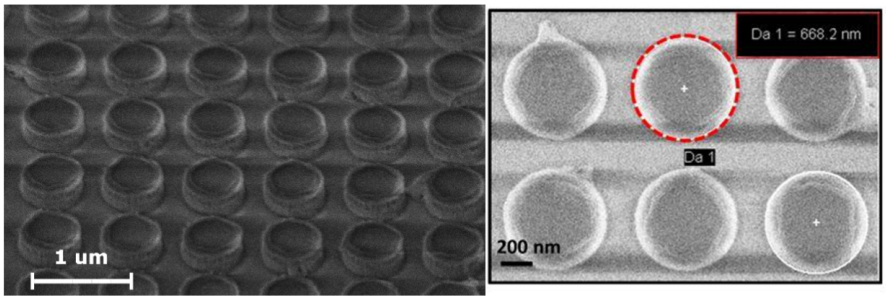

FIGURE 5.6: SEM images of the as-fabricated GST/silicon nanocylinders showing measured radii values of $\sim$ 668 nm.

5.3.2 Optical characterisation

The devices were optically characterised in collaboration with Ivan Sinev from ITMO university, employing a NIR Fourier imaging spectroscopy to obtain the experimental reflectance spectra. Results, for normal incidence, **Figure 5.7a** shows excellent agreement with numerical simulations. That is, for a-GST (green curves), a reflectance peak of 79% corresponding to the electric dipole resonance is clearly observed at λ = 1540 nm (*cf.* 80% at λ = 1550 nm from COMSOL simulations). The second reflectance peak corresponding to the magnetic dipole mode is located experimentally at a shorter wavelength of λ = 1380 nm, with a strength of R = 83% (slightly red-shifted *cf.* numerically-obtained results, where λ = 1320 nm and R = 93%; but again in very good agreement). The reflectance spectrum taken after crystallisation (made here via hot plate annealing for a first proof of concept, but reversible switching via laser scans is shown in the next section) confirms the predicted shift of ED peak at λ = 1540 nm, with the MD nearly unaffected by the phase transition. An absolute experimental contrast (modulation depth) between phases of 70% was obtained at λ = 1540 nm, very close to that predicted by our numerical models (i.e., 72% at λ = 1550 nm). Presence of noise in the measurements is due to a low signal-to-noise ratio originated by the laser operating at very low powers to ensure that the GST layer didn't crystallise during the measurements. The optical performance of our hybrid metasurfaces at oblique incidence was also experimentally investigated, under both TE and TM incidence, and compared to numerically obtained results. Thus, **Figures 5.7b** to **5.7e** show the experimentally measured reflectance spectra as a function of the angle of incidence under both TM and TE polarisation (top) plotted against simulations for reference. It can be noted that:

- Under TM polarisation, as expected, ED and MD resonances are excited when the GST layer is amorphous (**Figure 5.7b**), with the numerically-predicted splitting with angle of incidence of the MD mode and subsequent cancellation of the ED mode upon GST crystallisation. (**Figure 5.7b**)

- Under TE illumination, the as-fabricated metasurfaces (**Figures 5.7d** and **5.7e**) show robustness at oblique incidence (i.e. ED and MD reflection peaks remain in the same spectral position at every angle), and the ED resonance at 1550 nm

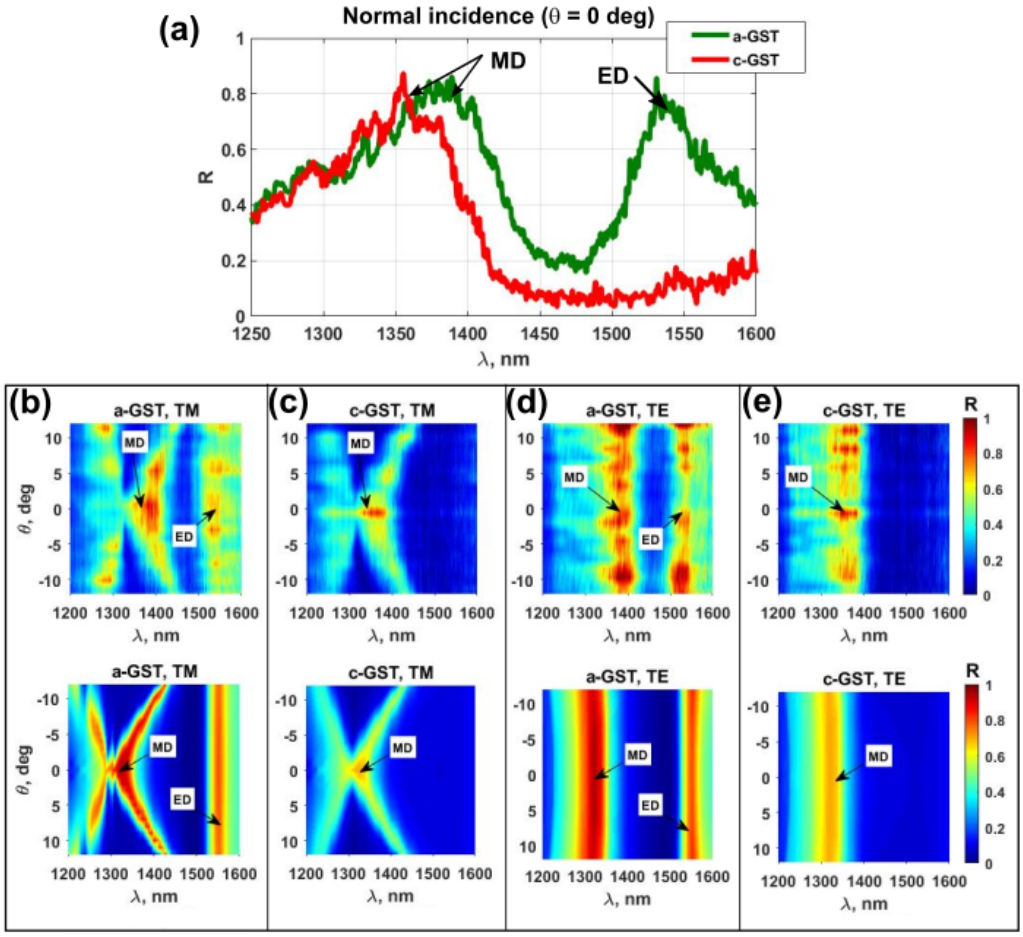

FIGURE 5.7: **(a)** Experimentally obtained reflectance spectra at normal incidence for amorphous (green) and crystalline (red) states. **(b-e)** Experimental angular reflectance spectra (top) compared to simulations (bottom): **(b-c)** Under TM excitation when the GST is **(b)** amorphous and **(c)** crystalline. **(d-e)** Under TE excitation for **(d)** amorphous and **(e)** crystalline GST.

is again completely suppressed for the c-GST phase over the entire range of incident angles measured.

For additional information, the reflectance spectra were also taken employing conventional microspectroscopy (i.e. where measurements are performed in the real image plane as described in section 3.3.2) using a JASCO-MSV spectrometer with a focusing/collection objective lens of NA 0.25 (i.e. with excitation and collection angles of $\sim \pm 15\,^{\circ}$). Results for amorphous and crystalline states are shown in **Figure 5.8**. Here, the influence of the angle of incidence over the optical response becomes even more evident, since:

- Due to the highly dispersive nature of the MD, in the amorphous phase (green

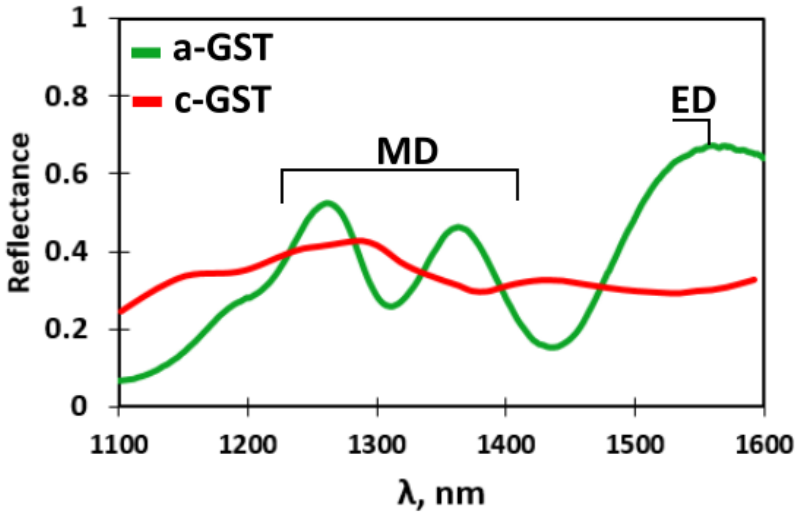

FIGURE 5.8: Reflectance spectra of the hybrid silicon/GST nanocylinders taken with conventional microspectroscopy.

curve) the resonance seems to be split in two peaks corresponding to the smaller and larger wavelength branches of the MD due to an averaging of the signal coming from excitation and collection at different angles simultaneously. On the other hand, the dispersionless nature of ED results in an homogeneous reflectance peak.

- After crystallisation, the absence of ED is confirmed (red curves), with the two branches of MD being slightly damped due to an increase of the losses in crystalline GST.

5.3.3 Multilevel, optically induced, reversible switching

Optical switching experiments were carried out using a femtosecond laser source (Yb^{3+} Avesta TEMA-150, central wavelength 1050 nm, pulse duration 150 fs), in collaboration with ITMO university in St. Petersburg. Note that at the wavelength used, the losses of both amorphous and crystalline GST are high while the absorption in silicon is negligible [203], which ensures very effective heating of GST inclusions since no energy is dissipated in the surrouding materials. To facilitate fast switching of large areas of the metasurface, the laser was focused on the sample with a 5 cm achromatic doublet lens that provided smooth laser intensity profile in the focal plane (with a laser spot FWHM of approximately 15 μm). The sample was

then scanned with respect to the laser beam to achieve switching of even larger areas of the metasurface. For these studies, the fabricated cylinders radii were slightly decreased to $\sim$ 311 nm (instead of 333 nm) in order to blue shift the overall optical response, thus be able to capture the red shift of ED peak upon crystallisation with the spectrometer detector (InGaAs CCD, up to 1650 nm). Fourier spectroscopy was performed to obtain the reflecance spectra at normal incidence after each laser scan.

Crystallisation laser scans were performed in the multi-pulse regime (80 MHz repetition rate) excitation with a fluence of 1.28 mJ/cm^2. Multilevel switching from crystalline GST back to amorphous GST were carried out in the quasi single-pulse regime (20 Hz repetition rate) with fluences linearly increasing from 6.4 up to 19.2 mJ/cm^2; in steps of 2.7 mJ/cm^2. **Figure 5.9a** shows results over an entire switching cycle, consisting of 1 crystallisation laser scan and 6 partial re-amorphisation scans (thus 7 tunable levels in total). A strong red shift and damping of the ED after crystallisation (scan 1) can be observed, followed up by its restoration and blue-shift as the GST layer is gradually re-amorphised (scans 2 to 7). These behavior leads to the possibility of fine control over the spectral amplitude of the metasurface resonance.

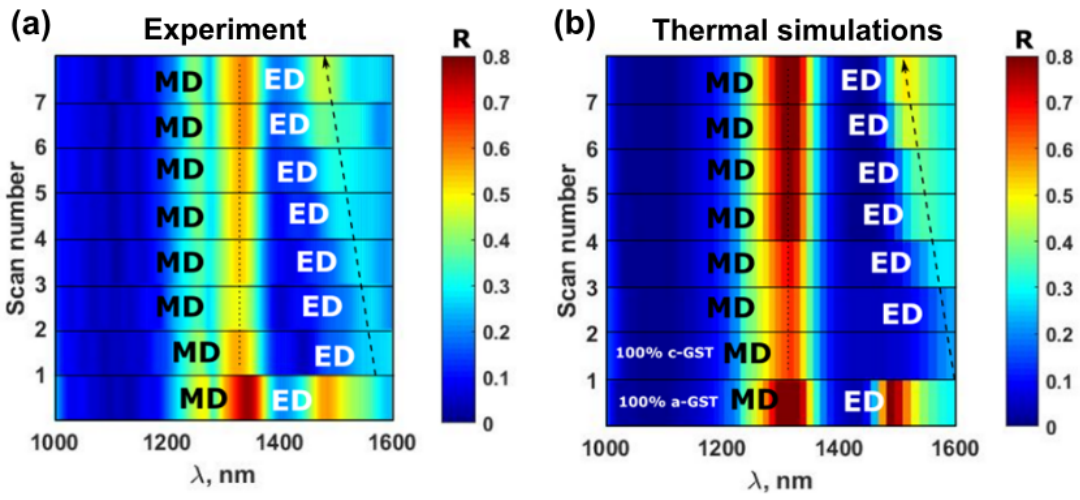

FIGURE 5.9: **(a)** Reflectance measurements of the hybrid silicon/GST nanocylinders performed after each laser scan via Fourier imaging spectroscopy. **(b)** Reflectance spectra after thermal simulations (described in detail in **section 5.3.4**).

Figure 5.9b shows the numerically obtained results after thermal FEM simulations, revealing a fairly good agreement with respect to what was obtained experimentally (i.e. an abrupt red shift of ED upon crystallisation, followed up by gradual blue shifts at each re-amorphisation step). Analyses from thermal simulations

(discussed in detail in the next section) suggested that the multilevel tuning was achieved by redistribution of the hot-spots (electric field maxima) across the GST layer at the laser pump wavelength, which results in different regions of the GST layer being re-amorphised after each scan.

Finally, the repeatability of the multilevel switching process was demonstrated via replication of the above switching experiments for various cycles over the same sample. **Figure 5.10** shows results of crystallisation and multilevel re-amorphisation over 8 cycles (one cycle per horizontal sub-panel). As expected, again the spectral position of the ED is blue shifted and becomes stronger after each fs pulse, due to an increase of the amount of amorphous GST inside the nanodisk, whereas the spectral position of the MD remains unaffected. Note that here there is a more obvious splitting of the MD at λ = 1370 nm and λ = 1240 nm respectively (compared to measurements shown in **Figure 5.9a**, which were performed with Fourier imaging spectroscopy) since conventional microspectroscopy measurements were employed here to speed up the experiment (each Fourier spectroscopy measurement takes around 1 hour). Note that in cycle 4, 11 levels (instead of 7) were demonstrated via linear scaling of the fluence up to 22.2 mJ/cm^2. Importantly, no structural damage was

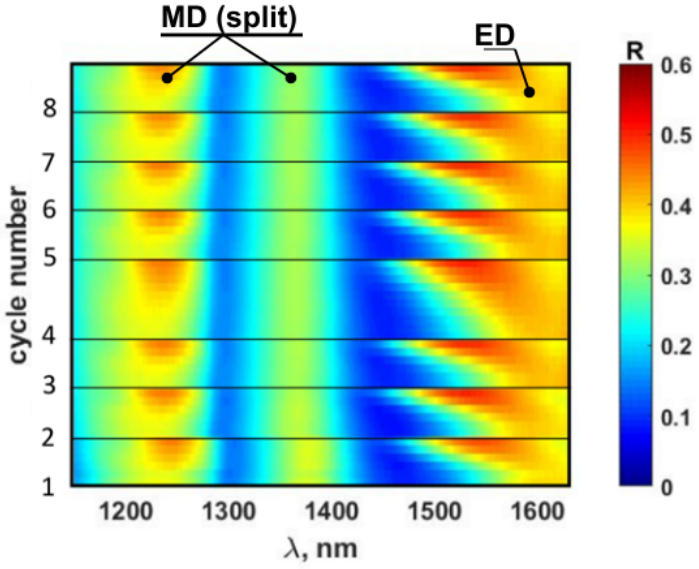

FIGURE 5.10: Variation of the reflectance spectra over a total of 8 switching cycles. Every cycle consisted of several re-amorphisations of the metasurface and a single crystallisation.

observed during the switching process, which suggests that the developed architecture provides a robust and potentially attractive platform for real world applications. **Figure 5.11a** and **5.11b** show SEM images of the cylinders before and after laser scans respectively, with no signs of geometry deformation. Structural damage

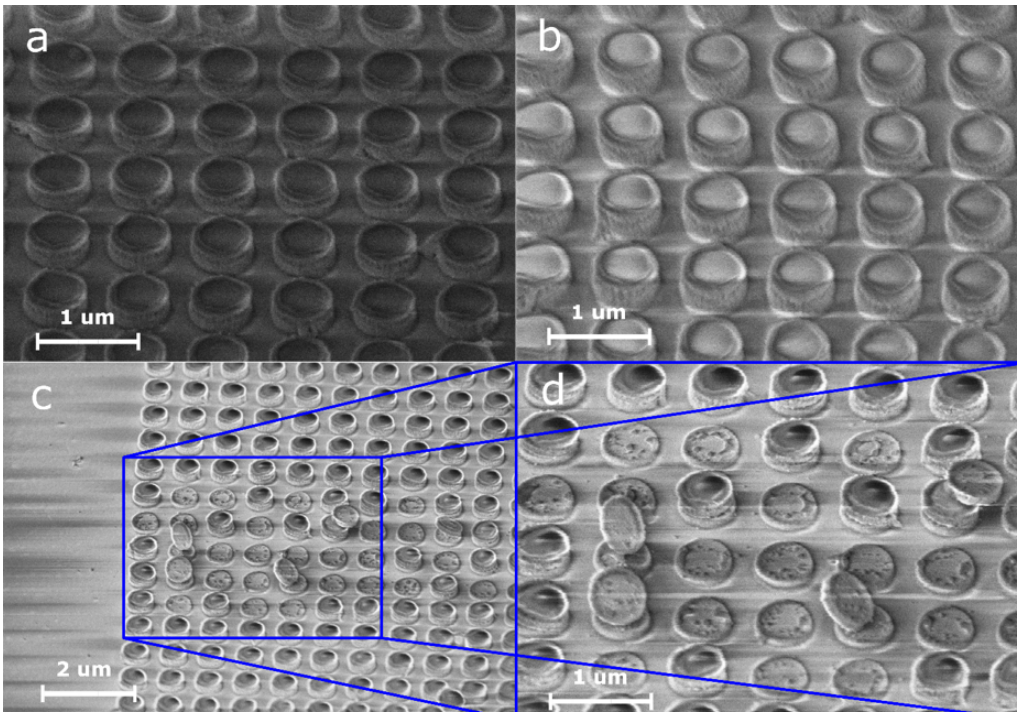

FIGURE 5.11: **(a-b)** SEM images of the devices before **(a)** and after **(b)** laser scans. **(c-d)** SEM images after damaging the sample via directly exposing it to laser fluences above 20 mJ/cm^2.

was only observed when the fully crystalline arrays were directly exposed to high fluences above 20 mJ/cm^2 (i.e. without passing through previous re-amorphisation steps employing linearly increasing power fluences). **Figures 5.11c-d** show 2 SEM images of the sample after being exposed to such high powers, where some cylinders are "cut in half" possibly due to disintegration of the central GST layer.

5.3.4 Thermal analysis of optically induced multilevel switching

For a better insight to the multilevel switching, thermal simulations of the hybrid Si/GST cylinders subject to laser excitation were carried out employing the heat transfer in solids COMSOL module linked to the RF module (as described in section 3.1.2, Chapter 3) .

Figure 5.12 shows a schematic flowchart of the simulation steps followed to reproduce the experimental results from laser scans, shown in **Figure 5.9b**. First, the crystalline GST nanodisk was excited with a laser pulse (λ = 1050 nm) having the same fluence employed in the experiment, with the purpose of extracting a power loss density map inside the GST layer. Volumetric losses were then used as a heat source to calculate the temperature distribution and subsequent cooling rates. Molten GST was assumed over regions of the temperature map where T > 630 °C (10 °C above the melting point of GST according to e.g. [204]). Re-amorphisation was considered if the cooling rates T_{rate} were faster than 20 °C/ns. Cooling rates were found to be significantly quicker than that (thus beneficial for the re-amorphisation process); always above 50 °C/ns for all the laser scans. This can be attributed to the metasurface design itself, as well as the judicious choice of the wavelength employed for the laser scans, since:

- Small volumes of GST, comparable to what is used in current PCM memory technologies were employed.
- The GST layers were embedded in the body of Si cylinders having better thermal conductivity; which helps the heat to flow away quicker.
- Silicon has no optical losses at λ = 1050 nm, whereas GST is highly absorbing, thus heat was found to be well-localised in the region of interest.

The last simulation step consisted of re-amorphised bits being included as new amorphous domains in the electromagnetic model to re-calculate both the reflectance spectrum after laser exposure, and the next power loss density map for the next laser scan. The iterative process was then repeated for the remaining pulses (i.e. 6 pulses in total with linear increments of 2.7 mJ/cm^2, with the first re-amorphisation pulse having a fluence of 6.4 mJ/cm^2). Reflectance spectra after each pulse were then compared to experimental data as depicted in **Figure 5.9** of the previous section.

For more clarity, **Figures 5.13a** and **5.13b** show the temperature evolution, after the fs pulse ends, with a cross section of the GST layer at 3 different times, $t = 0$ *ns*, $t = 0.2$ *ns* and $t = 1$ *ns* (**Figure 5.13b**). Regions above the melting temperature (T_{melt} = 630 °C) can be clearly identified as hot spots after the pulse ceases (at $t = 0$ *ns*) coming

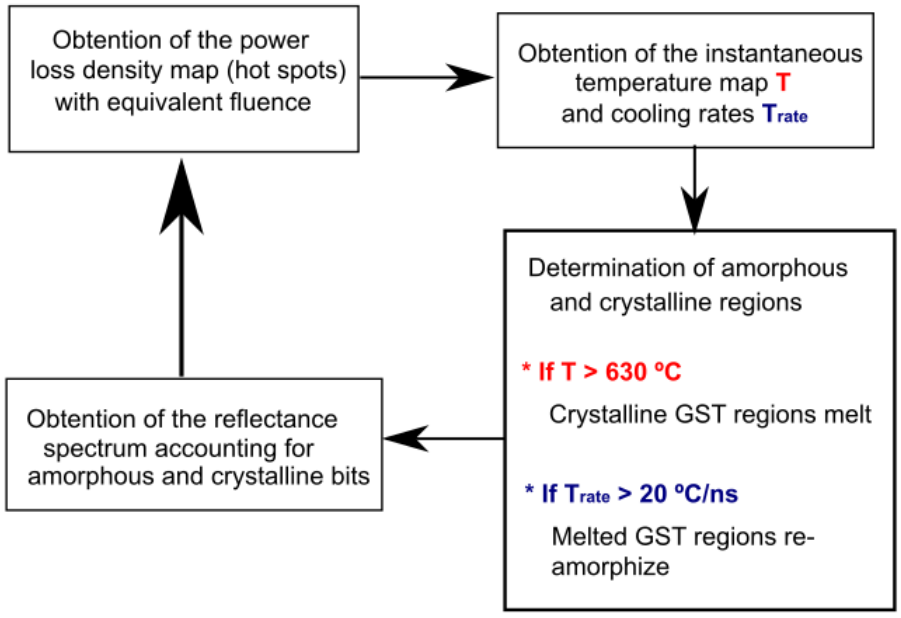

FIGURE 5.12: Flowchart describing the electromagnetic/thermal model employed for numerical replication of the experimental multilevel switching process.

from the strong field confinement inside the cylinders, with the temperature falling below 100 °C after just 1 ns, which clearly confirms re-amorphisation of the molten regions. Finally, **Figure 5.13c** shows the evolution of the crystalline and amorphous GST bits mapped through thermal simulations during the different fs pulses, and employed for re-calculation of the reflectance spectra a posteriori.

5.4 Metasurface additional potential and scalability

The multilevel amplitude control capabilities of all-dielectric silicon metasurfaces functionalised with embedded PCM inclusions demonstrated in this chapter could give rise to additional device functionalities, such as continuous optical phase control. This can be achieved via optimisation of the structure to operate under the first Kerker condition, where a 2π phase coverage is accessible with high transmission coefficients [106, 107]. Local phase control could induced in a fixed-cylinder geometry, potentially in the same way demonstrated in the previous sections: i.e. via changing the fraction of crystallisation of individual cylinders (similar to liquid-crystal-on-silicon spatial light modulators, where optical phase control is achieved pixel by pixel via changing the refractive index of liquid crystals [205]). In addition,

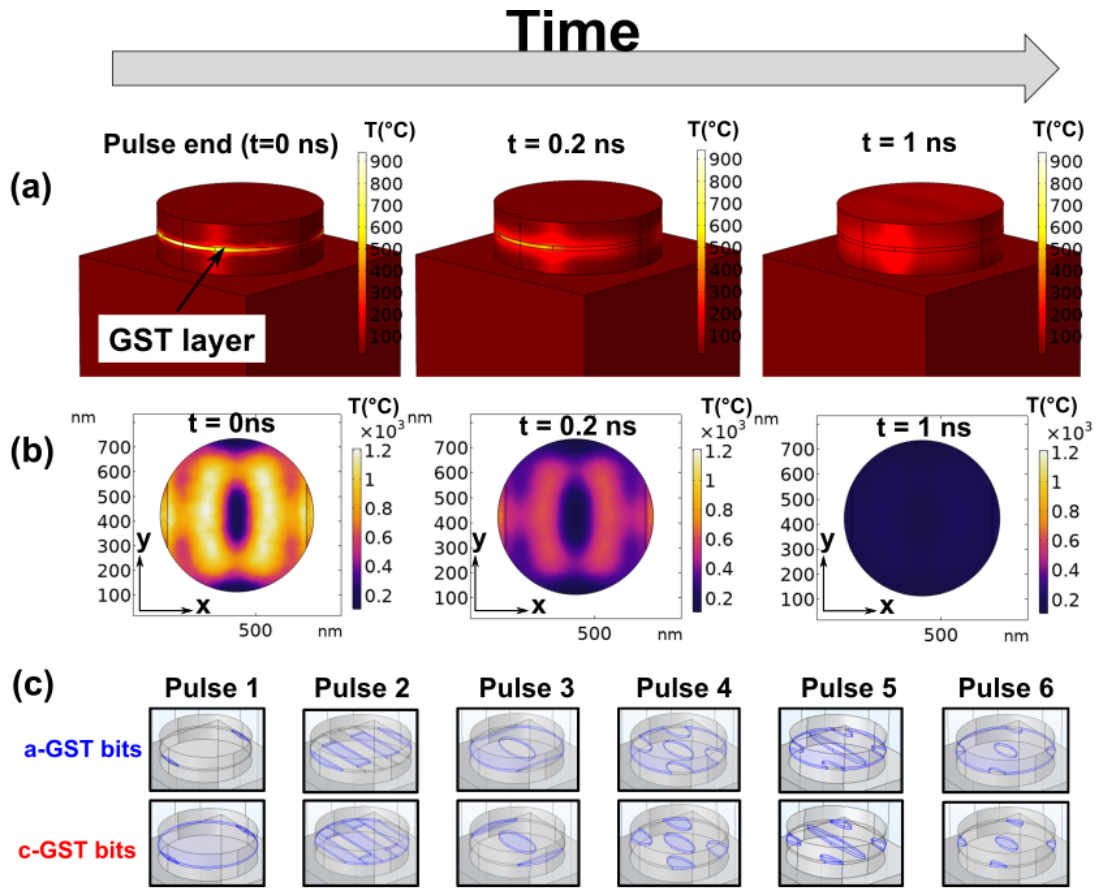

FIGURE 5.13: **(a)** Temperature evolution of a single cylinder after laser exposure (here for scan number 2, fluence 9.1 mJ/cm^2) **(b)** Cross section of the GST layer under the same conditions described in **(a)**, where molten and re-amorphised regions can be clearly identified at t = 0 and t = ns respectively. **(c)** Spatial distribution of crystalline and amorphous GST bits obtained after each scan, and used to compute the multilevel reflectance spectra.

by an appropriate combination of materials, the same design concept could be re-scaled to operate at other spectral bands where most of available liquid crystals fail due to optical absorption (such as the MWIR) [206], as it will be shown via simulations in what follows.

The unit cell employed in this study is depicted in **Figure 5.14a**. Here, a layer of the recently synthesised PCM $Ge_2Sb_2Se_4Te_1$ (GSST) [197] is embedded inside the body of a silicon cylinder. Such composition was chosen for being more suitable for optical phase control, due to its negligible optical losses in the MWIR compared to GST (refractive indices and absorption coefficients of both compositions are shown in **Figure 5.14b** for comparison). In addition, contrary to GST in the MWIR, the refractive index of a-GSST is closely matched with silicon in such spectral range

(**Figure 5.14b** left). The entire structure is embedded in an Al_2O_3 matrix, since reducing the refractive index contrast between high index cylinders and their surrounding medium has been proven to increase the bandwidth of the Kerker condition, thus resulting in more light being phase-shifted and transmitted through the structure [107]. The cylinder radius r, period Λ and thickness t_{cyl} were used as variables to maximise both the amount of phase coverage and amplitude in transmission upon gradual crystallisation of the PCM layer. Refractive indices of intermediate crystalline states were calculated employing an effective medium approximation, particularly the Landau-Lifshitz-Looyenga model [207]. The position of the GSST inclusions within the cylinder body, as well as its thickness t_{GSST} were also varied during the process.

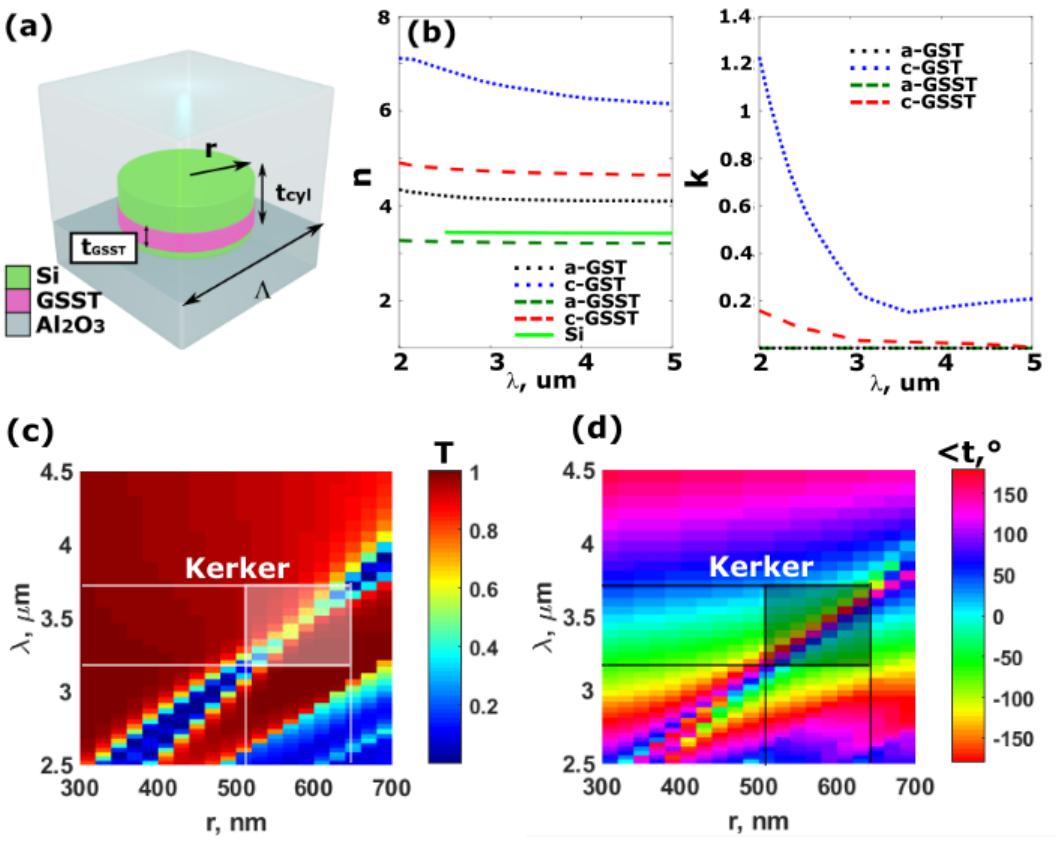

FIGURE 5.14: **(a)** Schematics of the unit cell employed for active optical phase control in the mid infrared. **(b)** Refractive index and absorption coefficient of amorphous/crystalline GST [197], Silicon [208], and amorphous/crystalline GSST [197], **(c-d)** Transmittance **(c)** and phase **(d)** in transmission as a function of the cylinder radius.

The first Kerker condition employing the above-described structure was confirmed via numerical simulations in the spectral region of $\lambda = 3.25\ \mu$m to $\lambda = 3.75\ \mu$m,

where both high transmission (**Figure 5.14c**) and a 2π optical phase control (**Figure 5.14d**) can be achieved via variation of the cylinder radius from r = 500 nm to r = 650 nm. The total cylinder thickness was t_{cyl} = 547 nm , with a 30 nm thick GSST layer located in the center. The amount of optical phase coverage and efficiency in transmission as a function of the crystalline fraction of GSST were then investigated at the central wavelength of the Kerker regime (i.e. $\lambda = 3.4\ \mu$m) for various GSST thicknesses (t_{GSST} = 30 nm, t_{GSST} = 220 nm, and t_{GSST} = 350 nm). As revealed by **Figure 5.15a**, using 30 nm results in a total phase coverage of $\sim 100\ ^\circ$ when changing from fully amorphous to fully crystalline (with efficiencies in transmission above 80%) , which is insufficient for most applications based on active wavefront shaping. This was found to be due to:

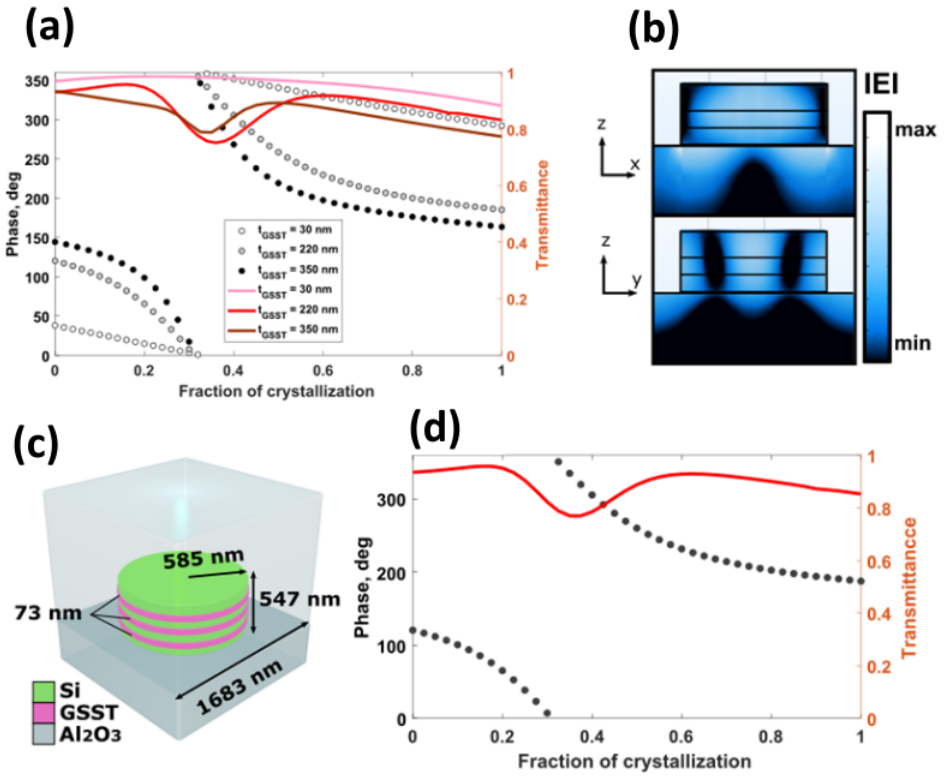

FIGURE 5.15: **(a)** Optical phase and transmittance variation as a function of the GSST layer thickness t_{GSST}. **(b)** Electric field distribution in the zx and zy planes when the cylinder is operating under the Kerker condition. **(c)** Multilayer GSST design equivalent to a single 220 nm thick GSST layer. **(d)** Phase and transmittance as a function of the crystallisation fraction for the design shown in **(c)**, with a total phase coverage of 300 ° and a minimum efficiency of 75%.

- First, the homogeneous nature of the electric field distribution (shown in **Figure 5.15b**), which is now not well-concentrated in the center of the structure

and occupies the whole cylinder volume instead

- Second, a reduced refractive index contrast between amorphous and crystalline GSST with respect to GST, as shown in **Figure 5.14b**.

Therefore, by gradually increasing the amount of active material, 300° and a full 360 ° phase coverage with mininum transmission efficiencies above 75% were obtained for t_{GSST} = 220 nm and t_{GSST} = 350 nm respectively. Such phase coverages are much better for flexible and active wavefront control [6], but results in the use of high PCM volumes which could potentially become difficult (or even impossible) to re-amorphise due to thermal insulation. An alternative to this could be splitting the large PCM volume into several thin layers to ease heat dissipation through the intermediate silicon layers. For example, in **Figures 5.15c** and **5.15d** it is shown how by splitting the 220 nm thick GSST layer into 3 thin layers (73 nm each), the same optical performance (i.e. 300° of optical phase span) can be achieved.

5.5 Summary and conclusions

We have introduced and experimentally validated a new practicable metasurface architecture based on a hybrid combination of high-index dielectric building blocks with embedded inclusions of chalcogenide phase-change materials.

Taking advantage of the strong localisation of the electric fields inside the cylinders, as well as of the characteristic complementary spatial field distribution of ED and MD resonances, attractive new phenomena (otherwise not possible) such as individual tuning of ED resonances have been demonstrated. Particularly, this was achieved in the NIR by employing arrays of low aspect ratio silicon nanocylinders functionalised with ultra-thin ($\lambda/100$) GST thin films within the silicon body, where the PCM is located only where it is really needed (i.e. the electric field antinodes of the ED mode). As a result of such configuration, ED resonances can be tuned to selectively switch a specific spectral band (here λ = 1550 nm) to be either reflected or transmitted by the device, via changing the PCM between amorphous and crystalline states respectively. On the other hand, the reflectance peak associated with

MD (λ = 1320 nm) remains nearly unaffected by the phase transition due to only minor interactions of the electric fields with the phase-change layer. Employing only 15 nm of GST, absolute modulation depths of the ED above 70% in reflection have been experimentally confirmed; with numerically estimated modulation depths of >60% in transmission ($\sim$ 50% better than what was achieved with cylinders fully made of PCMs operating in the MWIR, where dielectric losses of GST are even lower than in the NIR [39]).

More importantly, as in the case of plasmonic beam steerers reported in **Chapter 4**, reducing the GST volumes to a level comparable to what is used in PCM memories enabled successful reversible switching processes, as demonstrated by the first ever (so far we know) experimental reversiible **and** multilevel switching in phase-change metasurfaces. Crystallisation and re-amorphisation experiments were carried out employing fs laser scans, where up to 11 tunability levels have been demonstrated. No structural damage of the cylinders nor degradation of the optical performance was observed over a total of 8 switching cycles employing a gradual re-amorphisation approach.

Finally, and based on the experimentally-achieved multilevel control, the functionality and re-scaling capabilities of the proposed architecture have been investigated towards future research trends based on high efficiency optical phase control in the MWIR. This was numerically studied via a hybrid combination of the novel low loss phase change material $Ge_2Sb_2Se_4Te_1$ with Si nanocylinders, where local optical phase control can be achieved in a fixed-array geometry via changing the fraction of crystallisation of GSST embedded layers. Such devices can be optimised to provide different ranges of optical phase coverage, depending on the application needs, simply by changing the total volume of GSST material embedded inside the nanocylinder. Excellent efficiencies of operation of at least 75% in transmission were obtained, clearly outperforming phase-change plasmonic-based devices. However, significantly larger GSST thicknesses (up to 350 nm) were found to be needed for an entire 2π optical phase coverage, which could hinder the re-amorphisation capabilities of the proposed structure. Nevertheless, it was found that splitting the total volume in various thin layers across the cylinder body would result in the same optical response due to the homogeneous electric field distribution inside the cylinder, thus

could potentially ease heat dissipation after melting of the PCM layer (and improve the necessary cooling rates). Future work related to this part of the project would be therefore to investigate the reversible switching capabilities of the proposed devices as a function of the PCM volume embedded inside the silicon body, which would give an insight about the maximum amount of active material that can be used in such configurations.

Chapter 6

Hybrid dielectric-plasmonic metasurface architectures : Towards high efficiency phase-change metasurfaces with in-situ switching

6.1 Introduction and motivation

As discussed in **Chapters 2** and **5**, all-dielectric antennas are showing great potential towards the realisation of optical metasurfaces with high efficiency due to the absence of plasmonic losses [88]. Like the majority of currently available meta-atom architectures, this approach was inspired and re-scaled from the RF and MW antennae technology, where building blocks made of high refractive indices having different shapes have been used for filtering and moulding EM radiation for several decades now [209]. The purpose of dielectric resonant antennas (DRA) at RF and MW frequencies was however initially different from optical frequencies, as metal-based resonant elements can be considered perfect electric conductors, and thus do not suffer from plasmonic losses [8]. Instead, DRA have been used in such EM regimes as a way to miniaturise elements, since the dimensions required to excite dipole and higher order resonances scale linearly with the wavelength inside the material (i.e. $D \propto \lambda = \lambda_0/n$) [209, 210] rather than with the free-space wavelength

as in their metallic counter parts (where D $\propto \lambda_0$) [97]. As depicted in **Figures 6.1a** and **b**, further miniaturisation can be implemented through the introduction of a perfect symmetry plane (mirror metal plane) at the center of the dielectric block, which reduces the required resonator height by a factor of 1/2 based on the method of images. The same approach can be applied to scale down the antenna geometrical cross section to 1/4 of its original size, via including a second metal plane at one of the lateral boundaries of the antenna (**Figure 6.1c**) [97].

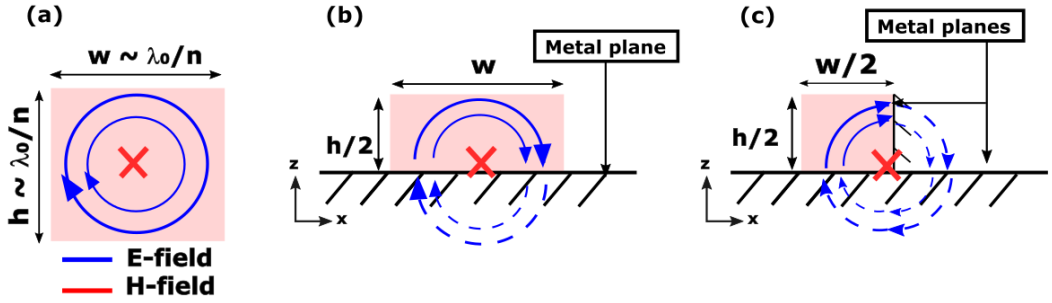

FIGURE 6.1: **(a)** Representation of magnetic dipole induction in a typical DRA operating at MW and RF frequencies, where high index materials can be used to miniaturise its geometry due to scaling being inversely proportional to the refractive index. **(b)** Introducing a perfect electric conductor in the center of the structure (e.g. a metal at low frequencies) results in a reduction of the required antenna height *h*. **(c)** A cross section area reduction down to 1/4 of the original size can be achieved by implementing a second metal plane in one of the DRA lateral boundaries.

In the optical regime, however, the scaling rules become different as the operation frequencies get closer to the plasma frequency of metals. Because metals do not behave as perfect electric conductors in such regimes (i.e. light is not perfectly reflected by the metal surface), radiation penetration inside the the metallic parts can no longer be neglected [75]. As a result, scaling of metallic antennas is not linear with the free-space wavelength λ_0 nor with the wavelength of the surrounding dielectrics λ, but rather with the so-called effective wavelength λ_{eff}, which depends on both the optical properties of the metal/dielectric interface, as well as the antenna geometry [75, 97, 101]. Such effective wavelength is typically of the order of 2 to 5 times smaller than the free-space wavelength [97]. Because of that, plasmonic antennae have no real competitor in terms of miniaturisation, something which is highly desirable for certain applications requiring high electromagnetic field confinement, such as photodetection or non-linear signal conversion. At the same time, as discussed in **Chapter 2**, plasmonic antennas can suffer from strong optical losses due to

electric fields being exponentially attenuated inside the metallic parts [75]. Recently, the use of hybrid dielectric/plasmonic antennae structures inspired from DRA in the RF and MW regimes was proposed to enhance the efficiency of phase-gradient metasurfaces at visible frequencies, where plasmonic MIM configurations start to suffer from severe ohmic losses coming from the top and bottom metallic parts [101, 111]. Particularly, as shown in **Figure 6.2a**, high index, low loss TiO_2 nanocylinders having different sizes and lying on a continuous silver plane were employed as a phase-gradient metasurface, resulting in experimental steering efficiencies up to 50% at $\lambda_0 = 633$ nm [11]; a very high value for the spectral range considered (**Figure 6.2b**).

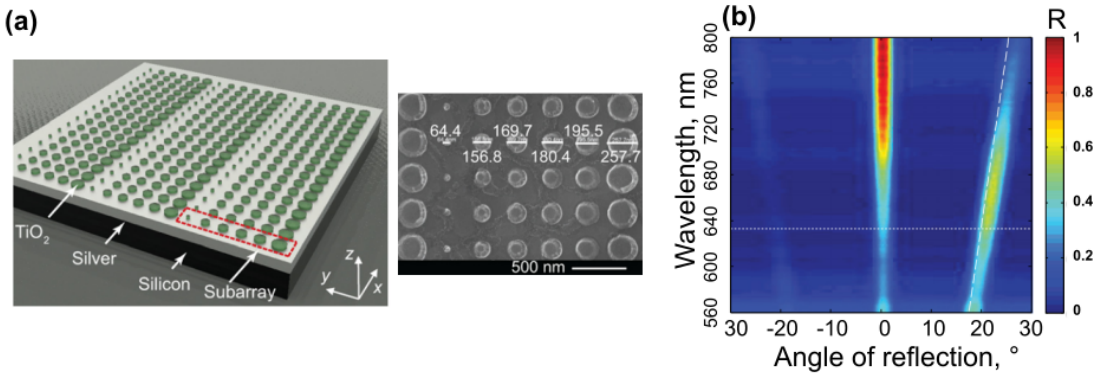

FIGURE 6.2: **(a)** Hybrid dielectric-plasmonic phase-gradient metasurface consisting of TiO_2 high-index, lossless nano-cylinders on top of a silver plane (left) and SEM picture of the fabricated structure (right). **(b)** Experimentally obtained angular reflectance, showing steering efficiencies up to 50% (colorbar). Figures reproduced and re-adapted from [11].

In this chapter, the potential of such an hybrid metasurface approach in combination with small inclusions of phase-change materials was numerically and experimentally evaluated, motivated by two key features:

- Firstly, by the fact that hybrid configurations can enhance the scattering efficiency with respect to MIM configurations, as demonstrated in ref. [11]. This could potentially result in beam steering efficiencies being significantly improved with respect to what was achieved in Chapter 4.

- Secondly, because such an approach provides as well a pathway towards in-situ resistive switching, due to (contrary to the all-dielectric approach shown

in **Chapter 5**) the presence of electrically conductive surrounding materials (metal bottom plane).

A generic scheme of the unit cell studied during this chapter is shown in **Figure 6.3a**. It consists of deeply subwavelength sized GST inclusions embedded within the body of a high-index (Si) dielectric cubic resonator, an analogue to the all-dielectric approach shown in **Chapter 5**. Here, however, the whole structure lies on top of a gold metal plane, which acts as a reflective symmetry plane (i.e. as in RF and MW dielectric antennae described previously), while at the same time provides an electrically-conductive medium to enable in-situ resistive switching of the PCM inclusions. A thin oxide layer (8 nm) is placed between the nanocube and the metal plane, in order to avoid thermally induced diffusion of gold into silicon and/or GST during the phase-change process [74, 211, 212]. As depicted in **Figure 6.3b**, via properly tailoring the cube geometry, magnetic dipole resonances (see colorbar) can be induced at a particular wavelength (here λ_0 = 1550 nm) via displacement current loops (white cones) being imaged by the metal plane. Such modes are qualitatively similar to the HEM modes of dielectric resonators at RF and MW frequencies [213], with the main difference of a clear penetration of electric fields inside the metal layer, due to the finite conductivity of metals at optical frequencies [11].

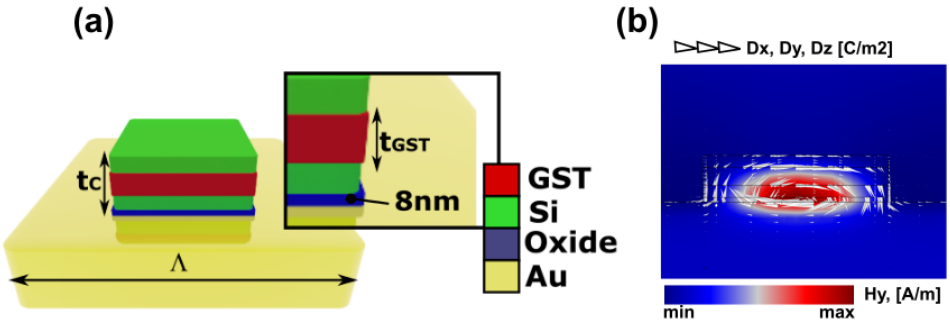

FIGURE 6.3: **(a)** Schematics of the hybrid dielectric/plasmonic unit cell proposed in this chapter, consisting of silicon nanocubes having small GST inclusions on top of a gold metal plane **(b)** Fundamental mode (simulated in COMSOL) supported by an infinte array of nanocubes shown in **(a)**, for an excitation wavelength of λ_0 = 1550 nm.

The main outcome of this chapter is to study and validate the potential, versatility and practicability of the above described structure via the design and fabrication of a set of devices having different functionalities. Particularly:

- **In section 6.2**, we show how reconfigurable hybrid dielectric/plasmonic metasurfaces enabled by PCMs can be, for instance, designed to operate as perfect absorbers/modulators operating in the NIR, where the absorption peaks can be switched from the O to the C optical telecommunication bands. In addition, the key role of the oxide layer to avoid thermally induced diffusion is demonstrated via fabrication of devices with and without barriers placed between the bottom gold plane and the dielectric resonator, and subsequent evaluation of the optical response after thermal annealing.

- The same configuration, but with dimensions being re-optimised is proposed in **section 6.3** towards the development of beam steering and beam shaping devices operating in the near infrared with enhanced efficiency.

- Finally, the in-situ switching capabilities of the proposed architectures are numerically evaluated in **section 6.3**, by using the bottom plane as a resistive heater.

6.2 Phase-change active dual-band absorbers/modulators

6.2.1 Super absorber design and analysis

As discussed in the previous section, hybrid dielectric-plasmonic architectures of the form of dielectric antennas on top of metal planes have been proposed as a reliable way to improve efficiency *cf.* metal/insulator/metal configurations [11, 111], especially at shorter wavelengths where plasmonic losses become severe [75]. In this section, the potential of such structures towards perfect absorption and modulation in the NIR is proposed and experimentally realised. This was achieved via incorporating GST inclusions inside a silicon resonator body to minimise its volume, following the design philosophy from previous chapters which already gave excellent results in terms of switchability of the PCM parts. More importantly, the role of thermal diffusion barriers towards practicable in-situ electrical switching was considered. This is especially important to allow plasmonic metalic parts to be used as resistive heaters, since thermally induced diffusion of noble metals into GST and silicon can severely and irreversibly degrade the device optical performance [74].

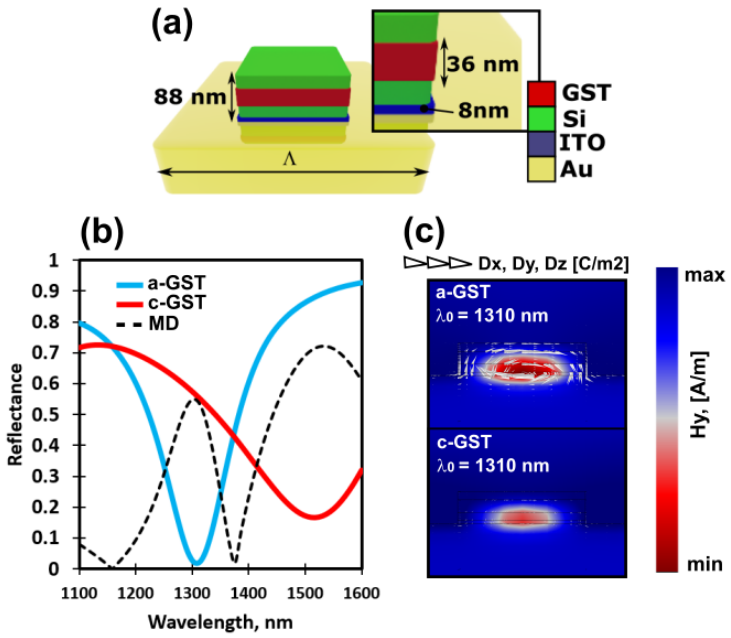

FIGURE 6.4: **(a)** Diagram showing dimensions and of the hybrid dielectric/plasmonic absorber and modulator. **(b)** Numerically obtained reflectance spectra for amorphous (blue) and crystalline (red) GST. Black dashed line represents the absolute modulation depth. **(c)** cross section of the device showing the electromagnetic field distribution when in resonance (a-GST, λ = 1310 nm) and our of resonance (a-GST, λ = 1310 nm), where attenuation of the magnetic dipole induction can appreciated upon crystallisation of the GST layer.

The optimised unit cell geometry is shown in **Figure 6.4a**. As introduced at the beginning of this chapter, it consists of square arrays of silicon dielectric resonators on top of a bottom gold plane. A 36 nm GST layer is embedded within the body of the resonator to provide a tunable environment, and a thin ITO film of 8 nm is placed between the gold plane and the body of the resonator to avoid thermal diffusion of gold into silicon and GST [74, 211]). The dielectric function of gold was obtained from ref. [214], and the properties of GST, Si, and ITO were the same as used in previous devices from Chapters 4 and 5. Figure **6.4b** shows the computed device optical response (reflectance) under normal incidence for amorphous (blue) and crystalline (red) states. In the amorphous phase the device was optimised to operate under the critical coupling regime, thus light is perfectly absorbed at a wavelength of λ = 1310 nm (O-band). **Figure 6.4c (top)** shows the electromagnetic field distribution in a cross section of the device, where a magnetic dipole induction driven by displacement current loops excited inside the resonator can be clearly identified as the origin of such behavior. After crystallisation, the absorption peak is shifted towards the S and C bands. The device modulation depth ($MD = abs(R_{am} - R_{cr})$) is plotted

in black dashed lines, showing values of 57% and 72% in the O and C bands respectively. Note that perfect absorption does not occur in the crystalline phase due to the specific optical properties of amorphous and crystalline GST, which do not allow for the critical coupling condition to be satisfied simultaneously. The use of other PCM compositions having different optical properties (such as e.g. GSST or GeTe) could be explored for this purpose [77, 197].

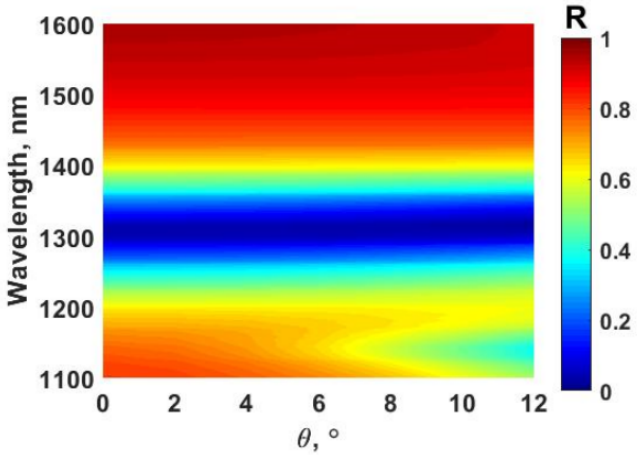

FIGURE 6.5: Effect of the angle of incidence on the reflectance spectra of the devices discussed in this section.

Finally, the device performance under oblique incidence was also analyzed, to gain insight about both its robustness against the angle of incidence and which spectroscopy method would be best employed for its experimental characterisation. Results are displayed in **Figure 6.5** for amorphous GST under TM polarisation, where, contrary to the all-dielectric approach, the resonant peak is stable for a range of angles going from 0 to 12 °. It can be also noticed the presence of a weaker, low frequency mode appearing when exciting the structure at angles above ~ 7 °.

6.2.2 Fabrication of nanocube arrays

Arrays of hybrid phase-change nanocubes were fabricated in 70×70 μm on SiO_2/Si substrates previously cleaned with acetone and isopropyl alcohol (**Figure 6.6a**). A schematic flowchart of the process is depicted in **Figures 6.6b** to **f**, and fine details of the fabrication steps are listed below:

- First, an Au/ITO/Si/GST/Si layer stack was sputtered onto the clean substrate. A thin film of titanium (10 nm) was included between the substrate and

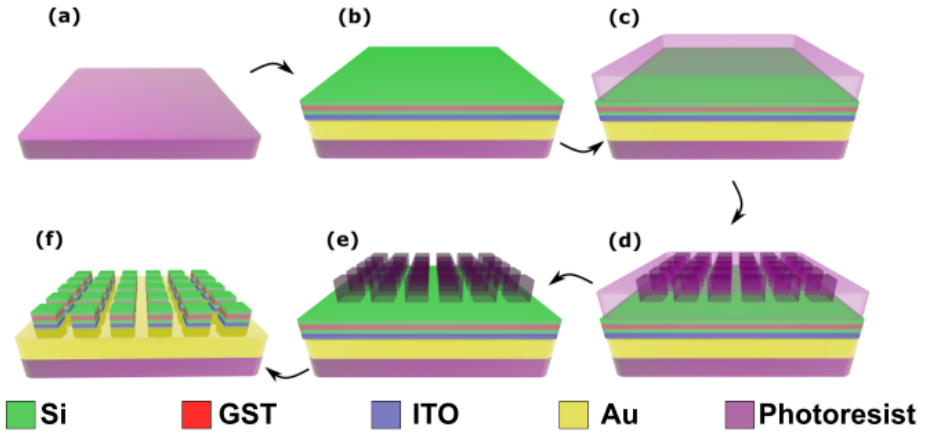

FIGURE 6.6: Flowchart describing the fabrication process of nanocubes. **(a)** Substrate cleaning. **(b)** Deposition of Ti, Au, ITO, Si, GST and Si. **(c)** Spin coating of the adhesion layer and negative photoresist **(d)** E-beam exposure. **(e)** Pattern development. **(f)** Reactive ion etching and photoresist removal.

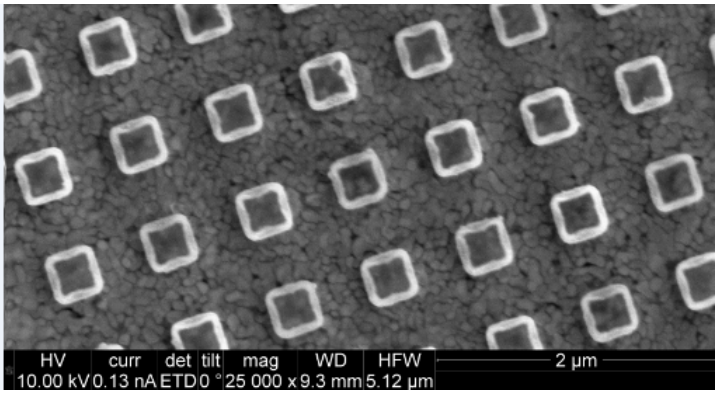

FIGURE 6.7: SEM picture of the as-fabricated hybrid nanocubes.

the gold layer, in order to improve gold adhesion, and thus avoid its delamination. DC sputtering (100 W) in an argon atmosphere (10 sccm) was used for the metallic layers (i.e. Au and Ti) employing a moorfield Nano-PVD sputtering system. The sputtering pressure and base vacuum were 5×10^{-5} mbar and 1.0×10^{-7} mbar respectively. The ITO layer was then deposited using a DC (25 W) custom-built magnetron sputtering machine, again in an Argon atmosphere (10 sccm, base pressure 1.0×10^{-6} mTorr, sputtering pressure 1.0×10^{-3} mTorr). Finally, samples were transferred again to the Nano-PVD system to sputter the remaining layers (i.e. silicon and GST). RF (60 W) sputtering was used for the silicon layers and DC (15 W) sputtering for the GST. The sputtering pressure and base vacuum were the same as for gold and titanium (**Figure 6.6b**).

- Next, the samples were covered with a polymer adhesion layer (Ti-Prime) employing a spin coating machine at 4000 rpm for 20 s, with subsequent post-baking at 90 C for 5 min. A negative resist (ma-N 2403) was then spin-coated at 3000 rpm for 60 s and post-baked at 90 °C for 10 min (**Figure 6.6c**).

- The nano-pattern was then transferred to the resist via e-beam lithography, with subsequent development in MF-319 solution for 45 s to eliminate the un-exposed areas. After lithography, the sample was post-baked at 90 °C for 5 min to increase the hardness of the remaining exposed areas (**Figure 6.6d**).

- The samples were then treated with a RIE process in a $CHF_3/SF_6/O_2$ plasma mixture to remove the regions not covered by the resist. The etching parameters were the same employed for the fabrication of all-dielectric nanocylinders described in **Chapter 5**. Finally, the remaining photoresist (after the RIE process) was removed via soft sonication in warm acetone (**Figure 6.6f**).

An SEM image of one of the fabricated devices is shown in **Figure 6.7**. Measured lattices and cube widths were of the order of 740 nm and 376 nm respectively, very close to the nominal sizes (i.e. 760 nm and 389 nm respectively).

6.2.3 Optical characterisation and validation of ITO as a diffusion barrier

Due to the relatively high robustness of the proposed metasurface configuration against the angle of incidence compared to all-dielectric metasurfaces (as was numerically demonstrated in **section 6.2.1**), Fourier imaging spectroscopy was not considered for the characterisation of these specific devices, and conventional microspectroscopy was used instead. Reflectance spectra of the fabricated structures were measured using a $\times 10$ objective lens with a numerical aperture of NA 0.2 (i.e. collection and excitation angles of $\pm$ 12 °). To check the effectiveness of the 8 nm thick ITO layer as a thermal diffusion barrier between gold and Si/GST (and therefore its optical response robustness against annealing processes), two sets of samples, with and without ITO, were fabricated.

Figures 6.8a to **c** show results from such results(with **Figure 6.8**a displaying again simulation results for amorphous and crystalline states for a direct comparison). **Figure 6.8b** plots the measured reflectance spectra of a device without ITO

barriers. For the as deposited state (amorphous GST), a resonant absorption peak can be clearly identified at $\lambda \sim 1310$ nm, as predicted by numerical simulations. Note the presence of a weaker resonant mode at smaller wavelengths ($\lambda \sim 1170$ nm), which coincides with numerical results shown in section 6.2.1 under oblique incidence, where an additional higher frequency mode can be excited at angles above 7 °. The sample was then annealed at 180 °C for 15 minutes to induce crystallisation of the GST inclusions, and its reflectance spectrum was measured afterwards (red lines). It can be seen that the optical response is completely degraded, and does not correspond to what was predicted by numerical simulations (in **Figure 6.8**a). The experiment was then repeated for samples having an 8 nm thick ITO thermal diffusion barrier incorporated at the Si/Au interface (results are displayed in **Figure 6.8c**). For the amorphous phase (blue lines), again a very good matching *cf.* simulations, with experimentally achieved absorptions of 99.4 % at = 1309 nm, as predicted by the numerical model. Note small signs of a weaker resonant mode located at smaller wavelengths here as well, due to oblique incidence. The expected behavior is also observed after crystallisation of the device, as a red-shift of the resonant peak towards larger wavelengths can be clearly observed (red lines); thus confirming the effectiveness of the diffusion-barrier approach. Finally, as also shown in **Figure 6.8c**, further annealing for 10 min at slightly higher temperatures (230 °C) did not degrade the optical response, but resulted in an overall blue shift of the resonant peak. This was thoguht to be potentially possible due to a decrease of the refractive index of ITO after annealing processes [195], but needs further investigation (i.e. via TEM imaging and ellipsometry measurements of annealed ITO films on gold). In such a case, the refractive index variations of ITO after annealing processes will need to be taken into account at the design stage.

The use of ITO, as well as alternative diffusion barriers not suffering from irreversible, thermally induced, change of the optical properties (i.e. such as SiNx, SiO_2) are currently being further investigated in a new PhD project (carried out by Joe Shields under the same supervision). On the other hand, numerical studies of other non-diffusive metals as a bottom plane (such as TiN [74]) were found to significantly degrade the optical performance due to excessive plasmonic losses, and thus damping of the resonances as shown in **Figure 6.9a**. A thin TiN (8 nm) layer on

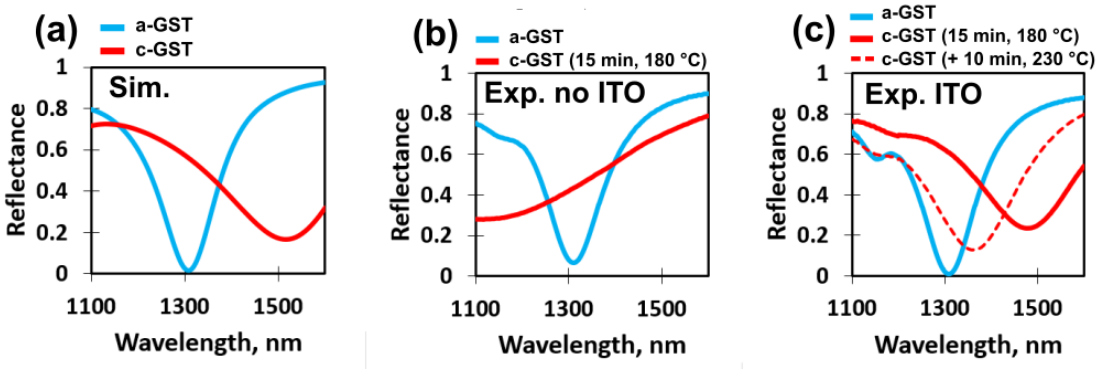

FIGURE 6.8: **(a)** Simulated device performance of the active, phase-change, hybrid dielectric/plasmonic, optimised to operate as a dual band optical absorber. **(b)** Experimentally obtained reflectance spectra for amorphous and crystalline GST in devices without an ITO diffusion barrier, where severe degradation of the optical response is clearly observed after crystallisation. **(c)** Same results displayed in **(b)**, for a device incorporating the ITO layer. The optical response is here mantained after crystallisation, but also modified after further annealing, probably due to changes in the refractive index of ITO.

gold could be however be re-considered as a diffusion barrier without significantly altering the optical response (as confirmed by simulations in **Figure 6.9b**).

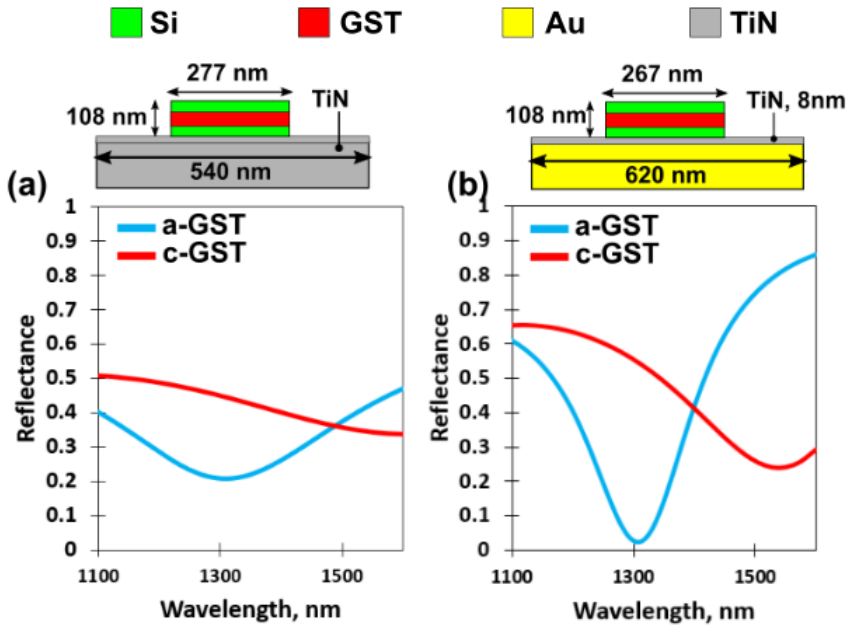

FIGURE 6.9: Optical performance of the device using TiN as a bottom metal plane **(a)**, and only as a barrier layer between the nanocubes and the gold plane **(b)**. Top diagrams show the re-optimised dimensions for each case.

6.3 Phase-change beam steering and beam shaping meta-devices with enhanced efficiency

In addition to perfect absorption, hybrid dielectric/plasmonic metasurfaces can be employed for wavefront shaping purposes with enhanced efficiency, even at visible frequencies (as demonstrated in [11]). This section aims to investigate the potential of such architectures towards active wavefront shaping in the NIR when functionalised with GST. For this purpose, a beam steering device analogue to the one shown in **Chapter 4** was designed (i.e. optimised to operate at λ = 1550 nm), and its optical performance in terms of beam steering efficiency was evaluated for comparison.

6.3.1 Electromagnetic design and analysis

The hybrid dielectric/plasmonic unit cell was re-optimised to operate under the overcoupled (under damped) regime, in order to simultaneously maximise both the amount of optical phase coverage and scattering efficiency. The resulting geometry and material distribution after optimisation is shown in **Figure 6.10a**. To avoid possible issues with changes of the ITO refractive index during annealing processes, as well as dielectric losses coming from this layer (which are not of interest for wavefront shaping devices), ITO was here replaced by SiO_2. Figure **6.10b** shows the optical phase variation as a function of the cube width w, where a near 2π phase coverage of $\Delta\phi$ = 340 $^\circ$ is accessible when the GST layer is amorphous. In analogy to MIM devices reported in **Chapter 4**, the phase profile becomes flat after crystallisation, with only minor phase variations induced by varying w. However, as it can be seen from Figure **6.10c**, the efficiencies (reflectances) employing the new hybrid approach are in this case significantly higher (*cf*. MIM configurations shown in **Figure 4.4c**, Chapter 4), mainly due to the absence of optical losses coming from a top metal plane and ITO layers. For a direct comparison of the potential of hybrid dielectric plasmonic phase-change meta-atoms in terms of efficiency enhancement, a super-cell of the same characteristics of the one studied in Chapter 4 was designed. That is, an array of super-cells made of four elements to impose linear phase gradients of $\Delta\phi$ = 90 $^\circ$ accross the surface when the GST layer is amorphous (i.e. w_1 = 148 nm, w_2 = 326 nm, w_3 = 364 nm and w_4 = 462 nm), resulting in an anomalous reflection angle

of $\theta = 33\,^{\circ}$ according to the generalised Snells law (eq. 2.20). The device behaviour for amorphous and crystalline phases was initially checked via calculation of the instantaneous electric field distribution, where anomalous and specular reflection was confirmed for amorphous and crystalline states, as shown in **Figure 6.11a** and **6.11b** respectively. Finally, the radiation patterns (i.e. reflectance as a function of the reflection angle) of both anomalous and specular reflection operational modes were calculated as described in **Chapter 4**, for a spectral range going from $\lambda = 1500$ nm to $\lambda = 1600$ nm. **Figure 6.11c** and **6.11d** show the resulting patterns for amorphous and crystalline phases respectively, revealing efficiencies as high as 65% for both anomalous (**Figure 6.11c**) and specular (**Figure 6.11d**) reflection; about 1.5 higher than what was achieved with MIM configurations in Chapter 4. The remaining 35% of missing energy is split into diffraction orders m = 0 and m = -1, and attenuated as plasmonic and dielectric losses in the metal plane and GST layers respectively.

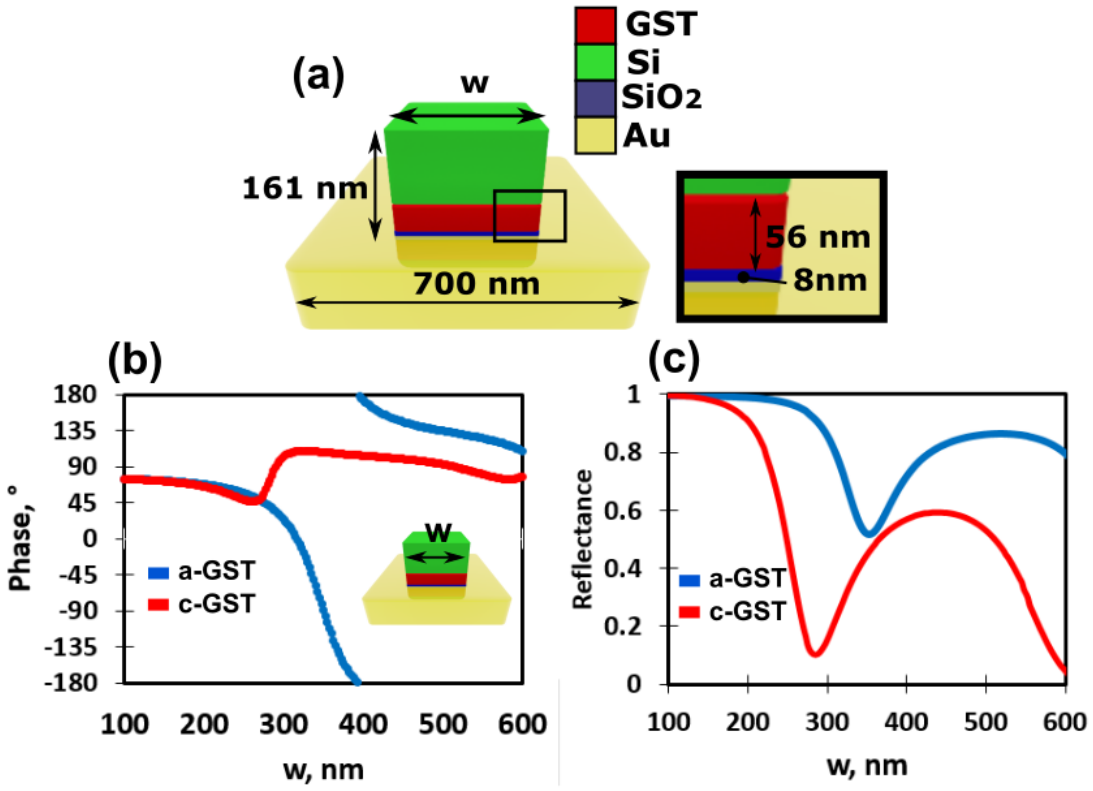

FIGURE 6.10: (a) Geometry and material distribution of the unit cell employed for the realisation of beam steering devices with enhanced efficiency. Phase (b) and amplitude (c) of the device as a function of the cube width w, for an excitation wavelength of $\lambda = 1550$ nm (blue lines correspond to amorphous GST, red lines to crystalline GST).

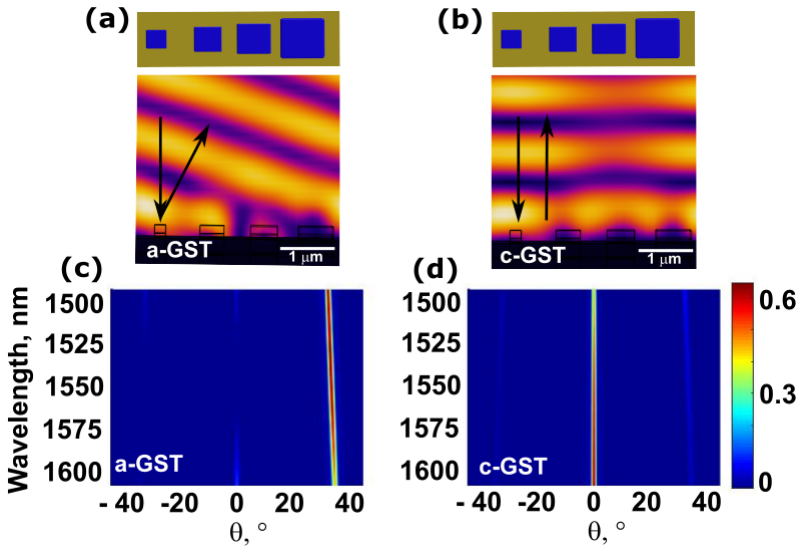

FIGURE 6.11: **(a-b)** Instantaneous electric field distribution over an infinite array of super cells at a wavelength of λ = 1550 nm, for amorphous **(a)** and crystalline **(b)** GST. **(c-d)** Calculated radiation pattern for a finite number of unit cells (15 here), for amorphous **(c)** and crystalline **(d)** GST.

6.3.2 Electrical switching of active beam steering devices with enhanced efficiency

Finally, the in-situ switching (re-amorphisation) capabilities of the proposed architectures were investigated via employing the bottom gold layer as a resistive heater. The total resistance of the heater (R) can be calculated via eq. 6.1 :

$$R = \rho \frac{L_g}{w_g t_g} \tag{6.1}$$

where ρ is the resistivity of thin gold films (11 nΩ.m according to ref. [215]), t_g is the gold layer thickness, and L_g and w_g are the length and width of the gold sheet respectively. As it can be seen from the above equation, rectangular geometries (i.e. where $L_g \neq w_g$) allow for the resistance to be more flexibly engineered, thus such geometry was chosen for the realisation of pixelated devices. An appropriate electronic design can be then implemented via connecting various pixels either in parallel or in series to match the total resistance to the probe resistance.

Figure 6.12a shows the schematics of a single pixel, here having dimensions of 0.09×2.8×11.2 μm. A sheet resistance of 5 Ω was calculated employing eq. 6.1. Details of the geometry and materials employed in simulations are displayed in Figure 6.12b). The temperature dependant thermal conductivity of c-GST, Au, and a-Si

Material	Thermal conductivity [W/mK]	Reference
c-GST	0.5	[137]
Au	318	[216]
a-Si	1.4	[217]
c-Si	280	Manufacturer
SiO_2	1.3	Manufacturer

TABLE 6.1: Thermal conductivity at room temperature of all the materials involved in resistive switching simulations of the developed hybrid dielectric/plasmonic beam steering devices.

were taken from [137], [216], and [217]; and values for SiO_2 and c-Si were adapted from the substrate manufacturer (thermal conductivities of all the employed materials at room temperature are given in table 6.1 for a quick reference). Note that c-Si is a very good thermal conductor with respect to c-GST, therefore, a 60 nm thick SiO_2 layer was placed between the gold layer and the c-Si substrate to act as a bottom thermally resistive barrier, thus force the heat to flow to the device upper part where the GST layer is located.

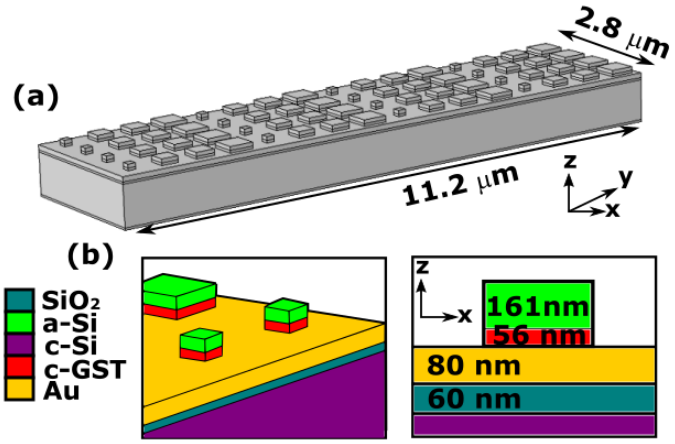

FIGURE 6.12: **(a)** Evolution of the temperature inside the GST inclusions of the 4 cube sizes present in the beam steerer unit cell. **(b)** Temperature distribution of the pixel after the pulse end, confirming values above the melting point (T_m = 630 °C) inside the GST layers.

The pixelated gold heater was set as a volumetric heat source of 0.24×10^{18} W/m^3 for a pulse duration of 20 ns (as explained in the methods **Chapter 3, section 3.1.2**). The cooling rates and temperature distribution of the pixel were then calculated after the pulse end to evaluate the occurence of re-amorphisation. Results from such simulations are displayed in **Figure 6.13**. **Figure 6.13a** shows the temperature evolution inside the GST layers of the four different cube sizes used in the beam steering

device (lighter to darker lines correspond to smaller and larger cubes). After the pulse ceases, a temperature slightly above the melting point (T_m = 630 ° C) is reach by the GST inclusions, confirming melting of the material. The temperature then drops to the GST glass temperature (T_g = 200 °C) after just 15 ns, confirming average cooling rates as high as 30 ° C/ns, more than sufficient to enable re-amorphisation according to e.g. refs. [33, 170].

It can be therefore concluded that the proposed hybrid dielectric-plasmonic architectures show, in addition to high versatility in terms of realisable designs, very good potential towards in-situ thermal switching, which would open up the possibility of their integration in real-wold applications where optically-induced switching (i.e. via laser scans) is not ideal.

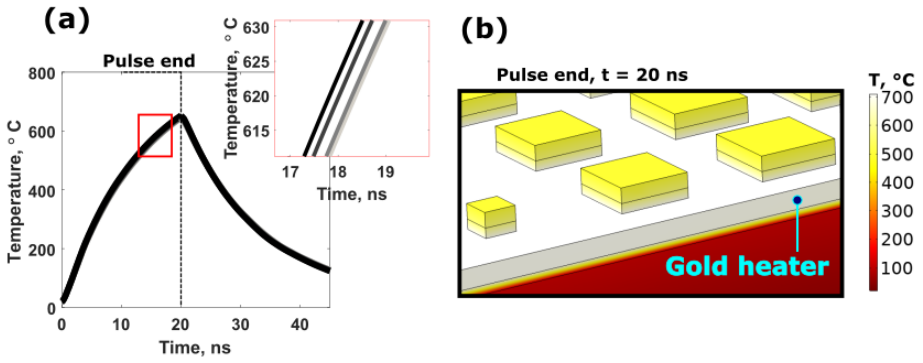

FIGURE 6.13: **(a)** Evolution of the temperature inside the GST inclusions of the 4 cube sizes present in the beam steerer unit cell. **(b)** Temperature distribution of the pixel after the pulse end, confirming values above the melting point (T_m = 630 ° C) inside the GST layers.

6.4 Summary and conclusions

In summary, this chapter shows how hybrid dielectric/plasmonic metasurface configurations can be efficiently combined with phase-change materials to yield active metasurfaces having benefits from all-dielectric metasurfaces in terms of achievable scattering efficiencies, while providing a conductive surrounding medium for in-situ resistive switching of the GST inclusions. Furthermore, the proposed meta-atom architecture showed great versatility in terms of realisable designs, as both super absorbers and high efficiency beam steering devices can be obtained using the same bulding block with slightly different geometries.

The concept has been illustrated and demonstrated via development of two different type of devices for both amplitude and phase control. Particularly:

- A dual band absorber/modulator operating at C and O optical telecommunication bands has been successfully designed, fabricated and tested, revealing very good matching between simulations and experiments, with experimental absorption coefficients as high as 99.4%. More importantly, the use of oxide barriers to prevent thermal diffusion of gold into silicon and/or GST was successfully validated, which is a very important point towards the realisation of devices with in-situ switching capabilities. Devices not incorporating such a layer (i.e. where Si was in direct contact with gold) showed severe degradation of the optical response after crystallisation of the GST layer via hot plate annealing. On the other hand, the optical response of crystalline devices showed no signs of degradation when ITO barrier layers were used. However, further thermal annealing revealed possible changes in the optical properties of ITO, resulting in a blue shift of the resonant absorption peak in the crystalline phase. The exact mechanism of such behavior, as well as the use of alternative barrier layers, such as SiNx and TiN, are currently being investigated.

- The potential of the proposed phase-change meta-atom configuration towards the development of beam steering devices with enhanced efficiency was also evaluated, with calcualted scattering efficiencies up to 65%, 1.5 times higher than what was achieved using MIM configurations (in Chapter 4).

- Finally, thermal simulations suggested that patterning of the device in rectangular pixels would allow to use the gold plane as a resistive heating element, where resistance could be engineered on demand via connection of several pixels either in parallel or in series. A volumetric heat source of $0.24 \text{x} 10^{18}$ W/m^3 resulted in melting of the PCM inclusions over a pulse of 20 ns, with subsequent numerically-obtained quenching rates of 30 °C/ns; thus confirming GST re-amorphisation.

In conclusion, hybrid dielectric/plasmonic architectures combined with GST have shown great potential and practicability towards the realisation and integration of

different type of devices with in-situ electrical switching capabilities.

In terms of future work, the following tasks should be considered:

- Study and evaluation of the suitability of different thermal diffusion barriers, in terms of long term thermal stability, as well as optical response.
- Fabrication of pixelated beam steering devices or absorber devices to realise in-situ electrical switching. This includes characterisation of electrical resistivity of as-sputtered thin gold films.
- Exploration of the device scalability to shorter wavelengths, via judicious material combination. For example, the phase change material Sb_2S_3 has been recently proposed as an alternative material to GST alloys in the visible spectrum [152], as it suffers from relatively low losses in such spectral regime. This new alloy could be potentially inserted in the body of (also lossless) TiO_2 dielectric resonators lying on top of a metal plane, to replicate the excellent device performances found in this work at shorter wavelengths.

Chapter 7

Thesis summary and conclusions

Phase-change metasurfaces are becoming a promising technology towards the development of dynamically reconfigurable compact, low power consumption photonic devices, which would find many suitable applications in the field of optical telecommunications, LIDAR scanning systems, color displays, holography and much more. However, there is a clear lack of agile progress since the first phase-change metasurface concepts were reported, 7 years ago now. As discussed during the course of this thesis, this is mainly due to the several engineering branches involved in the development of phase-change metasurfaces, which sometimes compromise each other in a non-trivial way. This includes, as schematically represented in **Figure 7.1**, thermal, chemical and functional considerations that are typically not taken into account, resulting on impracticable devices suffering from long term degradation and/or unidirectional switching (i.e. without the capability of being successfully re-amorphized). The most clear example is perhaps the compromise between optical and thermal responses, as small PCM volumes are easier to re-amorphize, but at the same time provide less tunability contrast.

This thesis has been mainly focused in totally or partially solving the key engineering problems arising from the marriage of phase-change materials with optical metasurfaces, motivated by the thought that most of such technological challenges can be addressed at the design stage. This was achieved via investigation and experimental realisation of novel device phase-change metasurface architectures, where the followed design philosophy included optical, thermal, functional and chemical considerations shown in **Figure 7.1**. Particularly:

- In terms of **thermal performance**, PCM volumes were always kept to a minimum to avoid thermal insulation, and thus guarantee reversible switching processes. This was achieved via combination of deeply subwavelength sized GST layers with alternative (non-tunable) dielectric materials (such as SiO_2 in **Chapter 4**, or Si in **Chapters 5** and **6**) to allow for the excitation of resonances while minimizing the amount of PCM. Reversible optical switching of phase-change metal/insulator/metal and all-dielectric architectures was experimentally achieved employing such a design approach, and initial simulation results suggest that hybrid dielectric/plasmonic structures would have in-situ electrical switching capabilities.

- On the other hand, as discussed previously, minimizing the PCM volumes can compromise the **optical response**, resulting in lower optical contrast/tunability between amorphous and crystalline states. This was addressed when possible via strategically locating the PCM inclusions in the regions of high electric field concentration (i.e. antinodes of the resonant modes), as demonstrated in **Chapter 5**. In addition, the combination of PCM with low-loss metasurface architectures, such as all-dielectric and hybrid dielectric/plasmonic configurations, resulted in scattering efficiencies as high as 70% and 65% respectively, very suitable values for both optical filtering and wavefront engineering.

- Finally, possible **chemical issues** such as PCM oxidation or metal diffusion were also successfully addressed at the design stage. The former via avoiding direct exposure of GST to air; whereas the later by incorporating thermal barrier layers, and exploration of metal-free metasurfaces (i.e. all-dielectric metasurfaces shown in **Chapter 5**).

In addition, special emphasis has been put in the development of phase-change "meta-devices" for active optical phase control, something that is not yet well-explored; as most of the work carried out up to now relies in active amplitude control [7, 63, 64, 65, 66, 67, 68, 69, 39, 70, 71]. Specific contributions to knowledge arising from this thesis include the following:

- Definition of new metasurface design approaches to minimise the PCM volumes, while maximizing optical efficiency and contrast (Chapters 4 to 6, references [38], [80] and [79]).

- First realisation of active, non-mechanical beam steering, employing phase-change materials in combination with metasurfaces (**Chapter 4**, reference [38]).

- First experimental demonstration of all-dielectric phase-change metasurfaces with multilevel **and** reversible switching capabilities (**Chapter 5**, reference [79]).

- Highest phase-change meta-device efficiencies reported up to now, with values up to 70% for all-dielectric configurations (**Chapter 5**, reference [79]), and up to to 65% for hybrid dielectric/plasmonic architectures **(Chapter 6**, reference [80]).

- First experimental validation of the use of thin oxide layers as thermal diffusion barriers in phase-change metasurfaces involving the use of thermally diffusive metals (**Chapter 6**, currently being further developed in a new PhD project).

- Introduction of the concept of hybrid dielectric-plasmonic metasurfaces having key functional benefits from all-dielectric metasurfaces in terms of optical efficiency, and from plasmonic metasurfaces in terms of compactness and in-situ electrical switching capabilities (**Chapter 6**, reference [80], and currently being further developed in a new PhD project).

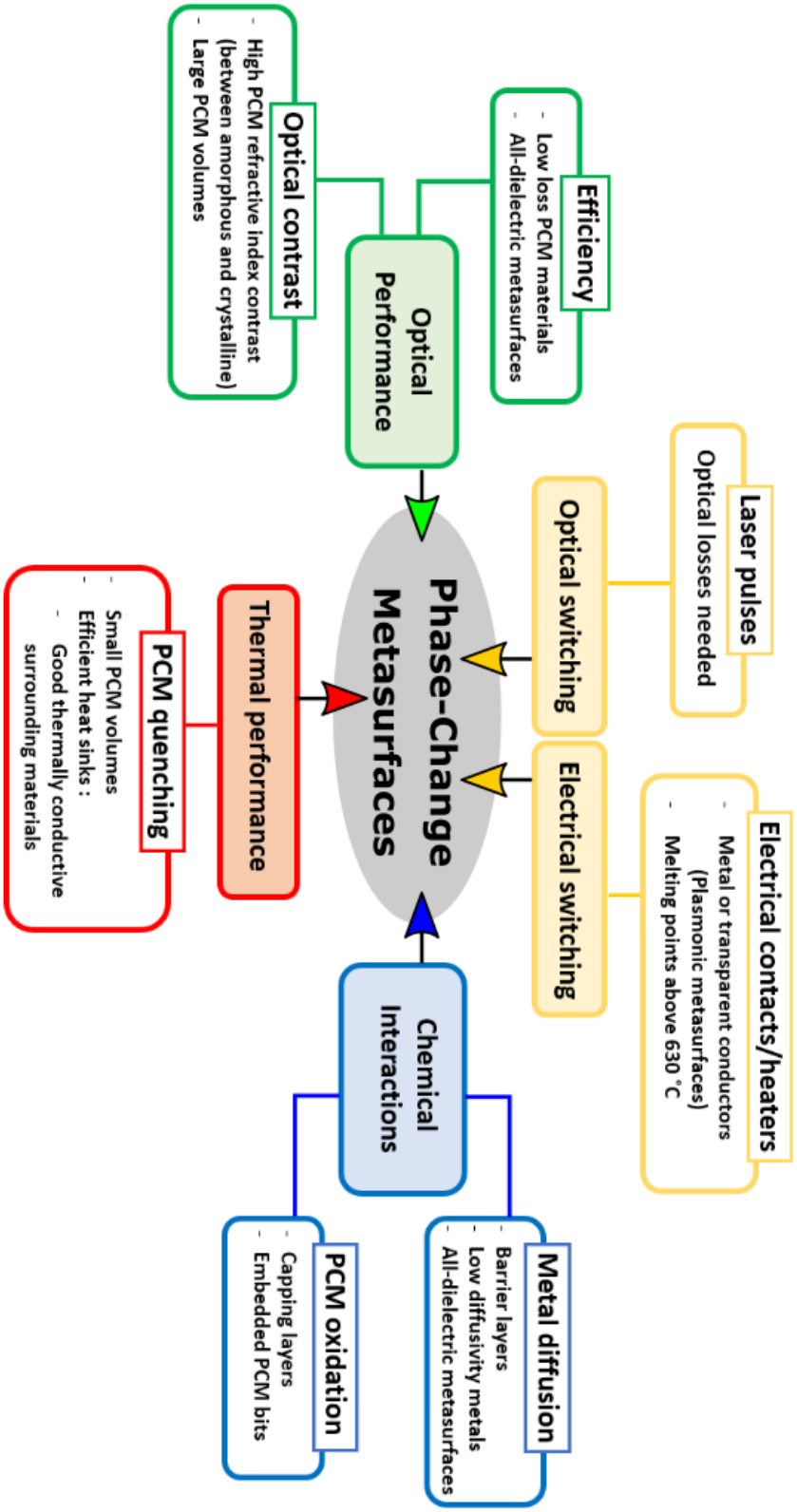

FIGURE 7.1: Diagram showing optical (green), thermal (red), chemical (blue) and functional (yellow), considerations for a successful development of phase-change metasurfaces.

Appendix A

Appendix

A.1 Optical properties for FEM simulations of active plasmonic beam steerers

The refractive index n and absorption coefficient k of the materials employed for the modelling of phase-change plasmonic beam steerers are shown in **Figure A.1**. Values were taken from references [218], [219], and [220] for aluminum, SiO_2 and ITO respectively.

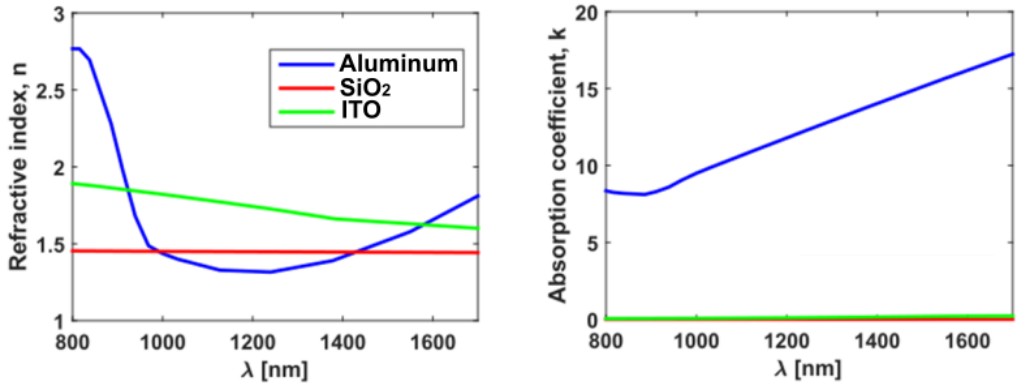

FIGURE A.1: Optical properties of Aluminum, SiO_2 and ITO employed in FEM simulations.

Appendix B

Appendix

B.1 Resonant regimes in asymmetric Fabry-Pérot cavities

In a Fabry-Pérot cavity, the complex output electric fieldE_{out} for an input electric field E_{in} can solved by superposing the beam reflected by the first surface with a series of secondary beams coming from internal reflections inside the cavity (**Figure B.1**). Particularly, an asymmetric Fabry-Perot cavity –also known as Gires-Tournois etalon— consists of a dielectric layer sandwiched between two reflective interfaces. The "asymmetric" connotation comes from the fact that one of the reflective surfaces has a reflection Fresnel coefficient of $r_1 < 1$, whereas the second one is typically close to being a perfect reflector $r_2 \approx 1$. The output electric field E_{out} for this configuration is given by [4, 192, 221]:

$$E_{out} = \frac{E_{in}(r_1 + e^{i\delta})}{1 + r_1 e^{i\delta}} \tag{B.1}$$

with r being the total reflection coefficient, and δ the roundtrip optical phase accumulation inside the cavity, named cavity phase, which at normal incidence is given by:

$$\delta = \frac{4\pi}{\lambda_0} t\tilde{n} = \beta + \alpha i \tag{B.2}$$

where t is the cavity thickness, $\tilde{n}$ is the complex refractive index of the cavity, and β and α are the real and imaginary parts of δ respectively. For a lossless cavity (i.e. made of non-lossy materials, thus $\mathrm{Im}(\delta) = 0$), the amplitude (modulus) and phase (argument) from eq. B.1 become:

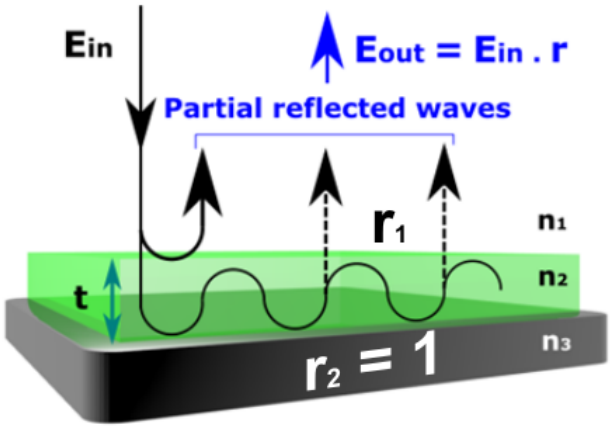

FIGURE B.1: Schematics of a simple asymmetric FP cavity.

$$E_{out} = E_{in} \tag{B.3}$$

$$\angle E_{out} = tan^{-1}\Big[\frac{(1-{r_1}^2)sin\beta}{2r_1+({r_1}^2+1)cos\beta}\Big] \tag{B.4}$$

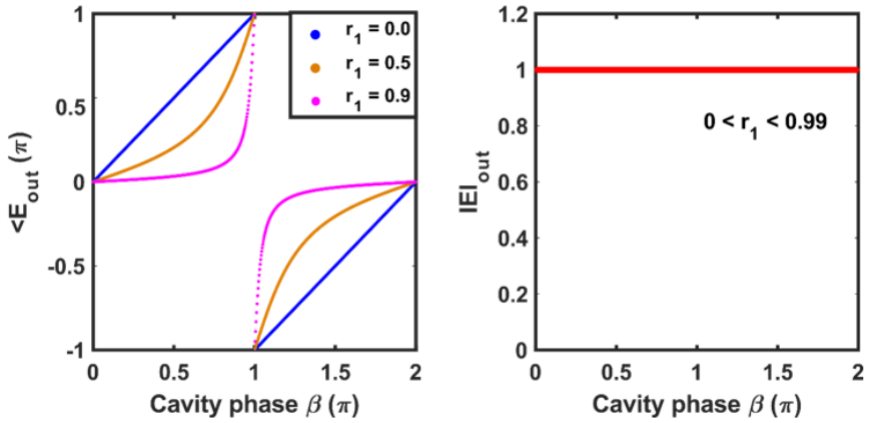

FIGURE B.2: Influence of the Fresnel coefficient r_1 on the output phase and amplitude of a non-lossy asymmetric FP cavity.

The output beam amplitude is therefore constant and equal to the amplitude of the incoming beam for any possible value of r_1 and β. However, the output optical phase strongly depends on both r_1 and β. As it can be seen from **Figure B.2**, for $r_1 = 0$, no reflection from the first surface takes place, which results in a linear trend of $\angle E_{out}$ with β. As r_1 increases, the output change in the optical phase becomes highly non-linear when approaching the cavity resonance (i.e. when $\beta = \pi$)[4]. Such a region of non-linearity allows therefore for controlling the output beam phase by slightly detuning the cavity phase β, which can be achieved via changes in the refractive

index and/or cavity thickness as it can be seen from B.2.

For a cavity with moderate losses where $\mathrm{Im}(\delta) \neq 0$, eqs. B.5 and B.6 become:

$$E_{out} = E_{in}\sqrt{\frac{e^{-2\alpha} + 2r_1 e^{-\alpha} + cos\beta + {r_1}^2}{r_1(1+e^{-2\alpha}) + (r_1^2+1)e^{-\alpha}cos\beta}} \tag{B.5}$$

$$\angle E_{out} = tan^{-1}\Big[\frac{(1-{r_1}^2)e^{-\alpha}sin\beta}{r_1(1+e^{-2\alpha} + ({r_1}^2+1)e^{-\alpha}cos\beta}\Big] \tag{B.6}$$

Contrary to the non-lossy case, both amplitude and phase of the beam become strongly dependant on r_1, and α. In fact, as shown in **Figure B.3**, three resonant regimes with different features can be identified based on this two values:

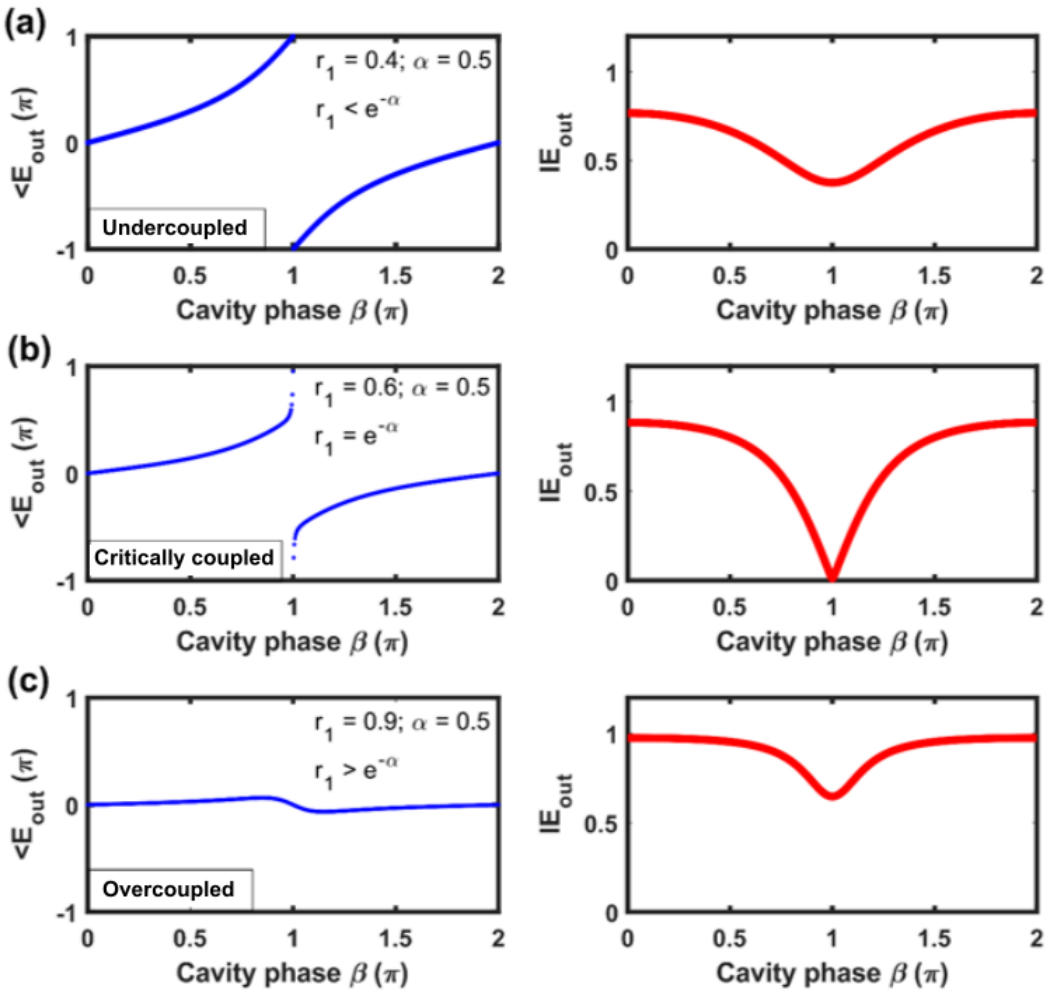

FIGURE B.3: Phase (left) and amplitude (right) of the three FP resonant regimes: **(a)** Overcoupled, **(b)** Critically coupled, **(c)** Undercoupled.

1. When $r_1 < e^{-\alpha}$ (**Figure B.3a**). This case corresponds to the overcoupled (underdamped) regime. Here, a 2π phase accumulation can be achieved via varying the

cavity phase, either by changing the refractive index of the medium or by varying the cavity thickness. This regime is ideal for applications requiring phase manipulation such as wavefront shaping.

2. When $r_1 = e^{-\alpha}$ (**Figure B.3b**). The system is critically coupled and thus provides the fastest approach to zero amplitude. A 2π phase coverage is still possible to achieve, but light is perfectly absorbed when the cavity is in resonance ($\beta = \pi$), thus resulting in phase modulation with low efficiency. Such configuration is therefore ideal for applications requiring for perfect absorption.

3. When $r_1 > e^{-\alpha}$ (**Figure B.3c**). Undercoupled (overdamped) regime. A 2π phase coverage becomes unaccessible. Such situation would be well suited e.g. for amplitude-only modulation where strong amplitude variations are accompanied by very little changes in the phase.

Any of the above described regimes can be therefore engineered by appropriately balancing the fraction of energy not coupled the cavity (determined by r_1) with respect to the energy lost inside the cavity (i.e. $e^{-\alpha}$).

Bibliography

[1] Jay Enoch. “History of mirrors dating back 8000 years”. In: *Optometry and vision science* 83.10 (2006).

[2] Olivier Darrigol. *A history of optics from Greek antiquity to the nineteenth century*. Oxford University Press, 2012.

[3] Warren Jay Smith. *Modern optical engineering*. Tata McGraw-Hill Education, 2008.

[4] Jose Philippe Pérez. *Optique géométrique matricielle et ondulatoire*. Masson, 1993.

[5] Laszlo Solymar and Ekaterina Shamonina. *Waves in metamaterials*. Oxford University Press, 2009.

[6] Nanfang Yu and Federico Capasso. “Flat optics with designer metasurfaces”. In: *Nature Materials* 13.2 (2014).

[7] Santiago Garcıa-Cuevas Carrillo et al. “Reconfigurable phase-change meta-absorbers with on-demand quality factor control”. In: *Optics Express* 26.20 (2018).

[8] Stanislav B Glybovski et al. “Metasurfaces: From microwaves to visible”. In: *Physics Reports* 634 (2016).

[9] Xingjie Ni, Alexander V Kildishev, and Vladimir M Shalaev. “Metasurface holograms for visible light”. In: *Nature Communications* 4.1 (2013).

[10] Benedikt Groever, Wei Ting Chen, and Federico Capasso. “Meta-lens doublet in the visible region”. In: *Nano letters* 17.8 (2017).

[11] Longfang Zou et al. “Spectral and angular characteristics of dielectric resonator metasurface at optical frequencies”. In: *Applied Physics Letters* 105.19 (2014).

[12] Qiong He, Shulin Sun, Lei Zhou, et al. "Tunable/Reconfigurable Metasurfaces: Physics and Applications". In: *Research* 2019 (2019).

[13] Arash Nemati et al. "Tunable and reconfigurable metasurfaces and metadevices". In: *Opto-Electronic Advances* 1.5 (2018).

[14] Sergey V Makarov et al. "Light-Induced Tuning and Reconfiguration of Nanophotonic Structures". In: *Laser & Photonics Reviews* 11.5 (2017).

[15] Sergey Makarov et al. "Tuning of magnetic optical response in a dielectric nanoparticle by ultrafast photoexcitation of dense electron–hole plasma". In: *Nano Letters* 15.9 (2015).

[16] Martina Abb et al. "All-optical control of a single plasmonic nanoantenna–ITO hybrid". In: *Nano Letters* 11.6 (2011).

[17] Martti Kauranen and Anatoly V Zayats. "Nonlinear plasmonics". In: *Nature Photonics* 6.11 (2012).

[18] Charles Rauscher and Robert Laenen. "Analysis of picosecond mid-infrared pulses by two-photon absorption in germanium". In: *Journal of Applied Physics* 81.6 (1997).

[19] Maxim R Shcherbakov et al. "Ultrafast all-optical switching with magnetic resonances in nonlinear dielectric nanostructures". In: *Nano Letters* 15.10 (2015).

[20] Gregory A Wurtz et al. "Designed ultrafast optical nonlinearity in a plasmonic nanorod metamaterial enhanced by nonlocality". In: *Nature Nanotechnology* 6.2 (2011).

[21] Nikolai Berkovitch, Pavel Ginzburg, and Michel Orenstein. "Nano-plasmonic antennas in the near infrared regime". In: *Journal of Physics: Condensed Matter* 24.7 (2012), p. 073202.

[22] Alexey V Krasavin et al. "Nonlocality-driven supercontinuum white light generation in plasmonic nanostructures". In: *Nature Communications* 7.1 (2016).

[23] Hou-Tong Chen et al. "Active terahertz metamaterial devices". In: *Nature* 444.7119 (2006).

[24] Ghazaleh Kafaie Shirmanesh et al. "Dual-gated active metasurface at 1550 nm with wide (> 300) phase tunability". In: *Nano Letters* 18.5 (2018).

[25] Francesco Bonaccorso et al. “Graphene photonics and optoelectronics”. In: *Nature Photonics* 4.9 (2010).

[26] David Shrekenhamer, Wen-Chen Chen, and Willie J Padilla. “Liquid crystal tunable metamaterial absorber”. In: *Physical Review Letters* 110.17 (2013).

[27] Zichen Zhang, Zheng You, and Daping Chu. “Fundamentals of phase-only liquid crystal on silicon (LCOS) devices”. In: *Light: Science & Applications* 3.10 (2014).

[28] Lianlin Li et al. “Electromagnetic reprogrammable coding-metasurface holograms”. In: *Nature Communications* 8.1 (2017).

[29] Jura Rensberg et al. “Active optical metasurfaces based on defect-engineered phase-transition materials”. In: *Nano Letters* 16.2 (2016).

[30] Mohammed Reza M Hashemi et al. “Electronically-controlled beam-steering through vanadium dioxide metasurfaces”. In: *Scientific Reports* 6 (2016), p. 35439.

[31] Minseok Kim et al. “Vanadium-dioxide-assisted digital optical metasurfaces for dynamic wavefront engineering”. In: *Journal of the Optical Society of America B* 33.5 (2016).

[32] Zewei Shao et al. “Recent progress in the phase-transition mechanism and modulation of vanadium dioxide materials”. In: *NPG Asia Materials* 10.7 (2018).

[33] Matthias Wuttig and Noboru Yamada. “Phase-change materials for rewriteable data storage”. In: *Nature Materials* 6.11 (2007).

[34] Matthias Wuttig, Harish Bhaskaran, and Thomas Taubner. “Phase-change materials for non-volatile photonic applications”. In: *Nature Photonics* 11.8 (2017).

[35] Kosmas Galatsis et al. “Alternate state variables for emerging nanoelectronic devices”. In: *IEEE Transactions on Nanotechnology* 8.1 (2008).

[36] Letian Wang et al. “Phase-change silicon as an ultrafast active photonic platform”. In: *arXiv preprint arXiv:1904.11691* (2019).

[37] Yat-Yin Au, Harish Bhaskaran, and C David Wright. “Phase-change devices for simultaneous optical-electrical applications”. In: *Scientific Reports* 7.1 (2017).

[38] Carlota Ruiz de Galarreta et al. “Nonvolatile reconfigurable phase-change metadevices for beam steering in the near infrared”. In: *Advanced Functional Materials* 28.10 (2018).

[39] Jingyi Tian et al. “Active control of anapole states by structuring the phase-change alloy Ge 2 Sb 2 Te 5”. In: *Nature Communications* 10.1 (2019).

[40] Andreas Tittl et al. “Palladium-based plasmonic perfect absorber in the visible wavelength range and its application to hydrogen sensing”. In: *Nano Letters* 11.10 (2011).

[41] Xiaoyang Duan, Simon Kamin, and Na Liu. “Dynamic plasmonic colour display”. In: *Nature Communications* 8.1 (2017).

[42] Yuan Hsing Fu et al. “A Micromachined Reconfigurable Metamaterial via Reconfiguration of Asymmetric Split-Ring Resonators”. In: *Advanced Functional Materials* 21.18 (2011).

[43] Jun-Yu Ou et al. “An electromechanically reconfigurable plasmonic metamaterial operating in the near-infrared”. In: *Nature Nanotechnology* 8.4 (2013).

[44] Imogen M Pryce et al. “Highly strained compliant optical metamaterials with large frequency tunability”. In: *Nano Letters* 10.10 (2010).

[45] Philipp Gutruf et al. “Mechanically tunable dielectric resonator metasurfaces at visible frequencies”. In: *ACS Nano* 10.1 (2016).

[46] Longfang Zou, Martin Cryan, and Maciej Klemm. “Phase change material based tunable reflectarray for free-space optical inter/intra chip interconnects”. In: *Optics Express* 22.20 (2014).

[47] Maoliang Wei et al. “Large-angle mid-infrared absorption switch enabled by polarization-independent GST metasurfaces”. In: *Materials Letters* 236 (2019).

[48] Cheng Hung Chu et al. “Active dielectric metasurface based on phase-change medium”. In: *Laser & Photonics Reviews* 10.6 (2016).

[49] Tianyou Li et al. “Tunable wave plate based on active plasmonic metasurfaces”. In: *Optics Express* 25.4 (2017).

[50] Jingyi Tian et al. “Reconfigurable all-dielectric antenna-based metasurface driven by multipolar resonances”. In: *Optics Express* 26.18 (2018).

[51] Niloufar Raeis-Hosseini and Junsuk Rho. "Metasurfaces based on phase-change material as a reconfigurable platform for multifunctional devices". In: *Materials* 10.9 (2017).

[52] Peter E Sieber and Douglas H Werner. "Reconfigurable broadband infrared circularly polarizing reflectors based on phase changing birefringent metasurfaces". In: *Optics Express* 21.1 (2013).

[53] Emilija Petronijevic and Concita Sibilia. "All-optical tuning of EIT-like dielectric metasurfaces by means of chalcogenide phase change materials". In: *Optics Express* 24.26 (2016).

[54] Chi-Young Hwang et al. "Switchable subwavelength plasmonic structures with phase-change materials for reflection-type active metasurfaces in the visible region". In: *Applied Physics Express* 10.12 (2017).

[55] Rahad Alaee et al. "Phase-change material-based nanoantennas with tunable radiation patterns". In: *Optics letters* 41.17 (2016).

[56] Xiya Ding et al. "Theoretical analysis and simulation of a tunable mid-infrared filter based on Ge2Sb2Te5 (GST) metasurface". In: *Superlattices and Microstructures* 132 (2019).

[57] Sajjad Abdollahramezani et al. "Dynamic dielectric metasurfaces incorporating phase-change material". In: *CLEO: Science and Innovations*. Optical Society of America. 2018, SF1J–1.

[58] Tun Cao, Robert E Simpson, and Martin J Cryan. "Study of tunable negative index metamaterials based on phase-change materials". In: *Journal of Optical Society of America B* 30.2 (2013).

[59] Tun Cao et al. "Fast tuning of double Fano resonance using a phase-change metamaterial under low power intensity". In: *Scientific Reports* 4.1 (2014).

[60] Tun Cao, Chenwei Wei, and Libang Mao. "Numerical study of achiral phase-change metamaterials for ultrafast tuning of giant circular conversion dichroism". In: *Scientific Reports* 5 (2015).

[61] Tun Cao et al. “Mid-infrared tunable polarization-independent perfect absorber using a phase-change metamaterial”. In: *Journal of the Optical Society of America B* 30.6 (2013).

[62] Wei Zhu et al. “Controlling optical polarization conversion with Ge 2 Sb 2 Te 5-based phase-change dielectric metamaterials”. In: *Nanoscale* 10.25 (2018).

[63] Wei Bai et al. “Near-infrared tunable metalens based on phase change material Ge 2 Se 2 Te 5”. In: *Scientific Reports* 9.1 (2019).

[64] Ann-Katrin U Michel et al. “Using low-loss phase-change materials for mid-infrared antenna resonance tuning”. In: *Nano letters* 13.8 (2013), pp. 3470–3475.

[65] Xi Wu et al. “Nonvolatile Tunable Integrated Mid-Infrared GST-SiC Metasurfaces”. In: *2018 IEEE Photonics Conference (IPC)*. IEEE.

[66] Xinghui Yin et al. “Beam switching and bifocal zoom lensing using active plasmonic metasurfaces”. In: *Light: Science & Applications* 6.7 (2017).

[67] Yurui Qu et al. “Dynamic Thermal Emission Control Based on Ultrathin Plasmonic Metamaterials Including Phase-Changing Material GST”. In: *Laser & Photonics Reviews* 11.5 (2017).

[68] Tun Cao et al. “Tuneable thermal emission using chalcogenide metasurface”. In: *Advanced Optical Materials* 6.16 (2018).

[69] Andreas Tittl et al. “A switchable mid-infrared plasmonic perfect absorber with multispectral thermal imaging capability”. In: *Advanced Materials* 27.31 (2015).

[70] Behrad Gholipour et al. “An all-optical, non-volatile, bidirectional, phase-change meta-switch”. In: *Advanced Materials* 25.22 (2013).

[71] Weiling Dong et al. “Wideband absorbers in the visible with ultrathin plasmonic-phase change material nanogratings”. In: *The Journal of Physical Chemistry C* 120.23 (2016).

[72] Ann-Katrin U Michel et al. “Reversible optical switching of infrared antenna resonances with ultrathin phase-change layers using femtosecond laser pulses”. In: *Acs Photonics* 1.9 (2014).

[73] Miquel Rudé et al. "Ultrafast and Broadband Tuning of Resonant Optical Nanostructures Using Phase-Change Materials". In: *Advanced Optical Materials* 4.7 (2016).

[74] Li Lu et al. "Inter-diffusion of plasmonic metals and phase change materials". In: *Journal of Materials Science* 54.4 (2019).

[75] William L Barnes, Alain Dereux, and Thomas W Ebbesen. "Surface plasmon subwavelength optics". In: *nature* 424.6950 (2003).

[76] Santiago Garcıa-Cuevas Carrillo et al. "A Nonvolatile Phase-Change Metamaterial Color Display". In: *Advanced Optical Materials* 7.18 (2019).

[77] Kostiantyn Shportko et al. "Resonant bonding in crystalline phase-change materials". In: *Nature Materials* 7.8 (2008).

[78] David Loke et al. "Breaking the speed limits of phase-change memory". In: *Science* 336.6088 (2012).

[79] Carlota Ruiz de Galarreta et al. "All-Dielectric Silicon/Phase-Change Optical Metasurfaces with Independent and Reconfigurable Control of Resonant Modes". In: *arXiv preprint arXiv:1901.04955* (2019).

[80] Carlota Ruiz de Galarreta et al. "Phase-change metasurfaces for dyamic beam steering and beam shaping in the infrared". In: *2018 IEEE International Symposium on Circuits and Systems (ISCAS)*. IEEE. 2018.

[81] Javier Alda and Glenn D Boreman. *Infrared Antennas and Resonant Structures*. SPIE Press, 2017.

[82] Malcolm H Levitt. *Spin dynamics: basics of nuclear magnetic resonance*. John Wiley & Sons, 2001.

[83] Mark A Ordal et al. "Optical properties of the metals al, co, cu, au, fe, pb, ni, pd, pt, ag, ti, and w in the infrared and far infrared". In: *Applied optics* 22.7 (1983).

[84] Viktor G Veselago. "Electrodynamics of substances with simultaneously negative and". In: *Usp. Fiz. Nauk* 92 (1967).

[85] Rakhesh S Kshetrimayum. "A brief intro to metamaterials". In: *IEEE potentials* 23.5 (2004).

[86] Ari Sihvola. "Metamaterials in electromagnetics". In: *Metamaterials* 1.1 (2007).

[87] Patrice Genevet et al. "Recent advances in planar optics: from plasmonic to dielectric metasurfaces". In: *Optica* 4.1 (2017).

[88] Isabelle Staude and Jörg Schilling. "Metamaterial-inspired silicon nanophotonics". In: *Nature Photonics* 11.5 (2017).

[89] David R Smith, John B Pendry, and Mike CK Wiltshire. "Metamaterials and negative refractive index". In: *Science* 305.5685 (2004).

[90] John B Pendry et al. "Low frequency plasmons in thin-wire structures". In: *Journal of Physics: Condensed Matter* 10.22 (1998).

[91] John B Pendry et al. "Magnetism from conductors and enhanced nonlinear phenomena". In: *IEEE transactions on microwave theory and techniques* 47.11 (1999).

[92] David R Smith et al. "Composite medium with simultaneously negative permeability and permittivity". In: *Physical Review Letters* 84.18 (2000).

[93] Richard A Shelby et al. "Microwave transmission through a two-dimensional, isotropic, left-handed metamaterial". In: *Applied Physics Letters* 78.4 (2001).

[94] Jessie Y Chin, Mingzhi Lu, and Tie Jun Cui. "Metamaterial polarizers by electric-field-coupled resonators". In: *Applied Physics Letters* 93.25 (2008).

[95] Inki Kim et al. "Outfitting next generation displays with optical metasurfaces". In: *ACS Photonics* 5.10 (2018).

[96] Alexandra Boltasseva and Vladimir M Shalaev. "Fabrication of optical negative-index metamaterials: Recent advances and outlook". In: *Metamaterials* 2.1 (2008).

[97] Lukas Novotny and Niek Van Hulst. "Antennas for light". In: *Nature photonics* 5.2 (2011).

[98] Graham H Schennum. "Frequency-selective surfaces for multiple-frequency antennas." In: *Microwave Journal* 16 (1973).

[99] Raj Mittra, Chich H Tsao, and Wai L Ko. "Frequency selective surfaces with applications in microwaves and optics". In: *1980 IEEE MTT-S International Microwave symposium Digest*. IEEE. 1980.

[100] John Huang. "Reflectarray antenna". In: *Encyclopedia of RF and Microwave Engineering* (2005).

[101] Longfang Zou et al. "Efficiency and scalability of dielectric resonator antennas at optical frequencies". In: *IEEE Photonics Journal* 6.4 (2014).

[102] Nina Meinzer, William L Barnes, and Ian R Hooper. "Plasmonic meta-atoms and metasurfaces". In: *Nature Photonics* 8.12 (2014).

[103] C Tserkezis et al. "Understanding artificial optical magnetism of periodic metal-dielectric-metal layered structures". In: *Physical Review B* 78.16 (2008).

[104] Arseniy I Kuznetsov et al. "Magnetic light". In: *Scientific Reports* 2 (2012).

[105] Shuming Wang et al. "Broadband achromatic optical metasurface devices". In: *Nature communications* 8.1 (2017).

[106] Isabelle Staude et al. "Tailoring directional scattering through magnetic and electric resonances in subwavelength silicon nanodisks". In: *ACS Nano* 7.9 (2013).

[107] Manuel Decker et al. "High-efficiency dielectric Huygens' surfaces". In: *Advanced Optical Materials* 3.6 (2015).

[108] Ramon Paniagua-Dominguez et al. "A metalens with a near-unity numerical aperture". In: *Nano letters* 18.3 (2018).

[109] Soheil Farazi, Farhad A Namin, and Douglas H Werner. "Tunable multiband metasurfaces based on plasmonic core–shell nanoparticles". In: *Journal of the Optical Society of America B* 35.4 (2018).

[110] Qingbin Fan et al. "Visible light focusing flat lenses based on hybrid dielectric-metal metasurface reflector-arrays". In: *Scientific Reports* 7 (2017).

[111] Longfang Zou et al. "Dielectric resonator nanoantennas at visible frequencies". In: *Optics Express* 21.1 (2013).

[112] Santiago Garcıa-Cuevas Carrillo et al. "Design of practicable phase-change metadevices for near-infrared absorber and modulator applications". In: *Optics Express* 24.12 (2016).

[113] Yao-Wei Huang et al. "Gate-tunable conducting oxide metasurfaces". In: *Nano Letters* 16.9 (2016).

[114] Wenshan Cai et al. “Metamagnetics with rainbow colors”. In: *Optics Express* 15.6 (2007).

[115] Anders Pors and Sergey I Bozhevolnyi. “Plasmonic metasurfaces for efficient phase control in reflection”. In: *Optics Express* 21.22 (2013).

[116] Fei Ding et al. “A review of gap-surface plasmon metasurfaces: fundamentals and applications”. In: *Nanophotonics* 7.6 (2018).

[117] Thomas Søndergaard et al. “Theoretical analysis of gold nano-strip gap plasmon resonators”. In: *New Journal of Physics* 10.10 (2008).

[118] Che Qu et al. “Tailor the functionalities of metasurfaces based on a complete phase diagram”. In: *Physical Review Letters* 115.23 (2015).

[119] Alexander E Minovich and Anatoly V Zayats. “Geometric-phase metasurfaces based on anisotropic reflection: generalized design rules”. In: *ACS Photonics* 5.5 (2018).

[120] Na Liu et al. “Infrared perfect absorber and its application as plasmonic sensor”. In: *Nano Letters* 10.7 (2010).

[121] Shinpei Ogawa and Masafumi Kimata. “Metal-insulator-metal-based plasmonic metamaterial absorbers at visible and infrared wavelengths: A review”. In: *Materials* 11.3 (2018).

[122] Dimitrios C Zografopoulos and Romeo Beccherelli. “Liquid-crystal-tunable metal–insulator–metal plasmonic waveguides and Bragg resonators”. In: *Journal of Optics* 15.5 (2013).

[123] Guoxing Zheng et al. “Metasurface holograms reaching 80% efficiency”. In: *Nature Nanotechnology* 10.4 (2015).

[124] Shulin Sun et al. “High-efficiency broadband anomalous reflection by gradient meta-surfaces”. In: *Nano Letters* 12.12 (2012).

[125] Nanfang Yu et al. “Light propagation with phase discontinuities: generalized laws of reflection and refraction”. In: *Science* 334.6054 (2011).

[126] Zhongyang Li et al. “Visible-frequency metasurfaces for broadband anomalous reflection and high-efficiency spectrum splitting”. In: *Nano Letters* 15.3 (2015).

[127] Nanfang Yu et al. "Flat optics: controlling wavefronts with optical antenna metasurfaces". In: *IEEE Journal of Selected Topics in Quantum Electronics* 19.3 (2013).

[128] Fei Ding, Anders Pors, and Sergey I Bozhevolnyi. "Gradient metasurfaces: a review of fundamentals and applications". In: *Reports on Progress in Physics* 81.2 (2017).

[129] Hui-Hsin Hsiao, Cheng Hung Chu, and Din Ping Tsai. "Fundamentals and applications of metasurfaces". In: *Small Methods* 1.4 (2017).

[130] James C Ginn et al. "Realizing optical magnetism from dielectric metamaterials". In: *Physical review letters* 108.9 (2012).

[131] Dennis Arslan et al. "Angle-selective all-dielectric Huygens' metasurfaces". In: *Journal of Physics D: Applied Physics* 50.43 (2017).

[132] Ye Feng Yu et al. "High-transmission dielectric metasurface with 2π phase control at visible wavelengths". In: *Laser & Photonics Reviews* 9.4 (2015).

[133] Qunshuo Wei et al. "Broadband multiplane holography based on plasmonic metasurface". In: *Advanced Optical Materials* 5.18 (2017).

[134] Mohammadreza Khorasaninejad et al. "Metalenses at visible wavelengths: Diffraction-limited focusing and subwavelength resolution imaging". In: *Science* 352.6290 (2016).

[135] Mohammadreza Khorasaninejad et al. "Achromatic metalens over 60 nm bandwidth in the visible and metalens with reverse chromatic dispersion". In: *Nano Letters* 17.3 (2017).

[136] Woo Yeong Cho et al. "A 0.18-/spl mu/m 3.0-V 64-Mb nonvolatile phase-transition random access memory (PRAM)". In: *IEEE Journal of Solid-State Circuits* 40.1 (2005).

[137] Stephen Hudgens and Brian Johnson. "Overview of phase-change chalcogenide nonvolatile memory technology". In: *MRS Bulletin* 29.11 (2004).

[138] Stanford R Ovshinsky. "Reversible electrical switching phenomena in disordered structures". In: *Physical Review Letters* 21.20 (1968).

[139] Ray J Von Gutfeld. "The extent of crystallization resulting from submicrosecond optical pulses on Te-based memory materials". In: *Applied Physics Letters* 22.5 (1973).

[140] John P Reifenberg et al. "Thickness and stoichiometry dependence of the thermal conductivity of GeSbTe films". In: *Applied Physics Letters* 91.11 (2007).

[141] RG Neale, DL Nelson, and Gordon E Moore. "Nonvolatile and reprogrammable, the read-mostly memory is here". In: *Electronics* 43.20 (1970).

[142] Guy Wicker. "A comprehensive model of submicron chalcogenide switching devices". PhD thesis. Wayne State University Ph. D Thesis, 1996.

[143] Tetsuya Akiyama et al. "Rewritable dual-layer phase-change optical disk utilizing a blue-violet laser". In: *Japanese Journal of Applied Physics* 40.3S (2001).

[144] Simone Raoux et al. "Phase change materials and phase change memory". In: *MRS Bulletin* 39.8 (2014).

[145] Peiman Hosseini. "Phase-Change and Carbon Based Materials for Advanced Memory and Computing Devices". PhD thesis. University of Exeter, 2013.

[146] C D Wright et al. "Arithmetic and biologically-inspired computing using phase-change materials". In: *Advanced Materials* 23.30 (2011).

[147] Tomoko Ohta. "Phase-change optical memory promotes the DVD optical disk". In: *Journal of Optoelectronics and Advanced Materials* 3.3 (2001).

[148] Manuel Le Gallo et al. "Mixed-precision in-memory computing". In: *Nature Electronics* 1.4 (2018).

[149] Duygu Kuzum et al. "Nanoelectronic programmable synapses based on phase change materials for brain-inspired computing". In: *Nano Letters* 12.5 (2011).

[150] Tomas Tuma et al. "Stochastic phase-change neurons". In: *Nature Nanotechnology* 11.8 (2016).

[151] Carlos Rıos et al. "In-memory computing on a photonic platform". In: *Science Advances* 5.2 (2019).

[152] Weiling Dong et al. "Wide Bandgap Phase Change Material Tuned Visible Photonics". In: *Advanced Functional Materials* 29.6 (2019).

[153] Amr M Shaltout, Vladimir M Shalaev, and Mark L Brongersma. "Spatiotemporal light control with active metasurfaces". In: *Science* 364.6441 (2019).

[154] Tong Cui, Benfeng Bai, and Hong-Bo Sun. "Tunable Metasurfaces Based on Active Materials". In: *Advanced Functional Materials* 29.10 (2019).

[155] Jingbo Sun et al. "An extremely broad band metamaterial absorber based on destructive interference". In: *Optics Express* 19.22 (2011).

[156] Tun Cao et al. "Broadband polarization-independent perfect absorber using a phase-change metamaterial at visible frequencies". In: *Scientific Reports* 4 (2014).

[157] Yiguo Chen et al. "Tunable near-infrared plasmonic perfect absorber based on phase-change materials". In: *Photonics Research* 3.3 (2015).

[158] M Zhang et al. "Plasmonic metasurfaces for switchable photonic spin–orbit interactions based on phase change materials". In: *Advanced Science* 5.10 (2018).

[159] Chulsoo Choi et al. "Metasurface with Nanostructured Ge2Sb2Te5 as a Platform for Broadband-Operating Wavefront Switch". In: *Advanced Optical Materials* (2019).

[160] ZL Sámson et al. "Metamaterial electro-optic switch of nanoscale thickness". In: *Applied Physics Letters* 96.14 (2010).

[161] Xiaohua Wang et al. "Tunable broadband, wide-angle, and polarization-dependent perfect infrared absorber based on planar structure containing phase-change material". In: *Applied Optics* 57.30 (2018).

[162] Tun Cao et al. "Rapid phase transition of a phase-change metamaterial perfect absorber". In: *Optical Materials Express* 3.8 (2013).

[163] Kandammathe Valiyaveedu Sreekanth et al. "Phase-Change-Material-Based Low-Loss Visible-Frequency Hyperbolic Metamaterials for Ultrasensitive Label-Free Biosensing". In: *Advanced Optical Materials* (2019).

[164] Fei Ding, Yuanqing Yang, and Sergey I Bozhevolnyi. "Dynamic Metasurfaces Using Phase-Change Chalcogenides". In: *Advanced Optical Materials* (2019).

[165] Tun Cao and Mengjia Cen. "Fundamentals and Applications of Chalcogenide Phase-Change Material Photonics". In: *Advanced Theory and Simulations* (2017).

[166] *COMSOL Multiphysics User's Guide, version 3.4*. 2007.

[167] Ho-Ki Lyeo et al. "Thermal conductivity of phase-change material Ge 2 Sb 2 Te 5". In: *Applied Physics Letters* 89.15 (2006).

[168] Eun-Kyoung Kim et al. "Thermal boundary resistance at Ge 2 Sb 2 Te 5/ZnS: SiO 2 interface". In: *Applied Physics Letters* 76.26 (2000).

[169] Ke Wang et al. "Influence of doping upon the phase change characteristics of Ge 2 Sb 2 Te 5". In: *Microsystem Technologies* 13.2 (2007).

[170] Fan R Liu et al. "An explanation of the crystallization of amorphous Ge2Sb2Te5 films induced by a short Gaussian laser pulse". In: *Applied Physics Letters* 103.5 (2013).

[171] Rainer Behrisch and Wolfgang Eckstein. *Sputtering by particle bombardment: experiments and computer calculations from threshold to MeV energies*. Vol. 110. Springer Science & Business Media, 2007.

[172] Sergei T Mileiko. "Composite Materials Series, 12: Metal and Ceramic Based Components". In: *Compopsite Materials Series* (1997).

[173] Jerome J Cuomo and R Jeffrey Gambino. "Influence of sputtering parameters on the composition of multicomponent films". In: *Journal of Vacuum Science and Technology* 12.1 (1975).

[174] Dragomir Neshev and Igor Aharonovich. "Optical metasurfaces: new generation building blocks for multi-functional optics". In: *Light: Science & Applications* 7.1 (2018).

[175] Mohammad Ali Mohammad et al. "Fundamentals of electron beam exposure and development". In: *Nanofabrication*. Springer, 2012.

[176] Ampere A Tseng et al. "Electron beam lithography in nanoscale fabrication: recent development". In: *IEEE Transactions on Electronics Packaging Manufacturing* 26.2 (2003).

[177] Jian Zhang et al. "Charging effect reduction in electron beam lithography with nA beam current". In: *Microelectronic Engineering* 88.8 (2011).

[178] Jack W Coburn. *Plasma etching and reactive ion etching*. American Institute of Physics New York, 1982.

[179] Rob Legtenberg et al. "Anisotropic reactive ion etching of silicon using SF 6/O 2/CHF 3 gas mixtures". In: *Journal of the Electrochemical Society* 142.6 (1995).

[180] Brian Henderson and G Frank Imbusch. *Optical Spectroscopy of Inorganic Solids*. Vol. 44. Oxford University Press, 2006.

[181] Adarsh B Vasista, Deepak K Sharma, and GV Pavan Kumar. "Fourier plane optical microscopy and spectroscopy". In: *Digital Encyclopedia of Applied Physics* (2018).

[182] Joseph W Goodman. *Introduction to Fourier optics*. Roberts and Company Publishers, 2005.

[183] Alberto G Curto et al. "Multipolar radiation of quantum emitters with nanowire optical antennas". In: *Nature Communications* 4 (2013).

[184] Dongxing Wang et al. "Directional Raman scattering from single molecules in the feed gaps of optical antennas". In: *Nano Letters* 13.5 (2013).

[185] Deepak K Sharma et al. "Directional second-harmonic generation controlled by sub-wavelength facets of an organic mesowire". In: *Applied Optics* 57.21 (2018).

[186] RN Jagtap and AH Ambre. "Atomic force microscopy (AFM): Basics and its important applications for polymer characterization: An overview". In: *Journal of Polymer Materials* 22.1 (2005).

[187] Jian Shen et al. "AFM tip-sample convolution effects for cylinder protrusions". In: *Applied Surface Science* 422 (2017).

[188] Ludwig Reimer. *Scanning electron microscopy: physics of image formation and microanalysis*. Vol. 45. Springer, 2013.

[189] Byung Joon Choi et al. "Cyclic PECVD of Ge2Sb2Te5 films using metallorganic sources". In: *Journal of the Electrochemical Society* 154.4 (2007).

[190] Zemin Xu et al. "Optical constants acquisition and phase change properties of Ge 2 Sb 2 Te 5 thin films based on spectroscopy". In: *RSC Advances* 8.37 (2018).

[191] Ivan P Kaminow and Thomas L Koch. *Optical fiber telecommunications III*. Academic press, 1997.

[192] Shane Colburn, Alan Zhan, and Arka Majumdar. "Tunable metasurfaces via subwavelength phase shifters with uniform amplitude". In: *scientific Reports* 7 (2017).

[193] Stéphane Larouche and David R Smith. "Reconciliation of generalized refraction with diffraction theory". In: *Optics Letters* 37.12 (2012).

[194] Wei Chen and Haroon Ahmed. "Fabrication of 5–7 nm wide etched lines in silicon using 100 keV electron-beam lithography and polymethylmethacrylate resist". In: *Applied Physics Letters* 62.13 (1993).

[195] Mahir Gulen et al. "Role of annealing temperature on microstructural and electro-optical properties of ITO films produced by sputtering". In: *Journal of Materials Science: Materials in Electronics* 24.2 (2013).

[196] Artemios Karvounis et al. "All-dielectric phase-change reconfigurable metasurface". In: *Applied Physics Letters* 109.5 (2016).

[197] Yifei Zhang et al. "Broadband transparent optical phase change materials". In: *CLEO: Applications and Technology*. Optical Society of America. 2017, JTh5C–4.

[198] Martin J Richards. *Acousto-optic beam steering modulator for a projection system*. US Patent App. 10/154,236. Dec. 2018.

[199] Javier Cambiasso et al. "Bridging the gap between dielectric nanophotonics and the visible regime with effectively lossless gallium phosphide antennas". In: *Nano Letters* 17.2 (2017).

[200] Yuan Hsing Fu et al. "Directional visible light scattering by silicon nanoparticles". In: *Nature Communications* 4 (2013).

[201] Dennis Arslan et al. "Silicon Huygens' Metasurfaces at Oblique Incidence". In: *European Quantum Electronics Conference*. Optical Society of America. 2017, EH_6_2.

[202] Toan Trung Nguyen and Sungjoon Lim. "Wide incidence angle-insensitive metamaterial absorber for both TE and TM polarization using eight-circular-sector". In: *Scientific Reports* 7.1 (2017).

[203] Daniel T Pierce and Wo E Spicer. "Electronic structure of amorphous Si from photoemission and optical studies". In: *Physical Review B* 5.8 (1972).

[204] Ozhan Ozatay et al. "Scaling Properties of Critical Phase Change Conditions in Ge2Sb2Te5 Nanopillars". In: *arXiv preprint arXiv:0804.4485* (2008).

[205] Grigory Lazarev et al. "LCOS spatial light modulators: trends and applications". In: *Optical Imaging and Metrology: Advanced Technologies* (2012).

[206] Yuan Chen et al. "Low absorption liquid crystals for mid-wave infrared applications". In: *Optics Express* 19.11 (2011).

[207] Maik Scheller, Christian Jansen, and Martin Koch. "Applications of effective medium theories in the terahertz regime". In: *Recent Optical and Photonic Technologies*. InTech Rijeka, Croatia, 2010.

[208] Calvin D Salzberg and John J Villa. "Infrared refractive indexes of silicon germanium and modified selenium glass". In: *Journal of the Optical society of America* 47.3 (1957).

[209] Aldo Petosa. *Dielectric resonator antenna handbook*. Artech House Publishers, 2007.

[210] Aldo Petosa and Apisak Ittipiboon. "Dielectric resonator antennas: A historical review and the current state of the art". In: *IEEE antennas and Propagation Magazine* 52.5 (2010).

[211] C Boit, F Lau, and R Sittig. "Gold diffusion in silicon by rapid optical annealing". In: *Applied Physics A* 50.2 (1990).

[212] Nicolaas A Stolwijk et al. "Diffusion and solubility of gold in silicon". In: *Physica B+ C* 116.1-3 (1983).

[213] Archita Banerjee and Debatosh Guha. "A new method to obtain HEM 12δ radiating mode in cylindrical DRA". In: *2014 XXXIth URSI General Assembly and Scientific Symposium (URSI GASS)*. IEEE. 2014.

[214] Robert L Olmon et al. “Optical dielectric function of gold”. In: *Physical Review B* 86.23 (2012).

[215] J Roy Sambles, Kevin C Elsom, and D Jordan Jarvis. “The electrical resistivity of gold films”. In: *Philosophical transactions of the Royal Society of London. Series A, mathematical and physical sciences* 304.1486 (1982).

[216] Moran Wang, Nuo Yang, and Zeng-Yuan Guo. “Non-Fourier heat conductions in nanomaterials”. In: *Journal of Applied Physics* 110.6 (2011).

[217] Seungjae Moon et al. “Thermal conductivity of amorphous silicon thin films”. In: *International Journal of Heat and Mass Transfer* 45.12 (2002).

[218] Aleksandar D Rakić. “Algorithm for the determination of intrinsic optical constants of metal films: application to aluminum”. In: *Applied Optics* 34.22 (1995).

[219] Ian H Malitson. “Interspecimen comparison of the refractive index of fused silica”. In: *Journal of the Optical Society of America* 55.10 (1965).

[220] Kim Sok Won et al. “Optical Properties of Sputtered Indium Tin Oxide Thin Films”. In: *Journal of Korean Physical Society* 59 (2011).

[221] Mikhail A Kats and Federico Capasso. “Optical absorbers based on strong interference in ultra-thin films”. In: *Laser & Photonics Reviews* 10.5 (2016).